

# **Fully-resolved simulations of heat transfer in particle-laden flows**

by

**Yayun Wang**

**A dissertation submitted to The Johns Hopkins University  
in conformity with the requirements for the degree of  
Doctor of Philosophy**

**Baltimore, Maryland**

**Jan, 2018**

**© 2018 by Yayun Wang**

**All rights reserved**

# Abstract

Solid particles suspended in a fluid flow are encountered in many industrial applications, environmental processes and natural systems, such as fluidized beds, cloud formation, dust and pollutants dispersion, industrial mixers, oceanic plankton and many others. In the present dissertation we carry out fully resolved numerical simulations of several problems in this general area both with and without particles-fluid heat transfer. An important aspect of the work is that the finite size of the particles is properly accounted for and that the fluid dynamic forces acting on them are based on an accurate solution of the fluid equations rather than parameterized. The general approach used in this study is based on the PHYSALIS method. This method uses local analytic solutions as "bridges" between the particle surfaces and a fixed underlying Cartesian grid.

For the isothermal case, we study the rotational dynamics of a particle free to rotate around a fixed center in a turbulent flow. Fixing the particle center and carrying out parallel simulations of the flow without the particle enables us to fully characterize the flow incident on the particle. We determine the scales of eddies interacting most with the particle and explore the effect of vortex shedding on the rotational dynamics. The Magnus mechanism is not

found to play a significant role.

To account for particles-fluid heat transfer phenomena, we have extended PHYSALIS to deal with the energy equation. This new direct numerical simulation method for non-isothermal systems is described in detail and extensively validated against experimental studies and analytical solutions. The method is implemented numerically on a GPU-centric code, which is compatible with BLUEBOTTLE – a highly efficient GPU-centric computational fluid dynamics framework. An example of particles transported by a Rayleigh-Bénard convective flow is shown to demonstrate the potential applications of our method. A further application to the thermal wake of particles in turbulent flow is also given.

# Thesis Committee

## Primary Readers

Andrea Prosperetti (Primary Advisor)  
Department of Mechanical Engineering  
Johns Hopkins University

Rajat Mittal  
Department of Mechanical Engineering  
Johns Hopkins University

Tamer Zaki  
Department of Mechanical Engineering  
Johns Hopkins University

# Acknowledgments

It has been a very unique and pleasant journey in my life and it would have been impossible without the patience, guidance and encouragement from my advisor, Andrea Prosperetti. It is a very rare opportunity to be advised by a true scientist with a strong passion for science, from whom I learned more than just mathematics and physics, but also an attitude to the life and work.

I have received much help from many Professors in Johns Hopkins University, especially Prof. Rajat Mittal, Charles Meneveau, Tamer Zaki, Joseph Katz, Sean Sun, Tony Dalrymple. I also want to thank my coworkers in our research group: Adam J. Sierakowski, Daniel P. Willen, Shigan Chu, Gedi Zhou and Yuhang Zhang. I want to pay special thanks to Adam J. Sierakowski, from whom I started to learn the art of coding.

I would like to thank all my peers during my stay in the Johns Hopkins University: Hangjian Ling, Zhuoyu Zhou, Quan Jiao, Xinzhi Xue, Xiang Yang, Cao Zhang, Yuanchao Li, Jing Wang, Qi Wang, Kunlun Bai, Perry Johnson, Jiho You, Ismail Hameduddin. Because all of you, it is no longer a lonely experience of studying oversea but a period with a lot of laughter and happiness.

I also want to thank United States National Science Foundation grant CBET 1335965 for support of this work.

I want to express my deepest love and gratitude to my parents: your love and support make it possible for me to see the world and enjoy my life, thank you!

Finally, I want to give a warm kiss to my significant one, Longhua You. It would not be easy without your endless love during all these years. You are a best friend, a teacher, a companion, a brother and much more. I am so blessed to have met you at a young age and grow up together.

# Table of Contents

<b>Table of Contents</b>	<b>vii</b>
<b>List of Tables</b>	<b>xi</b>
<b>List of Figures</b>	<b>xv</b>
<b>1 Introduction</b>	<b>1</b>
1.1 Modeling methods for particle laden flows . . . . .	3
1.2 Direct Numerical Simulation of particle-laden flow in isothermal system . . . . .	4
1.2.1 Immersed Boundary Methods . . . . .	6
1.2.1.1 Continuous forcing methods . . . . .	6
1.2.1.2 Discrete forcing approach . . . . .	9
1.2.2 PHYSALIS method . . . . .	13
1.3 Direct Numerical Simulation methods for non-isothermal systems	15
1.3.1 Immersed boundary method for non-isothermal system	16
1.3.1.1 Neumann boundary conditions . . . . .	17
1.3.2 Volume of Fluid method . . . . .	20

1.4	Applications of multiphase Direct Numerical Simulation methods to non-isothermal systems . . . . .	21
1.5	Objectives and organization of this dissertation . . . . .	28
<b>2</b>	<b>PHYSALIS method</b>	<b>36</b>
2.1	A general solution . . . . .	36
2.2	Implementation . . . . .	39
2.3	PHYSALIS for arbitrary forcing . . . . .	40
<b>3</b>	<b>Rotational dynamics of a particle in a turbulent stream</b>	<b>44</b>
3.1	Introduction . . . . .	45
3.2	Numerical Method . . . . .	47
3.3	Parameter Values . . . . .	50
3.4	Results . . . . .	53
3.5	Forces . . . . .	63
3.6	Summary and Conclusion . . . . .	70
<b>4</b>	<b>A new DNS method –PHYSALIS for non-isothermal system</b>	<b>75</b>
4.1	Mathematical formulation . . . . .	76
4.2	Modification of PHYSALIS method for momentum equation with buoyancy . . . . .	77
4.3	The local solution . . . . .	78
4.4	Implementation . . . . .	82
4.5	Verification . . . . .	85



4.5.1	Stationary particle in a quiescent fluid . . . . .	85
4.5.2	Stationary particles in a moving fluid . . . . .	93
4.5.3	Transient heating of a sphere in a flow . . . . .	98
4.6	Examples with natural convection . . . . .	99
4.7	Summary and Conclusion . . . . .	104
	<b>Appendices</b>	<b>106</b>
4.A	Integral balances . . . . .	106
<b>5</b>	<b>Heat transfer from an array of fully-resolved particles in turbulent flow</b>	<b>114</b>
5.1	Mathematical model and numerical method . . . . .	116
5.2	Description of the simulations . . . . .	117
5.3	Simplified point-particle model . . . . .	121
5.4	Results . . . . .	124
5.4.1	Heat transfer rate . . . . .	124
5.4.2	Mean field . . . . .	127
5.4.3	Fluctuating field . . . . .	134
5.5	Summary . . . . .	143
	<b>Appendices</b>	<b>144</b>
5.A	Laminar flow and heat transfer past an infinite planar array of point particles . . . . .	144
5.A.1	Mathematical model . . . . .	145

5.A.2	Decomposition of the flow field . . . . .	146
5.A.3	Solution . . . . .	148
<b>6</b>	<b>Conclusion</b>	<b>155</b>
	<b>Curriculum Vitae</b>	<b>158</b>

# List of Tables

3.1	Simulation parameters at the inlet plane and at the plane with the particle center plane for $Re_p = 80$ (upper two lines) and 150; $Re_\lambda$ is the Taylor microscale Reynolds number defined by $Re_\lambda = \lambda_g u' / \nu$ ; $a$ is particle radius; $\eta$ the Kolmogorov length scale, $\lambda_g$ the Taylor length scale, $L$ the integral length scale, $u'$ the RMS of velocity fluctuations and $\Delta x$ the mesh length. . . .	50
3.2	Numerical values of several quantities characterizing the simulations; $\tau_c = 2a/U$ is the convection time past the particle, $\tau_e$ the eddy turn-over time, $St_K$ and $St_e$ the Stokes numbers for the sphere based on the Kolmogorov and turn-over times and $O_{fl}$ , defined in (3.5), the mean angular velocity of a fluid eddy with the size of the particle. . . . .	52
3.3	Root mean square values of the normalized angular velocity and couple components. . . . .	57

- 4.1 The deviation from 1 of the quantity  $\Lambda_T$ , defined in (4.24), is a measure of the error affecting the solution of the energy equation. The results in this table illustrate the sensitivity of the numerical error to the choice of the radius  $r_T/a$  of the integration surface and to different orders of truncation  $\ell_{max}$  of the series expansion (4.9). The situation simulated is a single particle at constant temperature in an enclosure subject to a constant heat flux with no fluid flow. . . . . 86
- 4.2 The deviation from 1 of the quantity  $\Lambda_T$ , defined in (4.24).  $N_p$  is the number of particles;  $a/\Delta x$  is the grid resolution, where  $a$  is the particle radius;  $\alpha$  is the volume fraction;  $D_c$  is the distance between two particle centers;  $D_{left}$  is the distance from the most left particle center to the left boundary;  $D_{top}$  is the distance between the most upper particle center the the top boundary. 87
- 4.3 Calculated drag coefficient  $C_D$  and particle Nusselt number  $Nu_p$  for steady uniform flow past a single spherical particle at  $Re = 50$  for various values of the radius  $r_s$  of the momentum integration surface, order of truncation  $\ell_{max}$  of the infinite summations, mesh lengths per radius  $a/\Delta x$  and domain size. The deviation from 1 of the quantity  $\Lambda_q$ , defined in (4.30), is a measure of the numerical error affecting the solution of the energy equation. For all these simulations, the radius of the integration surface for the temperature is  $r_T/a = 1.15$  and the order of truncation in (4.9)  $\ell_{max} = 3$ . . . . . 94

4.4	Drag coefficient $C_D$ and particle Nusselt number $Nu_p$ for steady uniform flow past a single spherical particle at $Re = 50$ from the literature. The data in the first group are from numerical simulations (label "S"), those in the second one from empirical correlations (label "C"); the last line is an experimental value (label "E"). . . . .	95
4.5	Overall energy balance for single-phase natural convection for two values of the Rayleigh number $Ra$ and Prandtl number $Pr$ and different domain discretizations. The convection cell is a parallelepiped with a square cross section and aspect ratio (side/height) = 1/2; $N_x, N_y$ and $N_z$ are the number of grid points in the two horizontal and the vertical directions; the Nusselt number shown is $Nu = \frac{1}{2}(Nu_c + Nu_h)$ . The quantities in the last three columns should all be equal to 1 in the absence of errors; $\Lambda_u$ is the ratio of the computed kinetic energy dissipation rate to the theoretical result given in (4.56); $\Lambda_\theta$ is the ratio of the temperature dissipation rate to the theoretical result given in (4.52). Ref. represents the work by Stevens, Verzicco, and Lohse (2010). Note that in the work of Stevens, Verzicco, and Lohse (2010), the convection cell is a cylinder rather than a parallelepiped and the numbers of cells quoted are in the azimuthal, radial and axial directions. . . . .	99

4.6	<p>Natural convection with <math>N_p</math> fixed particles and <math>Ra = 2 \times 10^5</math>, <math>Pr = 1.75</math>. The convection cell is a parallelepiped with a square cross section and aspect ratio (side/height) = 1/2; <math>N_x, N_y</math> and <math>N_z</math> are the number of grid points in the two horizontal and the vertical directions. The quantities in the last three columns should all be equal to 1 in the absence of errors; <math>\Lambda_{Nu}</math> is the normalized heat-flux balance given in (4.34); <math>\Lambda_u</math> is the ratio of the computed kinetic energy dissipation rate to the theoretical result given in (4.56); <math>\Lambda_\theta</math> is the ratio of the temperature dissipation rate to the theoretical result given in (4.52). In the multi-particle cases, the particle position is randomly assigned and the particle temperature randomly fixed in the range shown. The volume fraction for <math>N_p = 1</math> is 0.71%, for <math>N_p = 5</math> is 1.0% and for <math>N_p = 8</math> is 1.7%. . . . .</p>	104
5.1	<p>Characteristics of the incident turbulence at the particles plane; <math>Re_\lambda</math> is the Taylor Reynolds number, <math>\eta</math> is the Kolmogorov length, <math>a</math> the particle radius, <math>\tau_E</math> the eddy turn-over time, <math>\ell</math> the integral length scale and <math>u'</math> the root-mean square turbulent velocity fluctuations. . . . .</p>	119
5.2	<p>Nusselt number predicted by several correlations for steady laminar flow past an isolated sphere, and by Gunn's correlation for a sphere in a particle bed, compared with the result of the present simulations; <math>\alpha</math> is the fluid volume fraction. . . . .</p>	123

# List of Figures

1.1	Delta functions - different delta functions with 2, 3, 4 and 6 cell support. Figure from Haeri and Shrimpton (2012). . . . .	7
1.2	Illustration of IB (a) A two-dimensional staggered Cartesian grid with an IB. Locations of $u_x$ and $u_y$ are represented by horizontal and vertical arrows, respectively. Pressure and temperature are positioned at the center of each cell (green square). Lagrangian points on IB are shown with filled circles (red). $\Delta V_k$ is a volume that is assigned to each Lagrangian point. (b) Representation of a sphere by Lagrangian points. Figure from Tavassoli et al. (2013). . . . .	10
1.3	Ghost cell method: ghost, fluid and solid cells presented. Boundary intersect (BI) point and imaginary point (IP) are also presented for a sample ghost cell. Figure from Mittal et al. (2008).	12
1.4	Neumann or Robin boundary condition with two probe points. Two probe points are point 1 and 2 (Luo et al., 2016). . . . .	19

1.5	Vorticity contours superimposed on the temperature contours for different regimes (depend on Grashof numbers). Simulation results by Haeri and Shrimpton (2013). . . . .	26
1.6	Temperature distributions at $t = 5s$ for the five different fluidization velocities: $V = 0.035, 0.04, 0.045, 0.05,$ and $0.055$ m/s (from left to right). Simulation results by Feng and Musong (2014). . . . .	28
3.1	PDF of the angular velocity in the cross-stream plane $(x, y)$ normalized as in (3.7) for $Re_p = 80$ (above) and 150. The highest-peaked (red) and second-highest peaked (black) curves are for the shell and the sphere, respectively. The dashed lines are Gaussian fits. The broadest curve (blue) is for the fluid vorticity averaged over a spherical volume of radius $a$ ; the other curve (yellow) is for the fluid vorticity averaged over a spherical volume of radius $2a$ , both centered at the position of the particle center in the absence of the particle. . . . .	54
3.2	PDF of the dimensionless couple in the cross-stream plane $(x, y)$ (solid black line, squares) and in the direction of the incident flow (red line, circles) normalized as in (3.8) for $Re_p = 80$ (above) and 150. The solid lines and solid symbols are for the sphere and the dashed lines and open symbols for the spherical shell. . . . .	56
3.3	Time history of $L_x^*$ for the sphere with $Re_p = 150$ . Time is normalized by the convection time $\tau_c = 2a/U$ . The persistence time of the sign is denoted by $\Delta$ . . . . .	58



3.4	The solid lines show the PDF's of the sign persistence of the cross-stream plane components of the couple acting on the sphere for $Re_p = 80$ (upper panel) and $Re_p = 150$ . The dashed lines are the sign persistence of the cross-stream vorticity in the absence of the particle averaged over spherical volumes with radius $\frac{1}{2}a$ (solid square), $a$ (solid circle), $2a$ (open square) and $3a$ (open circle). . . . .	60
3.5	The solid lines show the auto-correlation of the cross-stream components of the couple acting on the sphere for $Re_p = 80$ (upper panel) and $Re_p = 150$ . The dashed lines are the auto-correlations of the vorticity averaged over spherical volumes with radius $\frac{1}{2}a$ (solid square), $a$ (solid circle), $2a$ (open square) and $3a$ (open circle). . . . .	61
3.6	Auto-correlation of the horizontal components of the particle angular velocity. The solid lines are for the sphere and the dashed lines for the spherical shell. The squares are for $Re_p = 80$ and the circles for $Re_p = 150$ . . . . .	62
3.7	Scatter plot of $L_y^*$ vs. $F_x^*$ (left) and $L_x^*$ vs. $F_y^*$ for the sphere with $Re_p = 150$ . In spite of the large scatter, a trend compatible with vortex shedding from the particle is clearly visible. . . . .	64
3.8	PDF of the product $F_x L_y$ normalized by the respective RMS values for the sphere with $Re_p = 150$ . The prevalence of negative values is compatible with the effect of vortex shedding in generating the cross-stream force component $F_x$ . . . . .	65

3.9	Six successive images separated by $0.188 \tau_c$ showing an example of the induced shedding of positive vorticity $\Omega_y^*$ from the sphere for $Re_p = 150$ . The color scale ranges over $-2.5 \leq \Omega_y^* \leq 2.5$ . As a consequence of this process a force $F_x > 0$ (directed to the right) and a couple $L_y < 0$ (counterclockwise) act on the particle. . . . .	66
3.10	PDF of the normalized product $F_x \Omega_y$ for the sphere with $Re_p = 150$ . A frequent occurrence of a cross-stream force component due to a Magnus-like mechanism would cause a prevalence of positive values of $F_x \Omega_y$ rather than the negative values indicated by the figure. . . . .	68
3.11	$F_x^*$ (upper panel) and $\Omega_y^*$ vs. time for one realization of the flow past a sphere with $Re_p = 150$ . The closed circles (green) mark instants where the product $F_x \Omega_y$ (normalized as in figure 3.10) is less than -1 while at the instants marked by open squares (red) the normalized product $F_x \Omega_y$ is greater than 1. . . . .	69
4.1	Temperature distribution in the neighborhood of a particle instantaneously brought to the temperature $T_p$ higher than that of the surrounding medium which is at the reference temperature. The lines (in ascending order with increasing time) are the analytic solution (4.25) and the symbols the computed results.	88
4.2	Early-time behavior of the particle Nusselt number for the situation of the previous figure. The line is the exact solution (4.26) and the symbols the numerical results. . . . .	89

4.3	Temperature distribution in the neighborhood of a particle the temperature of which increases linearly with time. Initially both the particle and the medium surrounding it are at the reference temperature. The lines (in ascending order with increasing time) are the analytic solution (4.27) and the symbols the computed results. . . . .	90
4.4	Steady-state temperature distribution in the medium surrounding a particle the temperature of which oscillates in time with a frequency $\omega$ at different instants of time. The Péclet number is $\omega a^2/D = 5$ . The lines are the exact solution (4.28) and the symbols the computational results. . . . .	91
4.5	Steady-state temperature distribution in the medium surrounding a particle the temperature of which oscillates in time with a frequency $\omega$ at different instants of time. The Péclet number is $\omega a^2/D = 20$ . The lines are the exact solution (4.28), the open symbols the computational results found using (4.9) for the temperature at the temperature cage nodes, and the filled symbols the computational results found by adding the correction (4.15) to the temperature at the cage nodes. . . . .	91
4.6	Cumulative error, defined in (4.29) of the corrected (solid line) and uncorrected numerical result for a particle the surface temperature of which oscillates sinusoidally. The horizontal axis is the Péclet number $Pe = \omega a^2/D$ . . . . .	93

4.7	The local Nusselt number, or dimensionless heat flux, defined in (4.31), at the surface of a sphere immersed in a steady uniform flow at a Reynolds number 50 as a function of the azimuthal angle. The solid line is the result of Bagchi, Ha, and Balachandar (2001) and the points the present results. . . . .	96
4.8	Two views of the steady temperature distribution and thermal wakes produced by 10 randomly arranged particles immersed in a cold stream; the color indicates the temperature. The particle temperature is fixed and is randomly assigned between 80% and 120% of the mean value 1 and the temperature of the incoming fluid is 0. . . . .	97
4.9	Time-dependence of the temperature of a particle immersed in a warmer uniform flow with $Re = 50$ . The solid lines are the present results and the dashed lines the results of Balachandar and Ha (2001). The three sets of curves correspond, in ascending order, to different values of the ratio $\rho c_p / (\rho_p c_{pp}) = 0.004$ , 0.02 and 0.1. . . . .	98

4.10 Successive configurations of an eight-particle system in naturally convecting flow with  $Ra = 2 \times 10^5$  and  $Pr = 1.75$ ; the color indicates the temperature normalized by  $T_h - T_c$ , which ranges from -0.5 at the bottom to 0.5 at the top of the cell. The frames are separated by a dimensionless time interval  $\sqrt{g\beta(T_h - T_c)L_z} \Delta t / L_z \simeq 2.07$ . The particle temperature adjusts according to (4.4);  $\rho c_p / (\rho_p c_{pp}) = 0.1$ . Note the response of the particles to the recirculating motion established by the natural convection in the cell as well as their changing temperature. 103

5.1 Examples of the instantaneous Nusselt number vs. time for two different spheres;  $\tau_E$  is the eddy turn-over time. . . . . 125

5.2 Average local Nusselt number over the spheres' surface;  $\theta = 0$  and  $\pi$  are the front and rear stagnation points, respectively. The thick dashed line is for laminar flow; the lightly dashed line is the pure conduction limit  $Nu = 2$ . . . . . 126

5.3 Three examples of the instantaneous local Nusselt number. The solid line is the mean value shown in figure 5.2 and the lightly dashed line the pure conduction limit  $Nu = 2$ . . . . . 126

5.4 Snapshot of the normalized temperature  $T_* = (T - T_p) / (T_i - T_p)$  in the flow studied in this paper; the isosurfaces correspond to  $T_* = 0.8$ . . . . . 127

5.5	Comparison between the time-mean normalized temperature distribution on a plane parallel to the mean velocity through the centers of three contiguous particles for turbulent flow (left) and for laminar flow. . . . .	128
5.6	Contour plot of the normalized average temperature field $(T - T_p)/(T_i - T_p)$ on a plane parallel to the flow direction through the particle center. . . . .	129
5.7	Contour plot of the normalized average streamwise velocity field $u_z/U$ on a plane parallel to the flow direction through the particle center. . . . .	130
5.8	Average normalized temperature deficit $(T_i - T)/(T_i - T_p)$ (upper diagram) and velocity deficit $(U - u_z)/U$ , vs. distance along a line through the particle center parallel to the mean flow; $z/a = 1$ is the rear stagnation point of the particle. . . . .	131
5.9	Probability density function of the temperature along a line through the sphere center parallel to mean flow; the sphere center is at $z = 0$ . From left to right the curves are for $z/a = 1.1, 1.25, 1.5, 2, 3, 8, 17.5$ . . . . .	132
5.10	Probability density function of the streamwise velocity along a line through the sphere center parallel to mean flow; the sphere center is at $z = 0$ . From left to right the curves are for $z/a = 1.1, 1.25, 1.5, 2, 3, 8, 17.5$ . . . . .	133
5.11	Contour plots of the root-mean-square normalized temperature fluctuations defined in equation (5.24). . . . .	134

- 5.12 Dependence of the root-mean-square temperature (upper diagram) and velocity fluctuations vs. distance along a line through the particle center parallel to the mean flow;  $z/a = 1$  is the rear stagnation point of the particle. In the lower diagram the upper two lines show the fluctuations of the two cross-stream velocity components; the thick line is for the streamwise velocity. . . . . 135
- 5.13 Normalized temperature variance  $\sigma_T = \overline{T'^2}/(T_i - T_p)^2$  in the cross-stream direction at different downstream distances from the sphere. In descending order of the maxima, the lines are for  $z/a = 1.25, 1.5, 2, 3$  and  $5$ ; the particle center is on the plane  $x = 0$ . 136
- 5.14 Normalized diagonal turbulent Reynolds stress  $u'_x u'_x / U^2$  (upper diagram) and  $u'_z u'_z / U^2$  in the cross-stream planes at downstream distances from the sphere  $z/a = 1.25, 1.5, 2, 3$  and  $5$ ; the particle center is on the plane  $x = 0$ . . . . . 137
- 5.15 Dependence of the average  $x$  (solid lines) and  $y$  components of the turbulent heat flux on distance from the sphere axis at downstream locations  $z/a = 1.2, 1.5, 2$  and  $3$ ; the particle center is on the plane  $x = 0$ . . . . . 139
- 5.16 Dependence of the average  $z$ -components of the turbulent heat flux on distance from the sphere axis at downstream locations  $z/a = 1.2, 1.5, 2$  and  $3$ ; the particle center is on the plane  $x = 0$ . 139

5.17 The three terms in the energy budget equation (5.25) as functions of the cross-stream coordinate at  $z/a = 1.2$  (upper diagram) and 1.5. . . . . 141

5.18 Mechanical (upper two lines) and thermal time scales, defined in (5.29), as functions of the downstream distance. The dashed line is for turbulent flow without the particles.  $z/a = 1$  is the rear stagnation point of the particle. . . . . 142



# Chapter 1

## Introduction

Particle laden flows, which are characterized by one phase—small, immiscible particles suspended in another continuously connected fluid phase, have a tremendous variety of engineering and scientific applications. In natural systems, examples range from pollution dispersion in the atmosphere and rain cloud formation to formation of planets in the early solar system. A typical engineering application is fluidized beds. These systems consist of fine particles (usually smaller than 5 mm) suspended in an upward gas flow, strong enough that the fluid drag on the particles overcomes gravity. In these conditions the particles are said to fluidize. When in the fluidized state, the moving particles work effectively as a mixer, which results in a uniform temperature distribution and a high mass transfer rate, which are beneficial for the efficiency of many physical and chemical processes. Other engineering applications are aerosol deposition in spray medication and industrial mixing. It is evident that systems of this type are characterized by large separation of scales. Understanding and predicting these complex phenomena is therefore of practical interest for both engineering and environmental problems.

Among all the examples of particle laden flows, particles dispersed and transported in turbulent flows are most commonly encountered and have remained an extreme challenging problem for decades. One of the main difficulties lies in the intrinsic multi-scale nature of turbulence: depending on their size and density, particles will interact with structures of the carrier flow at different time and spatial scales. This is already a complex system even without considering mass or heat transport between the dispersed phase and the continuous fluid. In spite of their common occurrences, our present understanding of these systems is far from complete. For example it is known that particles will form clusters under certain turbulent conditions, but a definite explanation for this complex phenomenon is still awaiting (see e. g. Uhlmann, 2005).

A full understanding of the underlying physical phenomena is crucial to improve the efficiency of processes involving particulate flows. Optical techniques used in experimental investigations are severely constrained by the opacity of the solid phase especially when the particle volume fraction is high. Direct numerical simulation is a promising tool for the study of such systems due to the ever increasing computer power and improved algorithms. Simulation of particulate systems with a large number of fully resolved particles has now become feasible. In the following sections, we briefly describe a few modeling methods for particle laden flows for both isothermal and non-isothermal system and some of their applications.

## 1.1 Modeling methods for particle laden flows

From the point view of simulation, one can broadly distinguish between two-fluid, or Eulerian-Eulerian models and Eulerian-Lagrange models. The first type of models adopts a description in which both phases are treated as continua. A drag force correlation that depends on the relative velocity of the two phases and volume fraction of the solid phase, possibly complemented by other terms describing e.g. added mass effects, is used to account for the interaction between the fluid and solid phases.

In Eulerian-Lagrange models each particle is tracked during the simulation. Particles are allowed to have collisions. In the point-particle model, for the fluid phase, particles are considered as points. The drawbacks of this model are obvious: the particle-fluid interaction is not fully resolved, and a simple drag law correlation is not able to accurately describe some phenomena associated with particles, such as wakes.

An approximate way to account for the finite size of the particles is adopted in the Discrete Element Model. In this model the fluid-particle interaction forces are parametrized as in the point-particle model, but the particle volume fraction is explicitly considered.

Going beyond the approximations used in these models requires a full solution of the Navier-Stokes equations for the fluid and Newton's law of motion for the particles. We refer to computational methods implementing this fundamental approach as Direct Numerical Simulation (DNS). The method described and used in the present dissertation belongs to this class. Some

researchers use the lattice-Boltzmann method for the fluid motion (see e.g. Ladd, 1994a; Ladd, 1994b). More recently, solving the Navier-Stokes equations directly has become more common. We briefly describe some methods developed for this purpose.

## 1.2 Direct Numerical Simulation of particle-laden flow in isothermal system

For the modeling methods at this fundamental level, the equations to be solved are:

$$\nabla \cdot \mathbf{u} = 0, \text{ in } \Omega_f \quad (1.1)$$

$$\frac{\partial \mathbf{u}}{\partial t} + \mathbf{u} \cdot \nabla \mathbf{u} = -\frac{1}{\rho} \nabla p + \frac{\mu}{\rho} \nabla^2 \mathbf{u} + \mathbf{g}, \text{ in } \Omega_f \quad (1.2)$$

$$\text{with } \mathbf{u} = \mathbf{U}_p \text{ on } S_p \quad (1.3)$$

where  $\mathbf{u}$  is the fluid velocity,  $p$  is the pressure,  $\mathbf{g}$  is the gravity and  $\rho$  and  $\mu$  the density and viscosity, respectively. The boundary of the solid body is denoted by  $S_p$ , and the surrounding fluid domain is denoted by  $\Omega_f$ .  $\mathbf{U}_p$  is the velocity of the immersed body on  $S_p$ .

In solving these equations, a key difficulty arises because the particles represent a complex and continually moving boundary for the fluid phase. Generally, the methods used to deal with this problem can be classified into two categories based on whether a fixed grid is, or is not, used for the simulation.

In moving-grid methods, a body-fitted grid is used and the equations are discretized in the computational domain and the boundary condition (equation (1.2)) is enforced directly on the boundary of  $S_p$ . The advantages of this approach are obvious: the grid resolution near the particle surface can be controlled and a better resolution in boundary layers can be achieved in high Reynolds number flows. However, this approach has to deal with the changing of the domain occupied by the fluid. For small changes, i.e., as long as the particles do not move over lengths comparable with their size, simply deforming the grid may be sufficient (Johnson and Tezduyar, 1997). However, after a time long enough that at least some of the particles have moved substantially, a complete grid regeneration is required (Hu, Joseph, and Crochet, 1992), which is usually very cumbersome. Additionally, the solution needs to be projected from the previous mesh to the new mesh after re-meshing. Moreover, generating a good quality body-fitted grid is not straightforward except for simple geometries, and it requires a considerable amount of computational time. Some examples of this kind of methods are the Arbitrary Lagrangian Eulerian (ALE) method (see e.g. Hu, Joseph, and Crochet, 1992; Hu, Patankar, and Zhu, 2001; Gan et al., 2003) and the Deforming-Spatial-Domain/Stabilized-Space-Time (DSD/SST) (see e.g. Johnson and Tezduyar, 1997; Johnson and Tezduyar, 2001).

Because of the drawbacks associated with body-fitted meshes, fixed grid methods have become the mainstream methods for simulating particle-laden flows. Methods based on regular Cartesian grids include the Immersed Boundary (IB) method, the Fictitious Domain method, the Volume of Fluid method

and the PHYSALIS method used in the present work. Among them, the Immersed Boundary method is the most popular one due to its flexibility, with applications from biological flows with elastic boundary at low Reynolds number to rigid body at high Reynolds number. In the following sections, we will briefly introduce Immersed Boundary method and PHYSALIS method.

### **1.2.1 Immersed Boundary Methods**

In Immersed Boundary method, the effect of the immersed body on the flow is imposed by modifying the equation (1.2), namely, adding a source term (forcing term) in the governing equation to mimic the effect of the solid body. Generally, Immersed Boundary methods can be divided into two categories depending on whether this forcing term is imposed on the original Navier-Stokes equation (in the continuum form, called direct forcing methods) or imposed on the discretized Navier-Stokes equation (discrete direct forcing) (Mittal and Laccarino, 2005).

#### **1.2.1.1 Continuous forcing methods**

The idea of imposing a forcing term on the continuous governing equation was first introduced by Peskin (1972), for the simulation of cardiac flow. In this method the fluid equation is solved on a global Cartesian grid and the boundary is defined by a series of Lagrangian points. Two sets of Lagrangian markers are used, one attached to the immersed body while the other set of points moves with the local fluid velocity. The forcing term is calculated from the difference of the position of these two sets of markers through a

constitutive equation.

Since the forcing is computed on the Lagrangian nodes, it must be spread to the surrounding cells. This step is accomplished by means of a distribution function which is essentially a smoothed representation of the delta function. Different forms have been adopted (see figure 1.1). After the Navier-Stokes equation is solved, the fluid velocity is interpolated back to the Lagrangian points and then used to move the Lagrangian points.

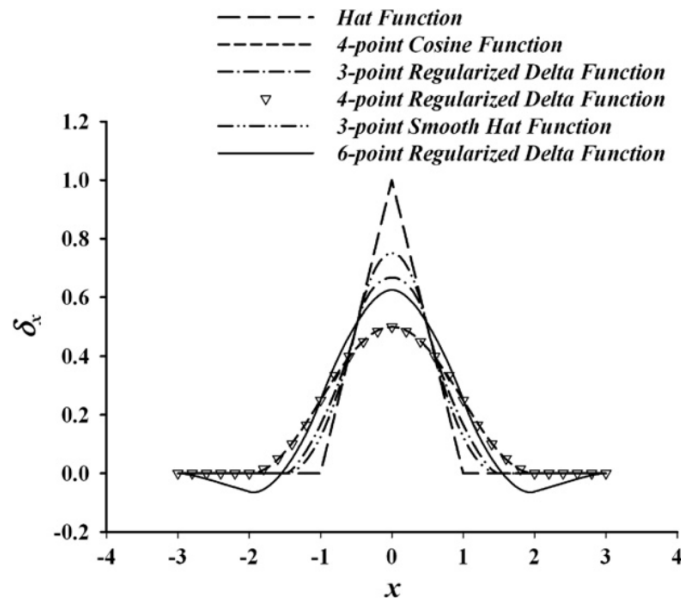


**Figure 1.1:** Delta functions - different delta functions with 2, 3, 4 and 6 cell support. Figure from Haeri and Shrimpton (2012).

Although this formulation can theoretically be used for rigid bodies, it causes numerical difficulties due to a stiffening of the mathematical formulation. To deal with this problem, Lai and Peskin (2000) suggested a forcing in the form of:

$$\mathbf{f} = -\kappa(\mathbf{x} - \mathbf{x}^e), \quad (1.4)$$

with  $\kappa$  a spring constant,  $\mathbf{x}$  the Lagrangian markers and the superscript  $e$  standing for the equilibrium position. However, to approach rigidity, a large  $\kappa$  is required, which also leads to a stiff system of equations and a very small time step. A more general form of the forcing, referred to as feedback forcing, was proposed by Goldstein et al. (1993). It is written in the form of a proportional-integral controller:

$$\mathbf{f} = \alpha \int_0^t (\mathbf{u}(\tau) - \mathbf{u}_r(\tau)) d\tau + \beta (\mathbf{u}(t) - \mathbf{u}_r(t)). \quad (1.5)$$

where  $\mathbf{u}$  is the interpolated velocity at Lagrangian point and  $\mathbf{u}_r$  is the real immersed body surface velocity. The idea of this forcing is to use a term proportional to the current error and a term corresponding to the error history such that it controls the flow velocity on the surface to eliminate the velocity error.

This method has been extensively developed further for more applications. However, it also has some limitations especially for solid bodies since it diffuses their boundary over one or more cells. In addition, spring stiffness and two free parameters are introduced and they are to be determined in a problem-dependent fashion. Moreover, the characteristic time scales of the oscillations of the spring-damper systems can lead to severe restrictions on the time step. Therefore, applications to particle-laden flow simulations are limited. A more widely adopted method is the discrete forcing method, which is introduced below.



### 1.2.1.2 Discrete forcing approach

In the second category of Immersed Boundary methods, the forcing term is applied on the discretized Navier-Stokes equations. This approach, which has been successfully used for a wide range of applications, can be implemented using a discrete direct forcing.

Mohd-Yusof (1997) introduced the discrete direct forcing method. His method overcomes some of the drawbacks of the feedback forcing method, i.e. the severe stability problems and the free parameters. Unlike Peskin's method, in Mohd-Yusof's method there are no Lagrangian points a single Cartesian grid is used and the forcing is directly applied on the Eulerian nodes. If the Navier-Stokes equation is discretized in time, we may write

$$\frac{\mathbf{u}^{n+1} - \mathbf{u}^n}{\Delta t} = RHS^{n+1/2} + \mathbf{f}^{n+1/2}, \quad (1.6)$$

where  $RHS^{n+1/2}$  contains convective and viscous terms and the pressure gradient. The forcing  $\mathbf{f}^{n+1/2}$  is calculated to yield  $\mathbf{u}^{n+1} = \mathbf{U}_f^{n+1}$  on the immersed boundary.

$$\mathbf{f}^{n+1/2} = -RHS^{n+1/2} + \frac{\mathbf{U}^{n+1} - \mathbf{u}^n}{\Delta t}. \quad (1.7)$$

Since forcing and all the terms are discretized on Eulerian node, the value of  $\mathbf{U}^{n+1}$  needs to be interpolated relying on the velocity of the boundary surface and the nearby Eulerian nodes. A simple choice is a one-side linear interpolation.

This method is straightforward and the forcing is direct in the sense the calculated velocities are compatible with the desired velocities on the boundary.

There are no additional unknown parameters introduced in the formulation and the extremely small time used in the continuous forcing method are avoided.

A general problem associated with Mohd-Yusof's method is the strong oscillations of hydrodynamic forces due to insufficient smoothing in the case of moving objects (Uhlmann, 2005). Specifically, a node in the solid can become a fluid node, or vice versa, at the next time step.

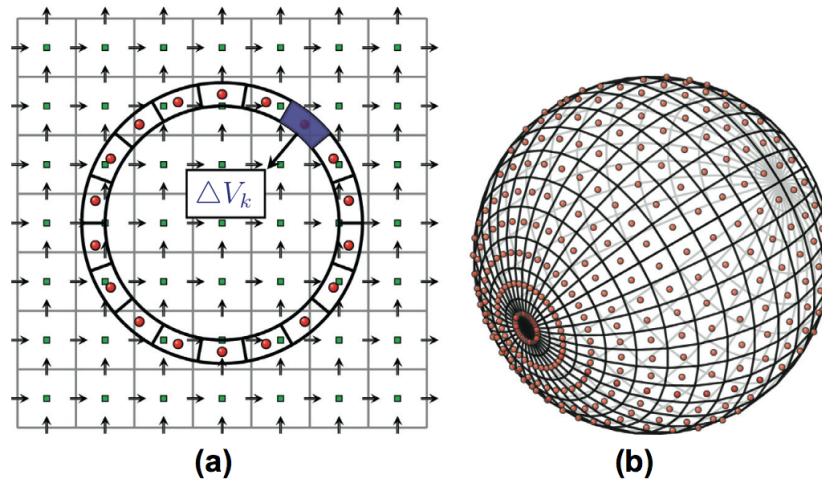


**Figure 1.2:** Illustration of IB (a) A two-dimensional staggered Cartesian grid with an IB. Locations of  $u_x$  and  $u_y$  are represented by horizontal and vertical arrows, respectively. Pressure and temperature are positioned at the center of each cell (green square). Lagrangian points on IB are shown with filled circles (red).  $\Delta V_k$  is a volume that is assigned to each Lagrangian point. (b) Representation of a sphere by Lagrangian points. Figure from Tavassoli et al. (2013).

A big progress to overcome these artificial oscillations was made by Uhlmann (2005), who proposed a method combining some of the best part from Peskin's method and Mohd-Yusof's discrete forcing method, and the method has been widely used since then. Similar to Peskin's method, two sets of grids are used, a fixed global Eulerian grid and a Lagrangian grid defined

on the surface of each immersed body (see figure 1.2). The forcing is computed on the Lagrangian node:

$$\mathbf{f}^{n+1/2} = -RHS^{n+1/2} + \frac{\mathbf{U}_p^{n+1} - \mathbf{u}^n}{\Delta t}, \quad (1.8)$$

$\mathbf{U}_p$  is the solid body velocity on the Lagrangian node, which, for a rigid body, is given by:

$$\mathbf{U}_p = \mathbf{u}_c + \boldsymbol{\Omega}_c \times (\mathbf{x} - \mathbf{x}_c). \quad (1.9)$$

with  $\mathbf{u}_c$ ,  $\boldsymbol{\Omega}_c$  the particle translational/angular velocities and  $\mathbf{x}_c$  the particle center of mass. The form is very similar to Mohd-Yusof's method. However, one significant difference is that all the terms (pressure, velocity) evaluated on the Lagrangian nodes in equation(1.8) need to be interpolated from the nearby Eulerian nodes. After the forcing is computed, they need to be interpolated back to Eulerian nodes. Uhlmann incorporated Peskin's regularized delta function for a smooth transfer between Eulerian and Lagrangian representations, which however has the undesirable effect of preventing a sharp representation of the immersed boundary.

The **ghost-cell method**, introduced by Majumdar, Iaccarino, and Durbin (2001) and Tseng and Ferziger (2003), is different from all the previous methods in that it does not have an explicit forcing added to either the continuous or discrete Navier-Stokes equation. Instead the no-slip boundary condition on the immersed body is enforced by imposing an artificial velocity inside the object through "ghost cells". Besides, there are no Lagrangian points defined and a global Eulerian grid is used for the computation.

As illustrated in figure 1.3, in this method each computational cell is tagged

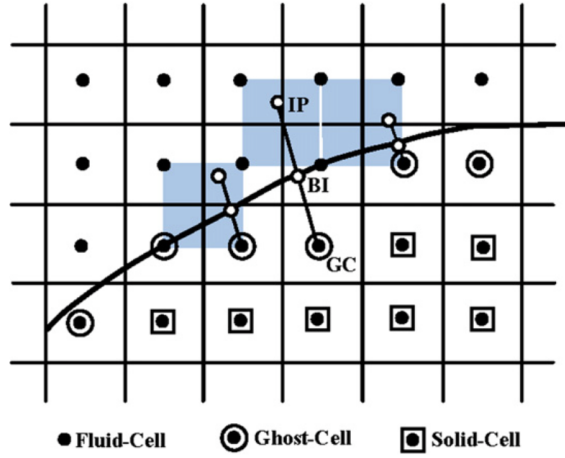


**Figure 1.3:** Ghost cell method: ghost, fluid and solid cells presented. Boundary intersect (BI) point and imaginary point (IP) are also presented for a sample ghost cell. Figure from Mittal et al. (2008).

as either a fluid cell, a solid cell or a ghost cell. A ghost cell is defined as a computational cell inside the solid domain, with at least one neighbor inside the fluid domain. A line segment is extended from each node (e.g., the node identified as *GC* in figure 1.3) of a ghost cell into the fluid normally to the object boundary. An image-point (*IP* in figure 1.3) is defined on this segment to lie in the fluid at the same distance from the boundary as the ghost-cell node under consideration in such a way that the surface point *BI* lies midway between the ghost-cell node and the image point. If a Dirichlet-type boundary condition is to be satisfied, for example for a component  $u$  of the fluid velocity  $\mathbf{u}$ , we write:

$$u_{GC} + u_{IP} = 2u_{IB}. \quad (1.10)$$

The value of  $u_{IP}$  at the image point is interpolated from the surrounding grid points. Different interpolation schemes can be chosen to achieve the desired order of accuracy.

**Cut-cell** method is another method classified under the discrete forcing method. However since the method gets overly complicated for application to moving geometries (Mittal et al., 2008), we will not describe the method here.

### 1.2.2 PHYSALIS method

The PHYSALIS method was developed primarily by Prosperetti and co-workers over the past two decades. The method was first applied to potential flow with many spherical particles (Prosperetti and Oğuz, 2001) and then extended to full Navier-Stokes problems (Zhang and Prosperetti, 2003). Its extension to fluid flows with heat transfer will be presented in Chapter 4 of this thesis. The method is based on the fact that an analytic solution of the field equations locally valid in the immediate neighborhood of each spherical particle can be used as a "bridge" between the particle surface and the adjacent grid points. The coefficients involved in the analytic solution are determined by matching with the finite-difference solution farther away from the particle.

The first applications were to cylinders in two-dimensional flows. Takagi et al. (2003) considered stationary cylinders. The first application to moving particles (cylinders) in a viscous fluid was reported in 2003 where the authors simulated two falling cylinders executing the well-known "drafting, kissing, and tumbling" motion and other examples (Zhang and Prosperetti, 2003). Later on, these authors extended the method to the three-dimensional case, and a general description on how to deal with moving particles are provided (Zhang and Prosperetti, 2005). The matching of the coefficients was executed by solving an over-determined linear system via the singular-value

decomposition. A more efficient method was proposed in Gudmundsson and Prosperetti (2013) by using scalar products of the finite-difference solution with spherical harmonic functions taken over a spherical surface concentric with the particle.

A big progress on the PHYSALIS method was made in Sierakowski and Prosperetti (2016) and Sierakowski (2016), with an implementation on a single GPU-centric code where communication between GPU and the host CPU was reduced to a minimum. In addition to the much-improved efficiency and capability for computation, much progress was made in this new version: a new collision model was developed, a new algorithm aiding the coefficient calculation was implemented and much more. This new code showed a superior ability to control the unphysical oscillations widely observed in most IB method.

Compared to the traditional IB method, advantages of PHYSALIS are exact satisfaction of the no-slip condition at the particle surface, the great simplification of the calculation of the hydrodynamic forces and couples, and the avoidance of the complex issues arising from the lack of geometrical conformity between the curved particle boundary and the underlying fixed Cartesian grid. Furthermore, the use of a local spectral representation of the solution permits one to describe the effect of each particle with fewer degrees of freedom than conventional finite-difference-based methods. As a consequence, the grid resolution can be kept relatively low without compromising the accuracy of the solution (Gudmundsson and Prosperetti, 2013). However, it also has its own limitations. For example, it would be very difficult, if not impossible, to

extend it to non-spherical immersed bodies.

Since 2005, the group have used the tool to study many phenomena in particle-laden flows. They studied wall effects on a rotating sphere (Liu and Prosperetti, 2010), pressure-driven flow in a channel with porous walls (Liu and Prosperetti, 2011) and continuity waves of up to 2000 particles suspended in a vertical liquid stream (Willen et al., 2017). For turbulent particle-laden flow, they performed simulations to learn the interaction between a solid particle and a turbulent flow (Naso and Prosperetti, 2010; Botto and Prosperetti, 2012).

### **1.3 Direct Numerical Simulation methods for non-isothermal systems**

In contrast to the massive interest in DNS methods for isothermal systems, the related problem of heat transfer in particulate flows has received much less attention. Several papers that adopt the point-particle or discrete-element models are available (see e.g. Zonta, Marchioli, and Soldati, 2011; Arcen, Tanière, and Khalij, 2012), but it is only very recently that truly fully-resolved multi-particle simulations have started to appear in the literature. Some of the most common multiphase DNS methods for non-isothermal system include the Volume of Fluid (VOF) method (Pan, 2006), the Arbitrary Lagrangian-Eulerian method (Hu, Patankar, and Zhu, 2001), Immersed Boundary methods (Kim and Choi, 2004; Feng and Michaelides, 2008; Feng and Michaelides, 2009), and Lagrange multiplier/fictitious domain methods (Yu, Shao, and Wachs, 2006; Wachs et al., 2015). We will introduce the IB method and VOF method

in the following sections.

### 1.3.1 Immersed boundary method for non-isothermal system

The energy equation to be solved is

$$\frac{\partial T}{\partial t} + \mathbf{u} \cdot \nabla T = D \nabla^2 T \text{ in } \Omega_f \quad (1.11)$$

with  $D = k/(\rho c_p)$  the thermal diffusivity of the fluid;  $k$  and  $c_p$  are the fluid thermal conductivity and specific heat, respectively;  $T$  is fluid temperature. Temperature field is subjected to conditions at the particle surface temperature, which can be Dirichlet, Neumann or Robin type. We base our discussion on Dirichlet-type boundary conditions first and Neumann-type will be considered later (section 1.3.1.1).

The continuous forcing method described in section 1.2.1.1 is not easily extended to energy equation since a counterpart of the spring system is not well defined for the energy equation. The immersed boundary methods used to solve energy equation all belong to the discrete direct forcing method (section 1.2.1.2), where an explicit or implicit forcing term is added to the discretized Navier-Stokes equation to mimic the effect of solid body. Similarly, a heat source is imposed on the computational nodes to modify the temperature in such a way that the desired temperature on the particle surface is satisfied. If equation (1.11) is discretized in time:

$$\frac{T^{n+1} - T^n}{\Delta t} = RHS^{n+1/2} + q^{n+1/2}, \quad (1.12)$$

$q$  is analogous to  $\mathbf{f}$  in equation (1.7), which mimics the temperature boundary



condition. Extension of the immersed boundary methods to energy equation is straightforward. For example, to extend the method introduced by Uhlmann (2005), a heat source term computed on the Lagrangian nodes is:

$$q^{n+1/2} = -RHS^{n+1/2} + \frac{\tilde{T}^{n+1} - T^n}{\Delta t}. \quad (1.13)$$

where  $\tilde{T}^{n+1}$  is interpolated from the prescribed solid body surface temperature and nearby Eulerian nodes. The heat source is then distributed to surrounding computational nodes.

### 1.3.1.1 Neumann boundary conditions

While the extension of the numerical methods described above for the momentum equations to non-isothermal system with Dirichlet boundary conditions is fairly straightforward, as just described, the case of Neumann boundary conditions requires additional considerations. We summarize some progress made in this specific aspect.

Kim and Choi (2004) used an interpolation procedure to determine the temperature along the wall-normal direction to impose a Neumann-type boundary condition. Their results were compared to those available in the literature for isothermal conditions only. Therefore, the validity of their interpolation scheme for the Neumann condition remains to be assessed.

Pacheco et al. (2005) modified the interpolation proposed by Kim and Choi (2004) to treat the Neumann boundary condition. The authors used bilinear-linear or linear-linear interpolation schemes to treat the Neumann-type boundary condition. The scheme can be applied to both two-dimensional

and three-dimensional body. Pacheco-Vega, Pacheco, and Rodić (2007) further generalized the scheme to handle Dirichlet, Neumann, and Robin (mixed) boundary conditions. Later, to deal with the Neumann boundary condition, Zhang, Zheng, and Eckels (2008) defined a layer of virtual points arranged on a surface parallel to the body surface and one grid spacing separated from it. These virtual points are chosen in the surface normal direction. The temperature at the virtual points is calculated through interpolation from surrounding Eulerian points. The Neumann condition is approximated by the first order one-sided finite difference scheme. Obviously, the additional layer will increase the computational complexity.

A method which avoids using this additional layer of points was proposed by Ren, Shu, and Yang (2013) who used a fractional step procedure. A preliminary temperature field is calculated in the first step and the corresponding heat flux is obtained. The difference between this heat flux and the prescribed heat flux is considered as an additional heat flux which is used to adjust the temperature field, similarly to the discrete direct forcing in the immersed boundary method. The method has been demonstrated to have second-order accuracy in space.

By its very nature, the ghost cell method can naturally treat the Neumann-type boundary condition since the image point is defined along the surface normal direction passing through the ghost cell. In Pan (2010), the image point is chosen at a fixed normal distance into the flow domain. Since only one image point is used, the numerical accuracy drops to first order as found from their results. In order to preserve the second order accuracy, Luo et al. (2016)

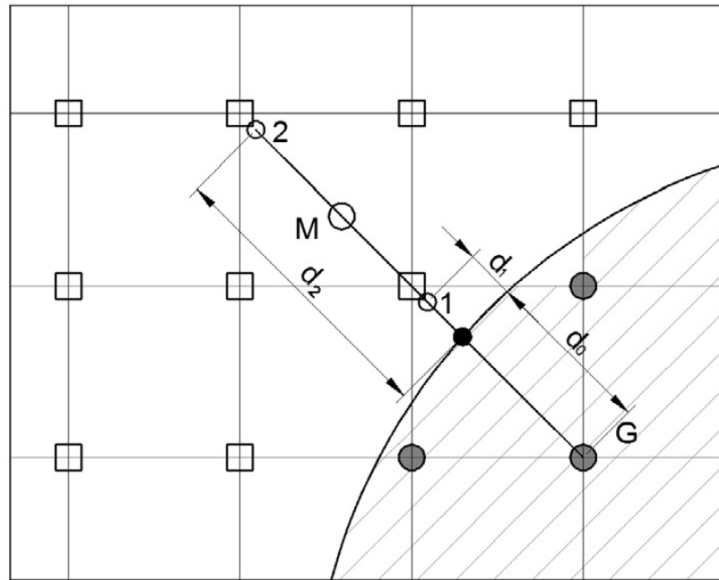


**Figure 1.4:** Neumann or Robin boundary condition with two probe points. Two probe points are point 1 and 2 (Luo et al., 2016).

defined two probe points along the surface normal direction, as illustrated in figure 1.4. The probe points are located at the same distance from the image point, one on the side of the body and the other one on the opposite side. Their position is chosen to guarantee that they belong to different cells. This method was showed to have a second order accuracy. A systematic way to achieve a higher accuracy was proposed by Seo and Mittal (2011) by using a weighted-least square error minimization solution. An example has been demonstrated by Xia, Luo, and Fan (2015) where a third order accuracy was achieved.

### 1.3.2 Volume of Fluid method

There are many industrial liquid-phase applications where solid particles, liquid particles and bubbles co-exist, and in which heat transfer effects are important (e.g. biological treatment of waste water). For applications involving drops or bubbles, the VOF multiphase model is considered as an appropriate framework (Lakehal, Meier, and Fulgosi, 2002). Though VOF was first developed for isothermal system, it was further extended to non-isothermal system and has some successful applications. Ström and Sasic (2013) studied the interaction of a solid particle and a bubble by solving both the momentum and energy equations by the VOF method. Ardekani et al. (2018) used the VOF method for the energy equation only, relying on the immersed boundary method for the momentum equations.

The solution of the momentum equations by the VOF method is well known and will not be described (Hirt and Nichols, 1981). For the energy equation the procedure is the following. The energy equation is written in the one-fluid formulation as:

$$\frac{\partial T}{\partial t} + \nabla \cdot (\mathbf{u}_{cp} T) = \nabla \cdot (D_{cp} \nabla T), \quad (1.14)$$

where

$$\mathbf{u}_{cp} = (1 - \epsilon)\mathbf{u}_f + \epsilon\mathbf{u}_p, \quad (1.15)$$

$$D_{cp} = (1 - \epsilon)D_f + \epsilon D_p. \quad (1.16)$$

$\epsilon$  represents the volume fraction of the solid phase in a computational cell.

$\mathbf{u}_f$  is the fluid velocity and  $\mathbf{u}_p$  the solid-phase velocity, given by the rigid-body motion of the particle;  $D_f$  and  $D_p$  denote the thermal diffusivities of the fluid and solid phases. Equation (1.14) is discretized around the Eulerian cell centers (pressure and temperature points on the Eulerian staggered grid) and solved using the “one fluid” approach, which envisages the equation as describing the temperature in a single medium with variable properties (1.15) and (1.16). In this approach, the disperse and continuous phases share a single temperature field. The condition of continuity of the heat flux across the particle boundaries is implicitly taken into account as explained in Ström and Sasic (2013).

While, in order to reduce the computational cost, the particle Biot number has often been assumed to be infinitesimally small so that the particle interior maintains a uniform temperature, one advantage of the VOF method is that there is no restriction on the particle Biot number. The major drawback of VOF methods is discontinuities of the boundary, or its tangential derivatives (depending on implementations), since the boundary representation is not well conformed with the actual geometry. Therefore, highly refined grids must be used near the body surface.

## **1.4 Applications of multiphase Direct Numerical Simulation methods to non-isothermal systems**

Several examples of the application of the methods described in the previous section can be found in the literature.

A widely studied and common choice for validation of non-isothermal

DNS methods is the uniform flow over a stationary cylinder or a sphere up to  $Re = 500$ , with or without natural convection (see e.g. Bagchi, Ha, and Balachandar, 2001; Kim and Choi, 2004; Liao and Lin, 2012; Xia, Luo, and Fan, 2015; Zhang, Zheng, and Eckels, 2008; Bharti, Chhabra, and Eswaran, 2007; Pan, 2010; Haeri and Shrimpton, 2013; Ren, Shu, and Yang, 2013; Wang et al., 2009; Gan et al., 2003). The dimensionless average heat transfer coefficient (average Nusselt number) of the particle for different Reynolds and Grashof numbers have been compared to experiments and general correlations have been derived. A general trend is that the averaged Nusselt number increases as Reynolds number increases. The local Nusselt number distribution over the particle surface has also been reported, with the maximum value observed at the front stagnation point. Extension to a fluctuating free stream over a stationary cylinder was studied by Alassar and Badr (2007). Later on, Bagchi and Kottam (2008) studied heat transfer of an isotropic turbulent flow over a stationary particle. The authors found that the mean thermal wake behaves similarly to that in a laminar flow. The averaged Nusselt number and local Nusselt number are also reported.

Another widely chosen example for validation is laminar natural convection of a heated cylinder placed eccentrically in a square duct. Pacheco et al. (2005) studied this situation by using an IB method. The cylinder had a fixed temperature, while the vertical side walls of the cavity had equal fixed temperatures, colder than the cylinder, and the horizontal walls were adiabatic. The cylinder was placed slightly above the cavity center. The values of Nusselt number along the cold wall was calculated and compared to experiments at

$Ra = 10^6$  and  $Pr = 10$ . The same simulation has been performed by Kang and Hassan (2011) using a combined IB-lattice Boltzmann method, Feng and Michaelides (2009) using a direct-forcing IB method and Yu, Shao, and Wachs (2006) with the Fictitious Domain method.

Kim et al. (2008) and Lee, Ha, and Yoon (2010) studied a similar problem but all the side walls were isothermal. A heated circular cylinder was placed at different locations in the duct, along the horizontal and vertical lines of symmetry or the diagonal. They show the isothermal lines for different  $Ra = 10^3 \sim 10^6$ . Besides, the local Nusselt number along the surface of the inner cylinder and along the walls of the enclosure were also reported. Pan (2010) studied the same problem but the author simulated the cylinder with both the isothermal and prescribed flux boundary condition. For the same  $Ra$ , the author found that the prescribed heat flux condition resulted in a lower average Nusselt number than the isothermal one. The same simulation has been performed by Badreddine et al. (2017) using an IB method based on a cut-cell approach.

Heat transfer from a heated rotating sphere has been studied for many years due to its application in the areas of drying or cooling, combustion, meteorology. Feng (2014) studied this phenomenon for Reynolds number up to 500 and derived a correlation for the average particle Nusselt number dependence on Reynolds number. Later Liao and Lin (2014) extended the study to include natural convection. The authors stressed the influence of the Rayleigh number, the aspect ratio of the enclosure and the Prandtl number on the heat transfer.

Many situations involve multiple stationary or moving particles and different methods suitable for these applications have been developed in the past decade. For example, flow past a staggered tube bank with heat transfer in two dimensional has been studied by Wang et al. (2009) using a Cartesian grid and Haeri and Shrimpton (2013) using a body-fitted grid. They all reported a total Nusselt number defined in terms of the average temperature at the outflow boundary and compared it favorably with correlations by Grimison (1937).

Steady flow through a random assembly of fixed isothermal particle packings in 3D with the aim to derive correlations were investigated by mainly two groups. Tavassoli et al. (2013) studied the flow over a fixed random array of 54 particles at different  $Re = 10, 50, 100$  and volume fractions  $\epsilon = 0.1, 0.3, 0.5$ . The authors reported the Nusselt number and compared with the correlation given by Gunn (1978) finding a reasonable agreement. Later, the study was extended to non-spherical particles (Tavassoli, Peters, and Kuipers, 2015) and it was found that the shape factor for a non-spherical particle plays a relatively minor role for heat transfer. This finding is contrary to the friction factor behavior in packed beds, where the shape factor has a very significant effect on pressure drop that cannot be fully accounted for by a simple redefinition of the effective radius.

Slight differently, Subramaniam's group focuses on understanding heat transfer phenomena in statistically homogeneous suspensions. Tenneti et al. (2013) found that the current two-fluid CFD models used to solve for heat transfer in gas-solid systems are often not accurate enough to predict



the temperature field and more sophisticated subgrid models are required. Their results were also compared to the correlation of Gunn (1978). In their later work (Sun, Tenneti, and Subramaniam, 2015), a new Nusselt number correlation over a range of  $0 \leq Re \leq 100$  and volume fractions between 0.1 and 0.5 was proposed. More recently, Sun et al. (2016) investigated and modeled the pseudo-turbulent heat flux in a suspension for a wide range of mean slip Reynolds numbers and solid volume fractions. They found that the transport term in the average fluid temperature equation, corresponding to the pseudo-turbulent heat flux, is significant when compared to the average gas-solid heat transfer. They developed an exponential decay model for the average bulk fluid temperature with a decay length scale that depends on the problem parameters.

For moving particles with buoyancy, the heat transfer effects can influence the particle settling velocities, since natural convection in the boundary layer around the particles gives rise to a force that may counterbalance, equate or even exceed the buoyancy force (Yu, Shao, and Wachs, 2006). The special case of zero terminal velocity is known as "thermal levitation" (Mandujano and Rechtman, 2008). The sedimentation of a single particle with heat transfer is governed mainly by the competition between natural and forced convection, which determines boundary layer separation, vortex shedding and the dynamics of the wake. Sedimentation of a hot/cold single particle has been studied by Gan et al. (2003) by using Arbitrary Lagrangian-Eulerian (ALE) method at  $Re = 21$  and  $Gr$  up to  $10^4$ . The authors identified five regimes depending on the different  $Gr$ . Haeri and Shrimpton (2013) studied the same problem

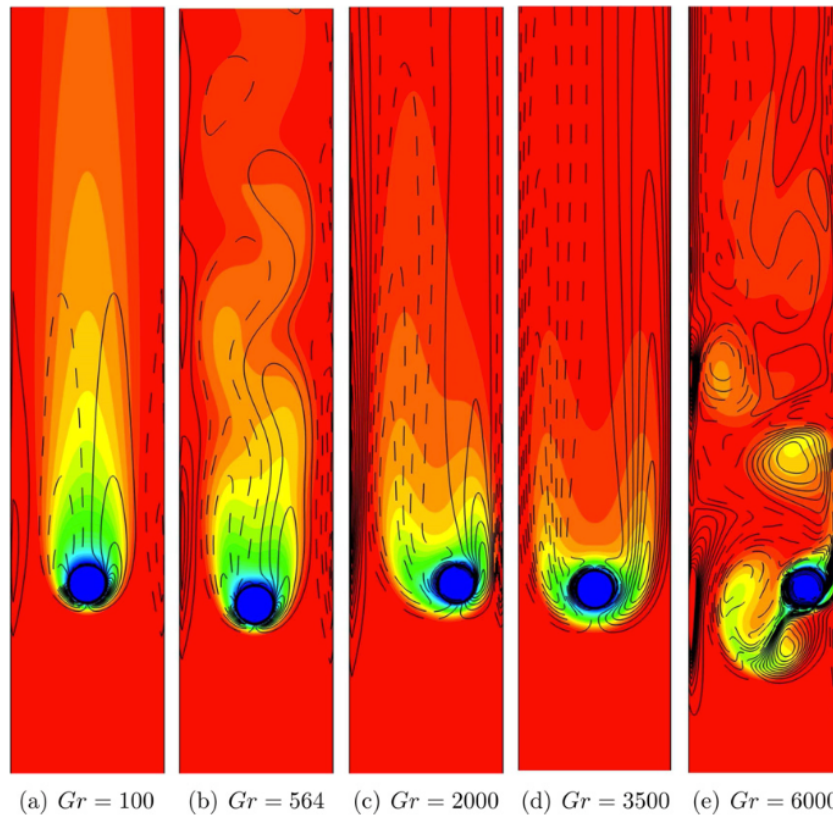


**Figure 1.5:** Vorticity contours superimposed on the temperature contours for different regimes (depend on Grashof numbers). Simulation results by Haeri and Shrimpton (2013).

and found the same regimes, as illustrated in figure 1.5. Up to  $Gr = 500$ , a symmetric and steady wake is observed. As the  $Gr$  increases to 810, periodic vortex shedding is observed which causes regular oscillations of the wake around the particle center-line. Between  $Gr$  is 810 and 2150, particle steadily settles off the center-line near one of the walls. In the fourth regime, particle once again reaches an equilibrium state and has a symmetric wake. When  $Gr$  is larger than 4500, large amplitude oscillation of the trajectory can be found. The streamlines around the hot or cold particles are different from those in the absence of buoyancy. Yu, Shao, and Wachs (2006) simulated the same problem

using the fictitious domain method. Kang and Hassan (2011) used a direct-forcing IB method coupled with two thermal LBM models and compared their results with those of Yu, Shao, and Wachs (2006) and Feng and Michaelides (2008). Liao and Lin (2012) carried out three-dimensional simulations and showed the instantaneous temperature contours near a falling hot sphere at  $Re = 11.6, 32$ . Xia, Luo, and Fan (2015) studied the same problem with a hot sphere cooling while settling. The authors concluded that natural convection dramatically changes the particle velocity, average Nusselt number and local Nusselt number distribution over the particle surface. Gilmanov and Acharya (2008) extended the problem by including the deformation of the particle by coupling the Immersed Boundary method with a Material Point method for the structural stresses and deformation.

Sedimentation of two or more heated or cooled particles have also been studied. The classic “drafting, kissing, and tumbling” motion with energy exchange has been studied by various methods (Feng and Michaelides, 2008; Ström and Sasic, 2013; Gan et al., 2003). Gan et al. (2003) used ALE to simulate a cold or hot sphere pairs for  $Re = O(10)$  and  $Gr$  from 100 to a few thousand. By using an IB method, Feng and Michaelides (2008) demonstrated the drafting-kissing-tumbling phenomenon can be observed at  $Gr$  up to 1000. However, for hot particles, the phenomenon disappears at higher  $Gr$  (of the order of 1500), when a hotter pocket of fluid created by the pair of particles rises and carries the two particles with it. The circulation around the particles has a stabilizing effect and the “tumbling” stage is inhibited. They also simulated a large group of particles sedimenting in a closed enclosure and showed

the formation and motion of clusters.

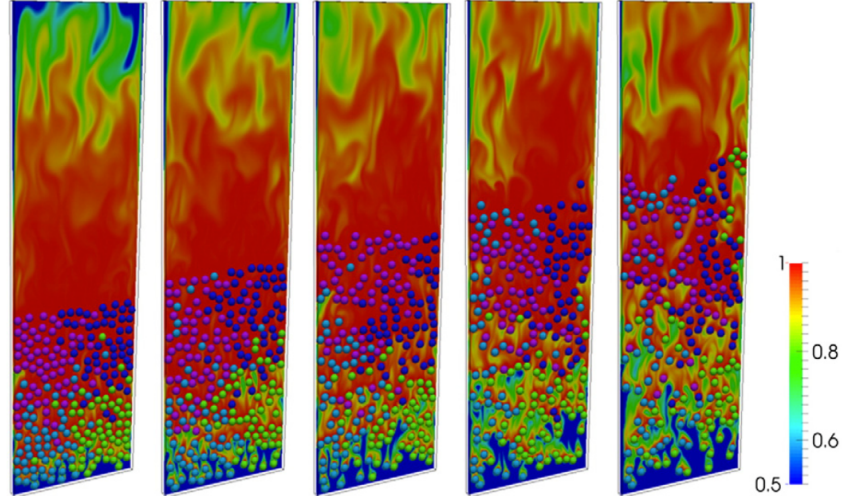


**Figure 1.6:** Temperature distributions at  $t = 5s$  for the five different fluidization velocities:  $V = 0.035, 0.04, 0.045, 0.05,$  and  $0.055$  m/s (from left to right). Simulation results by Feng and Musong (2014).

Another example of multiple and moving particles is fluidization beds. These simulations usually involve a large number of particles, require a massive computational effort and were only carried out very recently. Feng and Musong (2014) simulated 225 spheres and at five different fluidization velocities (figure 1.6). They found that the Nusselt number averaged over all particles increases with the increase of fluidization velocity. Deen et al. (2012) studied the fluidization of 1296 spheres in a pseudo two-dimensional bed. The fluid-particle heat transfer coefficient was calculated and revealed significant spatial variations.

## 1.5 Objectives and organization of this dissertation

This thesis consists of six chapters, including the present one.

In Chapter 2, The mathematical formulation and some implementation details of PHYSALIS are described. An introduction to the problem of forcing the fluid motion is outlined.

In Chapter 3, the results of simulations of an isothermal particle free to rotate in a turbulent flow are described. One objective of this study is to understand the scale of the turbulent vortices that interact most strongly with the particle. Besides, the role of vortex shedding and of Magnus-like lift forces is studied for its significance. The correlations between the fluctuating hydrodynamic force and couple acting on the particle are also calculated.

Chapter 4 focuses on the extension of PHYSALIS method to the energy equation. The analytical solution to the energy equation is developed and its inclusion on an existing code platform developed for the isothermal case is described. Validations and applications of this method are provided together with several examples.

In Chapter 5, we discuss the applications of the method to the thermal wake of particles in a weakly turbulent flow for a particle Reynolds number  $Re_p = 120$ . An analytical solution analogous to the (laminar) Oseen solution is derived for the heat equation in order to better understand the numerical results. The averaged Nusselt number and local Nusselt number distributions over the particle surface are calculated and compared with the uniform flow simulations. The temperature distribution and heat flux evolution in the wake are also described.

## References

- Alassar, R. S. and H. M. Badr (2007). "Heat Convection from a Sphere Placed in a Fluctuating Free Stream". In: *AIChE J.* 53, pp. 1670–1677.
- Arcen, B., A. Tanière, and M. Khalij (2012). "Heat transfer in a turbulent particle-laden channel flow". In: *Int. J. Heat Mass Transfer* 55, pp. 6519–6529.
- Ardekani, M. Niazi, O. Abouali, F. Picano, and L. Brandt (2018). "Heat transfer in laminar Couette flow laden with rigid spherical particles". In: *J. Fluid Mech.* 834, pp. 308–334.
- Badreddine, H., Y. Sato, M. Berger, and B. Ničeno (2017). "A Three-Dimensional, Immersed Boundary, Finite Volume Method for the Simulation of Incompressible Heat Transfer Flows around Complex Geometries". In: *Int J Chem Eng* 2017, p. 1726519.
- Bagchi, P., M. Y. Ha, and S. Balachandar (2001). "Direct numerical simulation of flow and heat transfer from a sphere in a uniform cross-flow". In: *J. Fluids Eng. Trans. ASME* 123, pp. 347–358.
- Bagchi, P. and K. Kottam (2008). "Effect of freestream isotropic turbulence on heat transfer from a sphere". In: *Phys. Fluids* 20, p. 073305.
- Bharti, R. P., R. P. Chhabra, and V. Eswaran (2007). "A numerical study of the steady forced convection heat transfer from an unconfined circular cylinder". In: *Heat Mass Transfer* 43, pp. 639–648.
- Botto, L. and A. Prosperetti (2012). "A fully resolved numerical simulation of turbulent flow past one or several spherical particles". In: *Phys. Fluids* 24, p. 013303.
- Deen, N. G., S. H. L. Kriebitzsch, M. A. Van der Hoef, and J. A. M. Kuipers (2012). "Direct numerical simulation of flow and heat transfer in dense fluid-particle systems". In: *Chem. Eng. Sci.* 81, pp. 329–344.
- Feng, Z. G. (2014). "Direct Numerical Simulation of Forced Convective Heat Transfer From a Heated Rotating Sphere in Laminar Flows". In: *J. Heat Transfer* 136, p. 041707.

- Feng, Z. G. and E. E. Michaelides (2008). "Inclusion of heat transfer computations for particle laden flows". In: *Phys. Fluids* 20, p. 040604.
- Feng, Z. G. and E. E. Michaelides (2009). "Heat transfer in particulate flows with Direct Numerical Simulation (DNS)". In: *Int. J. Heat Mass Transfer* 52, pp. 777–786.
- Feng, Z. G. and S. G. Musong (2014). "Direct numerical simulation of heat and mass transfer of spheres in a fluidized bed". In: *Powder Technol.* 262, pp. 62–70.
- Gan, H., J. Chang, J. J. Feng, and H. H. Hu (2003). "Direct numerical simulation of the sedimentation of solid particles with thermal convection". In: *J. Fluid Mech.* 481, pp. 385–411.
- Gilmanov, A. and S. Acharya (2008). "A computational strategy for simulating heat transfer and flow past deformable objects". In: *Int J Heat Mass Transf* 51, pp. 4415–4426.
- Goldstein, D., R. Handler, and L. Sirovich (1993). "Modeling a No-Slip Flow Boundary with an External Force Field". In: *J. Comput. Phys.* 105, pp. 354–366.
- Grimison, E. D. (1937). "Correlation and utilization of new data on flow resistance and heat transfer for cross flow of gases over tube banks". In: *Trans. ASME* 59, pp. 583–594.
- Gudmundsson, K. and A. Prosperetti (2013). "Improved procedure for the computation of Lamb's coefficients in the PHYSALIS method for particle simulation". In: *J. Comput. Phys.* 234, pp. 44–59.
- Gunn, D. J. (1978). "Transfer of heat or mass to particles in fixed and fluidised beds". In: *Int. J. Heat Mass Transf.* 21, pp. 467–476.
- Haeri, S. and J. S. Shrimpton (2012). "On the application of immersed boundary, fictitious domain and body-conformal mesh methods to many particle multiphase flows". In: *Int. J. Multiphase Flow* 40, pp. 38–55.
- Haeri, S. and J. S. Shrimpton (2013). "A new implicit fictitious domain method for the simulation of flow in complex geometries with heat transfer". In: *J. Comput. Phys.* 237, pp. 21–45.
- Hirt, C. W. and B. D. Nichols (1981). "Volume of fluid (VoF) method for the dynamics of free boundaries". In: *J. Comput. Phys.* 39(1), pp. 201–225.
- Hu, H. H., D. D. Joseph, and M. J. Crochet (1992). "Direct simulation of fluid particle motions". In: *Theor. Comput. Fluid Dynam.* 3, pp. 285–306.
- Hu, H. H., N. A. Patankar, and M. Y. Zhu (2001). "Direct Numerical Simulations of Fluid-Solid Systems Using the Arbitrary Lagrangian-Eulerian Technique". In: *J. Comput. Phys.* 169, pp. 427–462.

- Johnson, A. and T. Tezduyar (1997). "3D Simulation of fluid-particle interactions with the number of particles reaching 100". In: *Comput. Methods Appl. Mech. Eng.* 145, pp. 301–321.
- Johnson, A. and T. Tezduyar (2001). "Models for 3D computations of fluid-particle interactions in spatially periodic flows". In: *Comput. Methods Appl. Mech. Eng.* 190, pp. 3201–3221.
- Kang, S. K. and Y. A. Hassan (2011). "A direct-forcing immersed boundary method for the thermal lattice Boltzmann method". In: *Comput. Fluids* 49, pp. 36–45.
- Kim, B. S., D. S. Lee, M. Y. Ha, and H. S. Yoon (2008). "A numerical study of natural convection in a square enclosure with a circular cylinder at different vertical locations". In: *Int. J. Heat Mass Transfer* 51, pp. 1888–1906.
- Kim, J. and H. Choi (2004). "An immersed-boundary finite-volume method for simulation of heat transfer in complex geometries". In: *KSME Int. J.* 18, pp. 1026–1035.
- Ladd, A. J. C. (1994a). "Numerical simulations of particulate suspensions via a discretized Boltzmann equation. Part I. Theoretical foundation". In: *J. Fluid Mech.* 271, pp. 285–309.
- Ladd, A. J. C. (1994b). "Numerical simulations of particulate suspensions via a discretized Boltzmann equation. Part II: Numerical results". In: *J. Fluid Mech.* 271, pp. 311–339.
- Lai, M. C. and C. S. Peskin (2000). "An Immersed Boundary Method with Formal Second-Order Accuracy and Reduced Numerical Viscosity". In: *J. Comput. Phys.* 160, pp. 705–719.
- Lakehal, D., M. Meier, and M. Fulgosi (2002). "Interface tracking towards the direct simulation of heat and mass transfer in multiphase flows". In: *Int. J. Heat Fluid Flow* 23, pp. 242–257.
- Lee, J. M., M. Y. Ha, and H. S. Yoon (2010). "Natural convection in a square enclosure with a circular cylinder at different horizontal and diagonal locations". In: *Int. J. Heat Mass Transfer* 53, pp. 5905–5919.
- Liao, C.-C. and C.-A. Lin (2012). "Simulations of natural and forced convection flows with moving embedded object using immersed boundary method". In: *Comput. Methods Appl. Mech. Eng.* 213-216, pp. 58–70.
- Liao, C.-C. and C.-A. Lin (2014). "Mixed convection of a heated rotating cylinder in a square enclosure". In: *Int. J. Heat Mass Transfer* 72, pp. 9–22.
- Liu, Q. and A. Prosperetti (2010). "Wall effects on a rotating sphere". In: *J. Fluid Mech.* 657, pp. 1–21.



- Liu, Q. and A. Prosperetti (2011). "Pressure-driven flow in a channel with porous walls". In: *J. Fluid Mech.* 679, pp. 77–100.
- Luo, K., Z. Zhuang, J. Fan, and N. E. L. Haugen (2016). "A ghost-cell immersed boundary method for simulations of heat transfer in compressible flows under different boundary conditions". In: *Int. J. Heat Mass Transfer* 92, pp. 708–717.
- Majumdar, S., G. Iaccarino, and P. Durbin (2001). "RANS solver with adaptive structured boundary non-conforming grids". In: *Annu. Res. Briefs Cent. Turbul. Res.*, pp. 353–364.
- Mandujano, F. and R. Rechtman (2008). "Thermal levitation". In: *J. Fluid Mech.* 606, pp. 105–114.
- Mittal, R. and G. Iaccarino (2005). "Immersed boundary methods". In: *Annu. Rev. Fluid Mech.* 37, pp. 239–261.
- Mittal, R., H. Dong, M. Bozkurttas, F. M. Najjar, A. Vargas, and A. von Loebbecke (2008). "A versatile sharp interface immersed boundary method for incompressible flows with complex boundaries". In: *J. Comput. Phys.* 227, pp. 4825–4852.
- Mohd-Yusof, J. (1997). "Combined immersed boundary/B-spline methods for simulation of flow in complex geometries". In: *Annu. Res. Briefs Cent. Turbul. Res.*, pp. 317–328.
- Naso, A. and A. Prosperetti (2010). "The interaction between a solid particle and a turbulent flow". In: *New J. Phys.* 12, p. 033040.
- Pacheco, J. R., A. Pacheco-Vega, T. Rodić, and R. E. Peck (2005). "Numerical Simulations of Heat Transfer and Fluid Flow Problems Using an Immersed-Boundary Finite-Volume Method on Nonstaggered Grids". In: *Numer. Heat Transfer B* 48, pp. 1–24.
- Pacheco-Vega, A., J. R. Pacheco, and T. Rodić (2007). "A General Scheme for the Boundary Conditions in Convective and Diffusive Heat Transfer With Immersed Boundary Methods". In: *ASME J. Heat Transfer* 129, pp. 1506–1516.
- Pan, D. (2006). "An Immersed Boundary Method for Incompressible Flows Using Volume of Body Function". In: *Int. J. Numer. Meth. Fluids* 50, pp. 733–750.
- Pan, D. (2010). "A Simple and Accurate Ghost Cell Method for the Computation of Incompressible Flows Over Immersed Bodies with Heat Transfer". In: *Numer. Heat Transfer Part B Fundam.* 58, pp. 17–39.
- Peskin, C. S. (1972). "Flow patterns around heart valves: A numerical method". In: *J. Comput. Phys.* 10, pp. 252–271.

- Prosperetti, A. and H. N. Oğuz (2001). “Physalis: A new  $o(N)$  method for the Numerical Simulation of Disperse Systems: Potential Flow of Spheres”. In: *J. Comput. Phys.* 167, pp. 196–216.
- Ren, W., C. Shu, and W. Yang (2013). “An efficient immersed boundary method for thermal flow problems with heat flux boundary conditions”. In: *Int. J. Heat. Mass Transfer* 64, pp. 694–705.
- Seo, J. H. and R. Mittal (2011). “A sharp-interface immersed boundary method with improved mass conservation and reduced spurious pressure oscillations”. In: *J. Comput. Phys.* 230, pp. 7347–7363.
- Sierakowski, A. J. (2016). “GPU-centric resolved-particle disperse two-phase flow simulation using the Physalis method”. In: *Phys. Commun.* 207, pp. 24–34.
- Sierakowski, A. J. and A. Prosperetti (2016). “Resolved-particle simulation by the Physalis method: Enhancements and new capabilities”. In: *J. Comput. Phys.* 309, pp. 164–184.
- Ström, H. and S. Sasic (2013). “A multiphase DNS approach for handling solid particles motion with heat transfer”. In: *Int. J. Multiphase Flow* 53, pp. 75–87.
- Sun, B., S. Tenneti, and S. Subramaniam (2015). “Modeling average gas-solid heat transfer using particle-resolved direct numerical simulation”. In: *Int. J. Heat Mass Transfer* 86, pp. 898–913.
- Sun, B., S. Tenneti, S. Subramaniam, and D. L. Koch (2016). “Pseudo-turbulent heat flux and average gas-phase conduction during gas-solid heat transfer: flow past random fixed particle assemblies”. In: *J. Fluid Mech.* 798, pp. 299–349.
- Takagi, S., H. N. Oğuz, Z. Zhang, and A. Prosperetti (2003). “PHYSALIS: a new method for particle simulation Part II: two-dimensional Navier-Stokes flow around cylinders”. In: *J. Comput. Phys.* 187, pp. 371–390.
- Tavassoli, H., E. A. J. F. Peters, and J. A. M. Kuipers (2015). “Direct numerical simulation of fluid-particle heat transfer in fixed random arrays of non-spherical particles”. In: *Chem. Eng. Sci.* 129, pp. 42–48.
- Tavassoli, H., S. H. L. Kriebitzsch, M. A. Van der Hoef, E. A. J. F. Peters, and J. A. M. Kuipers (2013). “Direct numerical simulation of particulate flow with heat transfer”. In: *Int. J. Multiphase Flow* 57, pp. 29–37.
- Tenneti, S., B. Sun, R. Garg, and S. Subramaniam (2013). “Role of fluid heating in dense gas-solid flow as revealed by particle-resolved direct numerical simulation”. In: *Int. J. Heat Mass Transfer* 58, pp. 471–479.

- Tseng, Y. H. and J. H. Ferziger (2003). "A ghost-cell immersed boundary method for flow in complex geometry". In: *J. Comput. Phys.* 192, pp. 593–623.
- Uhlmann, M. (2005). "An immersed boundary method with direct forcing for the simulation of particulate flows". In: *J. Comput. Phys.* 209, pp. 448–476.
- Wachs, A., A. Hammouti, G. Vinay, and M. Rahmani (2015). "Accuracy of Finite Volume/Staggered Grid Distributed Lagrange Multiplier/Fictitious Domain simulations of particulate flows". In: *Comput. Fluids* 115, pp. 154–172.
- Wang, Z., J. Fan, K. Luo, and K. Cen (2009). "Immersed boundary method for the simulation of flows with heat transfer". In: *Int. J. Heat Mass Transfer* 52, pp. 4510–4518.
- Willen, D. P., A. J. Sierakowski, G. Zhou, and A. Prosperetti (2017). "Continuity waves in resolved-particle simulations of fluidized beds". In: *Phys. Rev. Fluids* 2, p. 114305.
- Xia, J., K. Luo, and J. Fan (2015). "Simulating heat transfer from moving rigid bodies using high-order ghost-cell based immersed-boundary method". In: *Int. J. Heat Mass Transfer* 89, pp. 856–865.
- Yu, Z., X. Shao, and A. Wachs (2006). "A fictitious domain method for particulate flows with heat transfer". In: *J. Comput. Phys.* 217, pp. 424–452.
- Zhang, N., Z. C. Zheng, and S. Eckels (2008). "Study of heat-transfer on the surface of a circular cylinder in flow using an immersed-boundary method". In: *Int. J. Heat Fluid Flow* 29, pp. 1558–1566.
- Zhang, Z. and A. Prosperetti (2003). "A Method for Particle Simulation". In: *J. Appl. Mech* 70(1), pp. 64–74.
- Zhang, Z. and A. Prosperetti (2005). "A second-order method for three-dimensional particle simulation". In: *J. Comput. Phys.* 210, pp. 292–324.
- Zonta, F., C. Marchioli, and A. Soldati (2011). "Time behavior of heat fluxes in thermally coupled turbulent dispersed particle flows". In: *Acta Mech.* 218, pp. 367–373.

# Chapter 2

## PHYSALIS method

We provide here a synthetic description of PHYSALIS method for the (isothermal) Navier-Stokes equations; a detailed description is available in, see e.g. Zhang and Prosperetti, 2005; Gudmundsson and Prosperetti, 2013; Sierakowski and Prosperetti, 2016.

### 2.1 A general solution

The computational domain contains a viscous Newtonian fluid in which several (equal or unequal) spherical particles are suspended. For simplicity we start by considering the case of a single stationary particle. Because of the no-slip condition, the fluid at the particle surface is also stationary and, therefore, its velocity very near the particle will be small. This circumstance allows us to linearize the Navier-Stokes equations around the state of zero motion reducing them, in effect, to the Stokes equations

$$-\nabla p + \mu \nabla^2 \mathbf{u} = 0, \quad (2.1)$$

$$\nabla \cdot \mathbf{u} = 0. \quad (2.2)$$

Of course, away from this thin region (in practice, at distances from the particle surface of the order of the mesh length of the finite-difference discretization) inertia is important and the full Navier-Stokes equations must be solved.

The Stokes equations for a spherical boundary admit a general solution, first given by Lamb (1932) (see also Kim and Karrila, 1991), which somewhat symbolically may be written as:

$$p(\mathbf{x}, t) = \sum_{\ell=1}^{\infty} \sum_{m=-\ell}^{\ell} P_{\ell m}(t) p_{\ell m}(\mathbf{x}), \quad \mathbf{u}(\mathbf{x}, t) = \sum_{\ell=1}^{\infty} \sum_{m=-\ell}^{\ell} U_{\ell m}(t) \mathbf{u}_{\ell m}(\mathbf{x}). \quad (2.3)$$

The precise form of the summations for pressure and velocity is more involved see e.g. Sierakowski and Prosperetti, 2016, but for simplicity we write it in this form which is sufficient to explain the principle of the method. The functions  $p_{\ell m}$  and  $\mathbf{u}_{\ell m}$  are explicitly known in terms of the distance from the particle center and spherical harmonic functions. In particular, the  $\mathbf{u}_{\ell m}$  satisfy exactly the no-slip condition on the particle surface whatever the level of truncation of the infinite summations. At each time step, the time-dependent coefficients  $P_{\ell m}(t)$  and  $U_{\ell m}(t)$  are adjusted so that the local solution (2.3), valid in the immediate neighborhood of the particle, matches the fully non-linear finite-difference solution. In practice, the infinite summations are truncated at  $\ell = \ell_{max}$  which results in the retention of  $3\ell_{max}(\ell_{max} + 2) + 1$  coefficients (the abbreviated notation  $U_{\ell m}$  used in (2.3) actually involves two families of coefficients in addition to the  $P_{\ell m}(t)$ ). Typical values used in our simulations are  $\ell_{max} = 2$  or  $3$ , which result in 25 and 46 coefficients per particle, respectively.

In the more general case in which the particle moves with instantaneous translational and angular velocities  $\mathbf{w}(t)$  and  $\mathbf{\Omega}(t)$ , respectively, we adopt a non-inertial reference frame in which the particle is at rest. If  $\mathbf{u}$  and  $\mathbf{U}$  denote the flow velocities in the particle rest frame and the original inertial frame, respectively, we then have:

$$\mathbf{U} = \mathbf{u} + \mathbf{w} + \mathbf{\Omega} \times \mathbf{r}, \quad (2.4)$$

in which  $\mathbf{r}$  is the position relative to the particle center of mass. The momentum equation in the rest frame takes the form

$$\rho \left( \frac{d\mathbf{u}}{dt} + 2\mathbf{\Omega} \times \mathbf{u} \right) = -\nabla p + \mu \nabla^2 \mathbf{u} + \rho \mathbf{g} - \rho [\dot{\mathbf{w}} + \dot{\mathbf{\Omega}} \times \mathbf{r} + \mathbf{\Omega} \times (\mathbf{\Omega} \times \mathbf{r})], \quad (2.5)$$

to be solved subject to the boundary condition  $\mathbf{u} = 0$  on the particle surface. In equation (2.5) dots denote Lagrangian time derivatives following the particle.

The change of variables

$$\mathbf{u} = \tilde{\mathbf{u}} + \frac{r^5 - a^5}{10\nu r^3} \dot{\mathbf{\Omega}} \times \mathbf{r}, \quad (2.6)$$

$$p = \tilde{p} + \rho(\mathbf{g} - \dot{\mathbf{w}}) \cdot \mathbf{r} + \frac{1}{2}\rho(\mathbf{\Omega} \times \mathbf{r})^2, \quad (2.7)$$

in which  $r = |\mathbf{r}|$  and  $\nu$  is the kinematic viscosity, brings equation (2.5) into the form:

$$\rho \left[ \frac{d\mathbf{u}}{dt} + 2\mathbf{\Omega} \times \mathbf{u} \right] = -\nabla \tilde{p} + \mu \nabla^2 \tilde{\mathbf{u}}. \quad (2.8)$$

with  $\tilde{\mathbf{u}} = 0$  on the particle surface.

It will be noted that the left-hand side of equation (2.8) contains the original velocity in the particle rest-frame,  $\mathbf{u}$ , which equals zero on the particle surface.

Therefore, by continuity, this quantity will be small near the particle and, therefore, there is a region adjacent to the particle where the left-hand side of equation (2.8) is small. Thus, locally,  $(\tilde{\mathbf{u}}, \tilde{p})$  approximately satisfy the Stokes equations (2.1), (2.2).

## 2.2 Implementation

The time advancement of the solution proceeds as follows:

1. Start from a provisional finite-difference solution, typically the solution at the previous time step;
2. By taking suitable scalar products of some components of this solution on a spherical integration surface of radius  $r_s$  concentric with the particle, find a provisional estimate of the coefficients  $P_{\ell m}$  and  $U_{\ell m}$ . For example,  $P_{\ell m}$  would be determined from

$$P_{\ell m} = \left( Y_{\ell}^m, [p(\mathbf{x}, t)]|_{|\mathbf{x}|=r_s} \right) = \int_{\Omega} \overline{Y_{\ell}^m} p(r_s, \theta, \phi) d\Omega, \quad (2.9)$$

in which the overline denotes the complex conjugate,  $\theta$  and  $\phi$  are the angular variables in a local spherical coordinate system centered at the particle center and  $\Omega$  is the solid angle with  $d\Omega = \sin \theta d\theta d\phi$ ;

3. Use (2.3) with the coefficients thus determined to assign boundary conditions to all velocity components on a “cage” of nodes adjacent to the particle surface;
4. Solve the Navier-Stokes equations over the finite-difference grid subject to these assigned velocity boundary conditions on the cage nodes;

5. Repeat to convergence.

There are two reasons why the coefficients determined at step 2 will be different in two successive iterations until the Stokes and Navier-Stokes solutions agree in the immediate neighborhood of the particle. In the first place, the solution (2.3) contains information on four scalar functions, the pressure and the three velocity components, and three additional scalar functions can be derived by calculating the vorticity of the flow. A proper count of the coefficients synthetically indicated by  $P_{\ell m}$  and  $U_{\ell m}$  in (2.3) shows that there are in fact three families of coefficients, and the fact that three families are sufficient to express 7 scalar functions is of course a consequence of the fact that these functions are not independent but are related to each other by the Stokes equations. If the coefficients are incorrect, the 7 scalar functions will be incompatible and this incompatibility will generate different values of the coefficients at the next iteration. Secondly, the coefficients are found on the basis of the field values on the surface of radius  $r_s$  over which the scalar product is evaluated. The expressions (2.3) with the coefficients thus determined are compatible with the velocity values at the cage nodes where the boundary conditions are applied only if the equations are satisfied and, again, this incompatibility contributes to the difference between the coefficient values at two successive iterations until convergence is achieved.

### **2.3 PHYSALIS for arbitrary forcing**

Let  $\mathbf{F}$  be an arbitrary force in the fluid domain, which is twice continuously differentiable. Then the force vector can be decomposed into a curl-free



component and a divergence-free component (Helmholtz decomposition):

$$\mathbf{F} = \mathbf{g} + \mathbf{f}, \quad \text{with} \quad \mathbf{g} = -\nabla\phi, \quad \mathbf{f} = \nabla \times \mathbf{B}. \quad (2.10)$$

By taking  $\mathbf{B}$  to be divergence free,  $\nabla \cdot \mathbf{B} = 0$ , the divergence-free component of the force can further be expressed as:

$$\mathbf{f} = -\nabla^2 \mathbf{A}. \quad (2.11)$$

in which  $\mathbf{A}$  is a vector field.

With an arbitrary force of the form (2.10), the Navier-Stokes equations in the inertial frame are

$$\rho \frac{d\mathbf{U}}{dt} = -\nabla p + \mu \nabla^2 \mathbf{U} + \mathbf{g} + \mathbf{f}. \quad (2.12)$$

By changing the reference frame using equation (2.4), we have:

$$\rho \left( \frac{d\mathbf{u}}{dt} + 2\boldsymbol{\Omega} \times \mathbf{u} \right) = -\nabla p + \mu \nabla^2 \mathbf{u} + \rho(\mathbf{g} + \mathbf{f}) - \rho[\dot{\boldsymbol{\omega}} + \dot{\boldsymbol{\Omega}} \times \mathbf{x} + \boldsymbol{\Omega} \times (\boldsymbol{\Omega} \times \mathbf{r})], \quad (2.13)$$

In order to reduce the right-hand side of the momentum equation to the Stokes form, with the aid of equation (2.11), equation (2.6) is modified to:

$$\mathbf{u} = \tilde{\mathbf{u}} - \frac{r^5 - a^5}{10\nu r^3} \dot{\boldsymbol{\Omega}} \times \mathbf{r} - \frac{\mathbf{A}}{\nu}, \quad (2.14)$$

However, the reduced Stokes equation

$$-\nabla \tilde{p} + \mu \nabla^2 \tilde{\mathbf{u}} = 0, \quad (2.15)$$

now has a non-homogeneous boundary condition:

$$\tilde{\mathbf{u}}|_{r=a} = -\frac{\mathbf{A}}{\nu}|_{r=a}. \quad (2.16)$$

where  $r = a$  is the particle surface.

The general solution to Stokes equation subject to a non-homogeneous boundary condition is given by Kim and Karrila (1991) but its calculation in general is a matter of some complexity. However, in the cases of interest in this work (turbulent forcing, natural convection), the spatial scale of the forcing is much larger than the particle size, which allows us to consider  $\mathbf{f}$  approximately constant and equal to its value at the particle center,  $\mathbf{f} \simeq \mathbf{f}_c$ . With this approximation, equation (2.13) becomes

$$\rho\left(\frac{d\mathbf{u}}{dt} + 2\boldsymbol{\Omega} \times \mathbf{u}\right) = -\nabla p + \mu\nabla^2\mathbf{u} + \rho(\mathbf{g} + \mathbf{f}_c) - \rho[\dot{\mathbf{w}} + \dot{\boldsymbol{\Omega}} \times \mathbf{x} + \boldsymbol{\Omega} \times (\boldsymbol{\Omega} \times \mathbf{r})], \quad (2.17)$$

Reduction to the Stokes form then requires to define  $\tilde{p}$  as

$$p = \tilde{p} + \rho(\mathbf{g} - \dot{\mathbf{w}} + \mathbf{f}_c) \cdot \mathbf{r} + \frac{1}{2}\rho(\boldsymbol{\Omega} \times \mathbf{r})^2. \quad (2.18)$$

This relation is used in Chapter 4.

## References

- Gudmundsson, K. and A. Prosperetti (2013). “Improved procedure for the computation of Lamb’s coefficients in the PHYSALIS method for particle simulation”. In: *J. Comput. Phys.* 234, pp. 44–59.
- Kim, S. and S. J. Karrila (1991). *Microhydrodynamics: Principles and Selected Applications*. Boston MA: Butterworth-Heinemann.
- Lamb, H. (1932). *Hydrodynamics*. 6th edition. New York NY: Dover.
- Sierakowski, A. J. and A. Prosperetti (2016). “Resolved-particle simulation by the Physalis method: Enhancements and new capabilities”. In: *J. Comput. Phys.* 309, pp. 164–184.
- Zhang, Z. and A. Prosperetti (2005). “A second-order method for three-dimensional particle simulation”. In: *J. Comput. Phys.* 210, pp. 292–324.

## Chapter 3

# Rotational dynamics of a particle in a turbulent stream<sup>1</sup>

In this chapter we present results of the fully-resolved numerical simulation of a turbulent flow past a sphere or spherical shell, larger than the Kolmogorov scale, free to rotate around a fixed center. This situation approximates the behavior of a particle whose relative motion with respect to the fluid is driven by external forces, such as density differences in a gravitational field. Holding the center fixed renders possible to have precise information on the turbulent flow incident on the particle by repeating the same simulations without the particle. Two particle Reynolds numbers based on the mean velocity,  $Re_p = 80$  and 150, are investigated; the incident turbulence intensities corresponding to Taylor microscale Reynolds numbers  $Re_\lambda = 36$  and 31, respectively. It is found that, as the Reynolds number of the incident flow increases, the scale of the eddies interacting with the particle also increases because of the particle rotational inertia. The numerical results are inconsistent with a significant

---

<sup>1</sup>This chapter is based on a paper "Rotational dynamics of a particle free to rotate in a turbulent stream" authored by Y. Wang, A. J. Serakowski and A. Prosperetti, submitted to *Phys. Rev. Fluids*.

role of Magnus-like lift forces but indicate the presence of induced vortex shedding at the higher Reynolds number investigated.

### 3.1 Introduction

The development of new experimental techniques and numerical methods (see, e.g., Glowinski et al., 2001; Uhlmann, 2005; Uhlmann, 2008; Mehrabadi et al., 2015; Picano, Breugem, and Brandt, 2015; Noorani et al., 2016) is making possible the study of the interaction of turbulence with particles larger than those for which the earlier point-particle models (see, e.g. Balachandar and Eaton, 2010; Calzavarini et al., 2012) were appropriate. Much of this work has dealt with aspects of the translational motion of particles, such as the statistics of particle velocity and acceleration (Zimmermann et al., 2011b). Less attention has been paid to particle rotation. The rotational intermittency and lift experienced by a neutrally buoyant particle in homogeneous turbulence were studied in Zimmermann et al., 2011a; Zimmermann et al., 2011b. The particle size was comparable to the integral scale and the particle Reynolds numbers were of the order of 1000. They found a strong intermittency of the angular dynamics, with the Probability Density Function (PDF) of the angular acceleration having a flatness of about 7, considerably larger than that of the angular velocity which was close to 4. The root-mean-square (RMS) angular acceleration was found to be of the order of  $(u'/2a)^2$ , with  $u'$  the RMS of the turbulent velocity fluctuations and  $a$  the particle radius. This is an unexpected result for an object of size close to the integral scale. They write “Which properties of the turbulent flow control the rate of rotation of the particle also

remains to be elucidated ... Small eddies acting on the particle in a spatially incoherent manner would result in a significantly reduced torque acting on the particle. This suggests a much more coherent flow pattern, in fact consistent with the recent numerical results of Naso and Prosperetti (2010).”

The extent of the fluid region most influencing the particle motion was also studied in Klein et al. (2013), with the conclusion that flow structures somewhat larger than the particle diameter interacted most strongly. A similar result has been found in studies directed primarily to the investigation of the effects of particle shape, including ellipsoids, disks and rods (Bellani et al., 2012; Byron et al., 2015). While spherical particles were found to have a larger effect on the fluid turbulence than prolate ellipsoids, the auto-covariances of ellipsoids and spheres were statistically identical. From this observation the authors conclude that rotation is controlled by the turbulent scales larger than the particle size. A qualitatively similar result is reported in Parsa and Voth (2014) for the rotational dynamics of neutrally buoyant rods. For all rod lengths, the correlation time of the Lagrangian autocorrelation of the rotation rate scales as the turn-over time of the eddies of the size of the rod.

In the studies mentioned so far neutrally or nearly-neutrally buoyant particles were used. More recently, Mathai et al. (2015), Mathai et al. (2016) used particles with a density significantly smaller than the surrounding liquid. This difference causes a stronger particle-liquid relative velocity, with the development of a wake and vortex shedding. As a consequence, unlike the equal density case, both velocity and acceleration de-correlate at the same rate, which is explained by the determining influence of the vortices shed in the

wake.

In this Chapter, as a step toward a better understanding of the “properties of the turbulent flow [which] control the rate of rotation of the particle”, we use fully resolved numerical simulations to study the rotational dynamics of a single spherical particle free to rotate around its center held fixed in an incident turbulent stream at two Reynolds numbers,  $Re_p = 80$  and  $150$ . By keeping the particle center fixed, and comparing with the identical incident flow in the absence of the particle, we can relate the particle rotational motion to features of the incident turbulence. Our interest lies in particles larger than the Kolmogorov length scale  $\eta$ ,  $a/\eta \sim 11$  to  $13$ , for which inertial effects are important. A point to stress is that the numerical method used in this work leads to a very accurate evaluation of the hydrodynamic couple on the particle, as documented in Gudmundsson and Prosperetti (2013).

The forced stationarity of the particle center approximates the buoyant relative motion studied in Mathai et al. (2015) and Mathai et al. (2016). As in that paper, we find significant effects of vortex shedding induced by the turbulence transported by the mean flow. The significance of Magnus-like forces, however, even if present, is found to be very limited at best. Due to the particle rotational inertia, the scale of eddies interacting with the particle is found to increase with the Reynolds number.

## 3.2 Numerical Method

The simulations are performed with the PHYSALIS method, a complete description of which is available in several papers including, most recently,

Sierakowski and Prosperetti (2016); implementation details are described in Sierakowski (2016). The Navier-Stokes equations are solved on a fixed Cartesian grid by a projection method. A characteristic feature of the method is the way in which the fluid is coupled to the particles, assumed to have no-slip spherical surfaces. The coupling is based on the recognition that, in the vicinity of the particle surfaces, the fluid motion differs little from a rigid-body motion. This circumstance permits the Navier-Stokes equations to be linearized to the Stokes form, for which an exact solution, obtained by Lamb (1932) and Kim and Karrila (1991), is available. This analytical solution is used as a “bridge” between the particle surface and the closest nodes of the Cartesian grid thus bypassing the difficulties deriving from the complex geometrical relationship between the spherical particles and the underlying Cartesian grid. The particle orientation is updated on the basis of the calculated hydrodynamic couple.

The method, which has been extensively validated in earlier papers see e.g. Gudmundsson and Prosperetti (2013) and Sierakowski and Prosperetti (2016), is accurate and efficient. Since the Lamb solution is expressed as a series of spherical harmonics, the error decreases exponentially, rather than algebraically, as the number of degrees of freedom used to describe each particle is increased. This feature is in marked contrast with the algebraic error decrease of most other methods, such as the immersed-boundary method. The no-slip condition at the particle surface is satisfied exactly for any degree of truncation of the series expansion. A unique feature of PHYSALIS, which makes it singularly suitable for the present study, is that the coefficients of the expansion directly furnish the couple acting on the particle with no need for



additional calculations. For these reasons the method furnishes the couple on the particle with a very high degree of accuracy which would be difficult to approach with conventional immersed-boundary methods. In the present work, the Lamb expansion was truncated keeping terms of order 0, 1, and 2, which corresponds to retaining a total of 25 coefficients per particle as in Botto and Prosperetti (2012).

Isotropic, homogeneous turbulence is generated in a  $210 \times 210 \times 210$ -cells cubic domain using the linear forcing scheme of Lundgren (2003), Rosales and Meneveau (2005), and Carroll and Blanquart (2013). This turbulent field, augmented by a constant velocity  $U$  along the  $z$  direction, is imposed at the inlet of an equal domain containing the particle in the manner described in Botto and Prosperetti (2012). The turbulence simulation continues throughout the simulation in such a way that the incident turbulent doesn't exhibit a spurious periodicity. The eddy turn-over time is at least 4 times shorter than the convection time over the length of the computational domain, which ensures the absence of artificial periodicity as discussed in Botto and Prosperetti (2012). We checked that the features of the turbulence, and in particular the intensity and integral length scales, matched the results reported in Rosales and Meneveau (2005).

We use 15 mesh lengths per particle radius  $a$  which, on the basis of our previous experience, provides a very good accuracy in the range of Reynolds numbers relevant for this study. The sides of both domains have a length of  $14a$  so that the area blockage due to the particle is less than 2%. We consider two different particle Reynolds numbers  $Re_p = 2aU/\nu$  (with  $\nu$  the kinematic

$Re_p$		$Re_\lambda$	$\eta/a$	$\lambda_g/a$	$L/a$	$u'/U$	$\eta/\Delta x$
80	Inlet	59.1	0.0445	0.674	2.66	–	0.668
	Particle center	36.1	0.0731	0.862	2.11	1.04	1.10
150	Inlet	47.2	0.0625	0.845	2.66	–	0.938
	Particle center	30.7	0.0907	0.989	2.06	0.413	1.36

**Table 3.1:** Simulation parameters at the inlet plane and at the plane with the particle center plane for  $Re_p = 80$  (upper two lines) and 150;  $Re_\lambda$  is the Taylor microscale Reynolds number defined by  $Re_\lambda = \lambda_g u' / \nu$ ;  $a$  is particle radius;  $\eta$  the Kolmogorov length scale,  $\lambda_g$  the Taylor length scale,  $L$  the integral length scale,  $u'$  the RMS of velocity fluctuations and  $\Delta x$  the mesh length.

viscosity of the fluid),  $Re_p = 80$  and 150. The particle center is fixed at a distance  $7a$  downstream of the inlet boundary in a symmetric position with respect to the lateral boundaries of the domain. The turbulence decays as it is convected toward the particle, and the forcing is adjusted so that, at the plane of the particle center, the values of  $Re_\lambda$  are comparable, 36 for  $Re_p = 80$  and 31 for  $Re_p = 150$ .

### 3.3 Parameter Values

Values of the parameters characterizing the turbulence are shown in Table 3.1. By the time the turbulence has reached the plane of the particle center, the Taylor microscale is comparable to the particle radius, while the Kolmogorov length is more than one order of magnitude smaller. From the last column of the table, showing values of  $\eta/\Delta x$ , it can be seen that the Kolmogorov scale is adequately resolved (see e.g. Pope, 2000, p. 347).

Several time scales are relevant for the present problem. In the first place, the turbulence is characterized by the Kolmogorov time scale  $\tau_K$  and the eddy

turn-over time  $\tau_e$  respectively given by

$$\tau_K = \sqrt{\frac{\nu}{\epsilon}}, \quad \tau_e = \frac{k}{\epsilon}, \quad (3.1)$$

with  $k$  the turbulent kinetic energy and  $\epsilon$  the dissipation, both evaluated at the particle plane. The particle response time to rotational motion is given by

$$\tau_p = \frac{I}{8\pi\mu a^3}, \quad (3.2)$$

where  $I$  is the moment of inertia and  $\mu$  the fluid viscosity. On the basis of these three time scales we can define two Stokes numbers:

$$St_K = \frac{\tau_p}{\tau_K} \quad \text{and} \quad St_e = \frac{\tau_p}{\tau_e}. \quad (3.3)$$

Another important time scale is the convection time past the particle at the velocity of the imposed mean flow:

$$\tau_c = \frac{2a}{U}. \quad (3.4)$$

Upon using the estimate  $\tau_\ell = (\ell^2/\epsilon)^{1/3}$  for the time scale of eddies of spatial scale  $\ell$ , it is possible to show that the convective time scale for  $Re_p = 80$  and  $Re_p = 150$  corresponds to  $\ell/a \simeq 2.13$  and  $\ell/a \simeq 0.406$ , respectively. This suggests that a frozen structure transported by the turbulence in the neighborhood of the particle would have an effect comparable to that of a stationary eddy of size  $\ell$ . The proper scale for the particle angular velocity is the angular velocity of an eddy of the same size of the particle which, for homogeneous isotropic turbulence, can be estimated to be

$$O_{fl} = \frac{1}{2} \left( \frac{\epsilon}{4a^2} \right)^{1/3}. \quad (3.5)$$

$Re_p$	$\tau_c/\tau_e$	$St_K$	$St_e$	$\tau_e O_{fl}$	$\nu\tau_e/a^2$
80	0.669	25.37	1.78	0.778	0.0747
150	0.271	16.33	1.78	0.763	0.0983

**Table 3.2:** Numerical values of several quantities characterizing the simulations;  $\tau_c = 2a/U$  is the convection time past the particle,  $\tau_e$  the eddy turn-over time,  $St_K$  and  $St_e$  the Stokes numbers for the sphere based on the Kolmogorov and turn-over times and  $O_{fl}$ , defined in (3.5), the mean angular velocity of a fluid eddy with the size of the particle.

Numerical values of these scales normalized by  $\tau_e$  are provided in Table 3.2.

We define a dimensionless moment of inertia  $I^*$  by

$$I^* = \frac{I}{\frac{2}{5} \left( \frac{4}{3} \pi a^3 \rho \right) a^2}, \quad (3.6)$$

with  $\rho$  the fluid density. We consider two different values of this quantity,  $I^* = 2$  and  $10/3$ , the latter corresponding to a spherical shell with the same mass as the particle.

For each value of  $Re_p$  and each realization of the turbulent flow, three types of simulations were carried out, one without the particle, one with the “light” particle ( $I^* = 2$ ) and one with the “heavy” particle ( $I^* = 10/3$ ). To mitigate the effect of statistical fluctuations, the results that we present have been obtained by averaging simulations with seven different realizations of the turbulent field, each one lasting between 60 and 100 eddy turn-over times as calculated in correspondence of the inlet conditions. Each particle simulation required about 12 weeks.

For fixed, non-rotating spheres in steady uniform flow experimental values of the drag coefficient  $C_D = F_z / (\frac{1}{2} \pi \rho a^2 U^2)$  are 1.23 for  $Re_p = 80$  and 0.894 for

$Re_p = 150$  (Roos and Willmarth, 1971). The well-known Schiller-Naumann correlation (see e.g. Clift, Grace, and Weber, 1978) gives 1.21 and 0.910 respectively. Drag coefficients in turbulent flow are larger (see e.g. Crowe, Sommerfield, and Tsuji, 1998). In our case, for  $Re_p = 80$  we find  $C_D = 1.31 \pm 0.52$  while, for  $Re_p = 150$ ,  $C_D = 1.05 \pm 0.09$ . The large standard deviation for  $Re_p = 80$  is due to the very strong turbulence intensity (see Table 3.1). Interestingly, the results for the spherical shell are different,  $C_D = 1.06 \pm 0.44$  and  $1.19 \pm 0.15$  for  $Re_p = 80$  and  $Re_p = 150$ , respectively. These results are a consequence of the different rotation dynamics of the two particles, which is affected by their respective moments of inertia as described in the next section. The average values quoted have been calculated over the last 40 turn-over times to avoid the effect of the initial transients.

### 3.4 Results

The two panels in figure 3.1 show the PDF of  $\Omega_{x,y}^*$ , the particle angular velocity components in the cross-stream plane  $(x, y)$ , normalized by  $O_{fl}$ , the angular velocity of eddies having the scale of the particle diameter defined in (3.5):

$$\Omega_{x,y}^* = \frac{\Omega_{x,y}}{O_{fl}}. \quad (3.7)$$

Here  $O_{fl}$  is evaluated on the plane of the particle center in the absence of the particle. The upper panel is for  $Re_p = 80$  and the lower one for  $Re_p = 150$ . The tallest, most peaked curves (red) are for the shell and the next ones (black) for the sphere. The lowest curve (blue) is the PDF for the fluid vorticity averaged over a sphere of radius  $a$  while the other one (yellow) is for the fluid vorticity

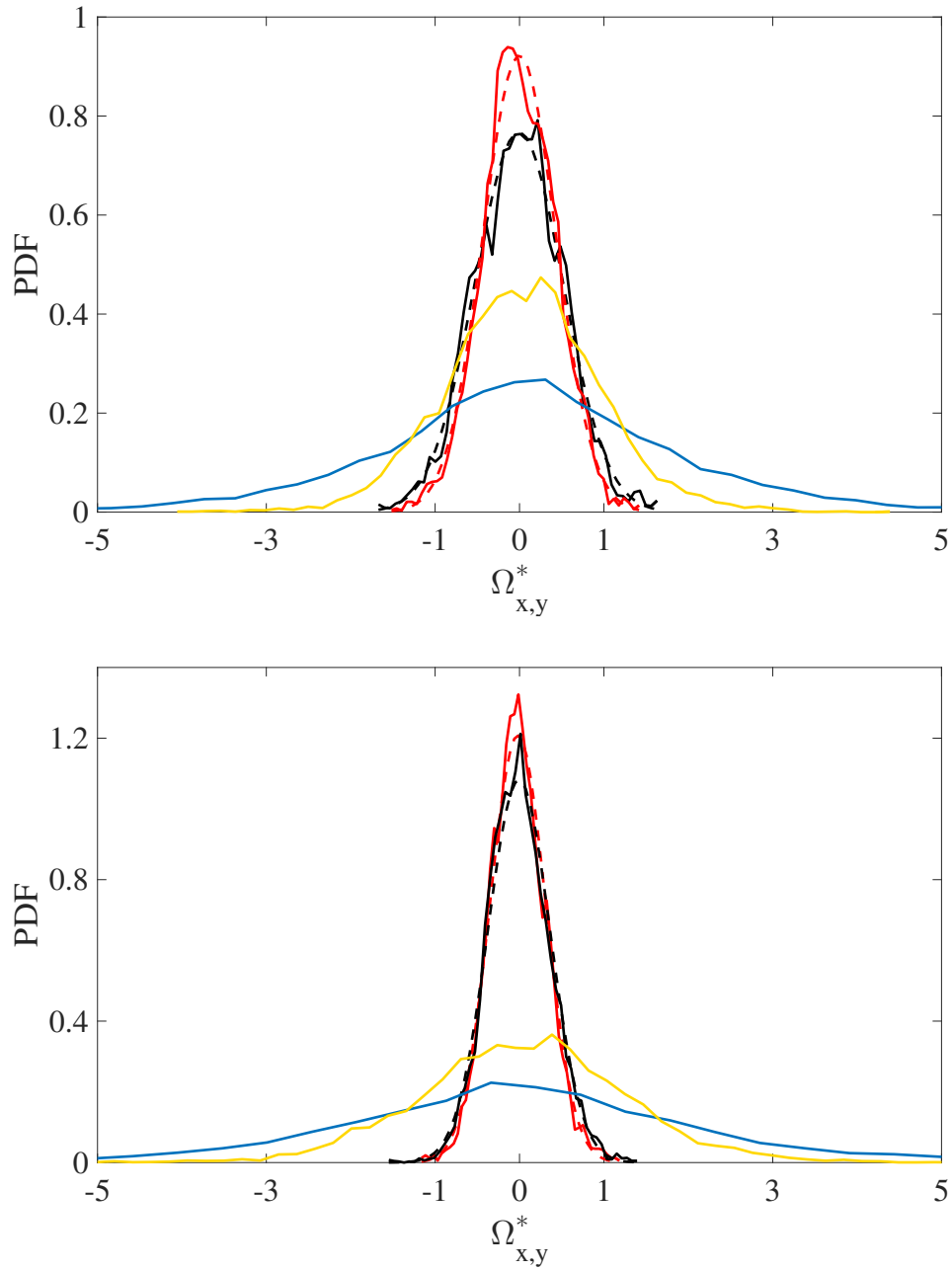


**Figure 3.1:** PDF of the angular velocity in the cross-stream plane  $(x, y)$  normalized as in (3.7) for  $Re_p = 80$  (above) and 150. The highest-peaked (red) and second-highest peaked (black) curves are for the shell and the sphere, respectively. The dashed lines are Gaussian fits. The broadest curve (blue) is for the fluid vorticity averaged over a spherical volume of radius  $a$ ; the other curve (yellow) is for the fluid vorticity averaged over a spherical volume of radius  $2a$ , both centered at the position of the particle center in the absence of the particle.

averaged over a sphere of radius  $2a$ , both calculated in the absence of the particle. The dashed lines are Gaussian fits. The increasing the averaging volume decreases the sensitivity to intermittency, so that the PDF becomes narrower.

The PDF's for the sphere and shell closely approximate Gaussian distributions with a flatness deviating by less than 5% from 3. The PDF's for the angular velocity in the flow direction (not shown) are similar. The PDF's of the averaged fluid vorticity are much broader and exhibit intermittency with a flatness of about 4.2.

The PDF's of the dimensionless couple acting on the particle, defined by

$$\mathbf{L}^* = \frac{\mathbf{L}}{8\pi\mu a^3 O_{fl}} \quad (3.8)$$

are shown in figure 3.2. Unlike the particle angular velocity, these PDF's are non-Gaussian and exhibit a relatively strong intermittency with a flatness of about 4. Qualitatively, these results are comparable to those of Zimmermann et al. (2011a), who found a flatness of about 4 for the angular velocity and of about 7 for the angular acceleration. The difference with our results is probably due to their use of a considerably more intense turbulence with  $Re_\lambda \simeq 300$ . Similar results have also been reported in Mathai et al. (2016).

The RMS values of the three components of the normalized angular velocity and couple are shown in Table 3.3. For both quantities, the components in the cross-stream plane are comparable, as expected. The angular velocities for the sphere are somewhat larger than for the shell as a consequence of the smaller rotational inertia. For the same reason, the couples acting on the shell

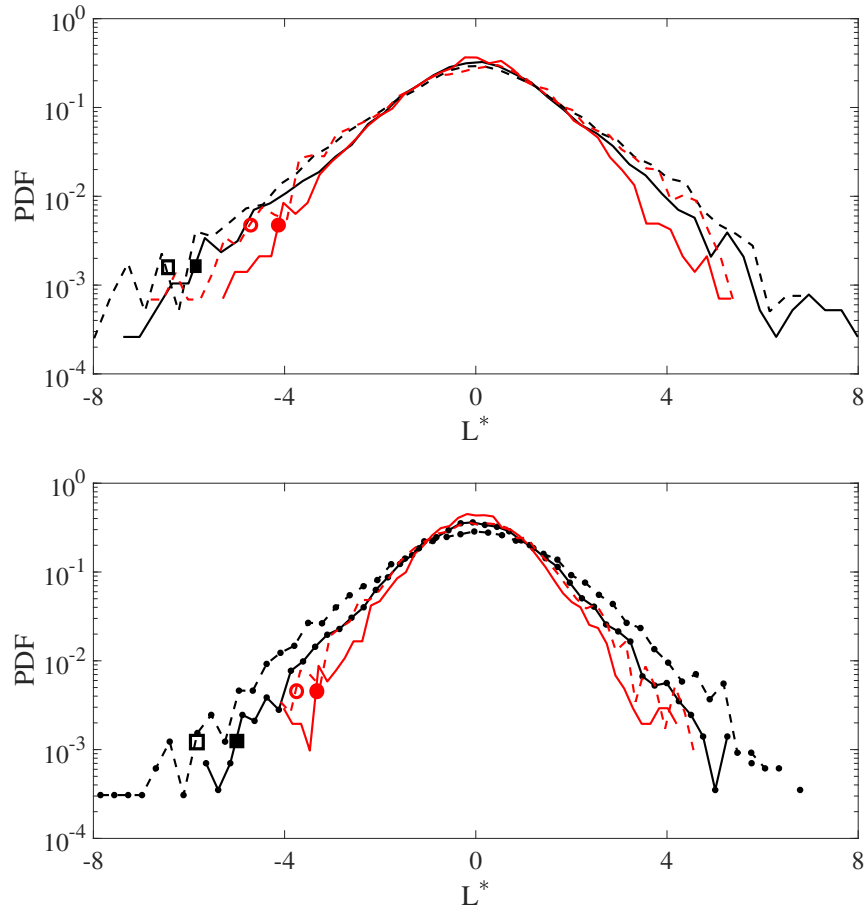


**Figure 3.2:** PDF of the dimensionless couple in the cross-stream plane ( $x, y$ ) (solid black line, squares) and in the direction of the incident flow (red line, circles) normalized as in (3.8) for  $Re_p = 80$  (above) and 150. The solid lines and solid symbols are for the sphere and the dashed lines and open symbols for the spherical shell.



	$Re_p = 80$		$Re_p = 150$	
	sphere	shell	sphere	shell
$\Omega_x^*$	0.580	0.424	0.378	0.328
$\Omega_y^*$	0.492	0.438	0.356	0.329
$\Omega_z^*$	0.503	0.469	0.389	0.306
$L_x^*$	1.525	1.716	1.275	1.630
$L_y^*$	1.469	1.665	1.255	1.517
$L_z^*$	1.295	1.572	1.008	1.193

**Table 3.3:** Root mean square values of the normalized angular velocity and couple components.

are larger than those acting on the sphere. The couples in the flow direction are somewhat smaller than those in the cross-stream plane, likely because of the different way in which the turbulent eddies responsible for rotation in this direction are distorted relative to the other ones. In correspondence with the smaller values of the couple in the direction of the incident stream, one notices also a somewhat weaker intermittency in figure 3.2. In all cases the numbers are of order one, which shows the correctness of the normalizations adopted for these quantities.

A striking feature of figure 3.1 is the much broader spread of the volume-averaged incident vorticity as compared with the particle angular velocity, which extends little beyond the fluid angular velocity at the particle radius. An obvious cause of this difference is the particle rotational inertia and, indeed, the spread of the PDF distribution for the heavy particle is narrower than that for the light one and more peaked around zero. However, these results are compatible with two different interpretations: (1) the particle is sensitive only to relatively large eddies, which however are swept by so quickly that they

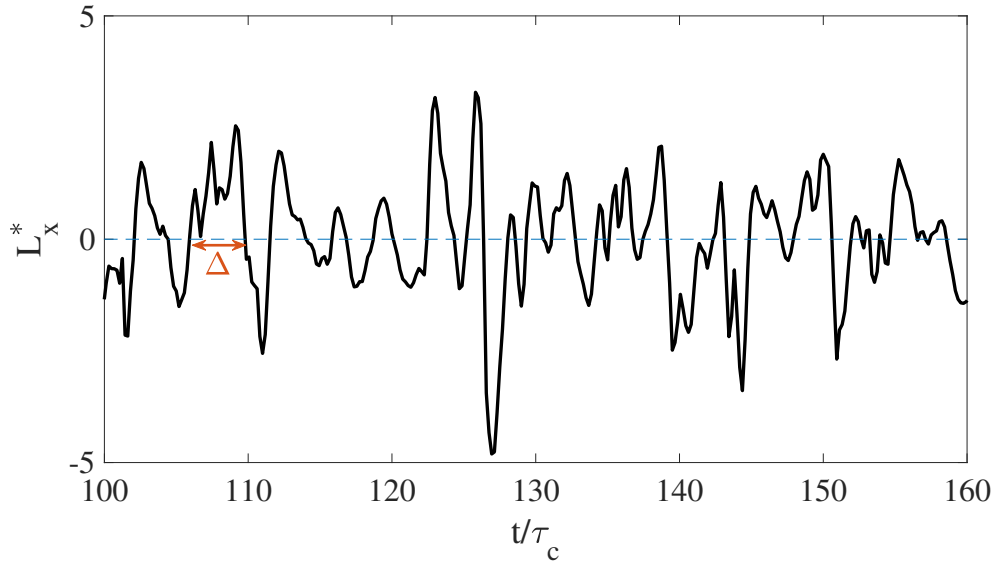


**Figure 3.3:** Time history of  $L_x^*$  for the sphere with  $Re_p = 150$ . Time is normalized by the convection time  $\tau_c = 2a/U$ . The persistence time of the sign is denoted by  $\Delta$ .

do not have time to impart a significant rotational velocity, or (2) the particle is sensitive to eddies of a broad size range which, however, buffet it with couples of random sign and orientation thus preventing it from acquiring a significant angular velocity. Figure 3.3 shows a portion of the time history of one component of the normalized couple acting on the sphere for  $Re_p = 150$ ; time is normalized by the convection time  $\tau_c$ . Rapid sign changes of the couple are evident here, but one also notices a few more extended time intervals, lasting several convection times, in which the couple maintains the same sign.

Ideally, investigating the matter quantitatively could be done with reference to the spectrum of the couple. Unfortunately, we have found that the spectrum converges very slowly and we could not obtain converged results in the available time. For this reason we use an alternative way looking at the sign persistence  $\Delta$  (defined in the figure) of the couple. The solid lines

in figure 3.4 show PDF's of this quantity for the two values of  $Re_p$ . The dashed lines in these figures show the PDF's of the sign persistency of the fluid vorticity, in the absence of the particle, averaged over volumes with radii  $\frac{1}{2}a$  (solid square),  $a$  (solid circle),  $2a$  (open square) and  $3a$  (open circle). The first conclusion to be drawn from these figures is that the most likely sign persistence is considerably shorter than one convection time. For  $\Delta/\tau_c \leq 1$ , at  $Re_p = 80$ , the sign persistence of the couple is intermediate between that of the vorticity averaged over volumes of radius  $\frac{1}{2}a$  and  $a$  while, for  $Re_p = 150$ , it is intermediate between  $a$  and  $2a$ . These comparisons suggest that the size of the eddies responsible for the couple acting on the particle is an increasing function of the particle Reynolds number since, as the Reynolds number increases, the smaller eddies are swept by too quickly to result in a persistent couple. For  $\Delta/\tau_c > 1$ , at  $Re_p = 80$ , the sign of the couple appears to be less persistent than that of the fluid vorticity averaged over volumes of radius  $a$  or larger but more persistent than the vorticity averaged over volumes smaller than  $a$ . For  $Re_p = 150$  the persistence of the couple is less than for averaging volumes of radius  $2a$  or larger. The fact that large eddies have a sign persistence longer than the particle couple implies that, although after averaging the vorticity acquires a definite sign, the detailed structure of these eddies includes smaller eddies of different signs which affect the particle couple. The irregularities evident in these results are due to the strong intensity of the turbulence the effects of which have not been completely removed by the limited averaging over seven realizations used in this work.

The previous considerations as to the size of eddies responsible for the

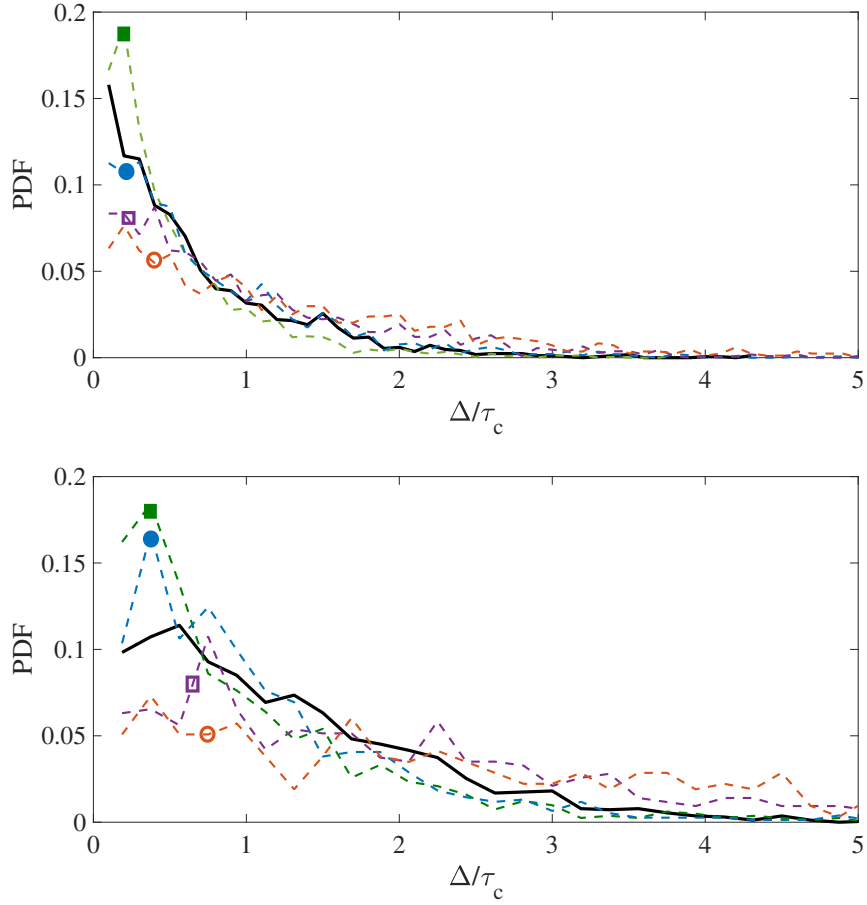


**Figure 3.4:** The solid lines show the PDF's of the sign persistence of the cross-stream plane components of the couple acting on the sphere for  $Re_p = 80$  (upper panel) and  $Re_p = 150$ . The dashed lines are the sign persistence of the cross-stream vorticity in the absence of the particle averaged over spherical volumes with radius  $\frac{1}{2}a$  (solid square),  $a$  (solid circle),  $2a$  (open square) and  $3a$  (open circle).

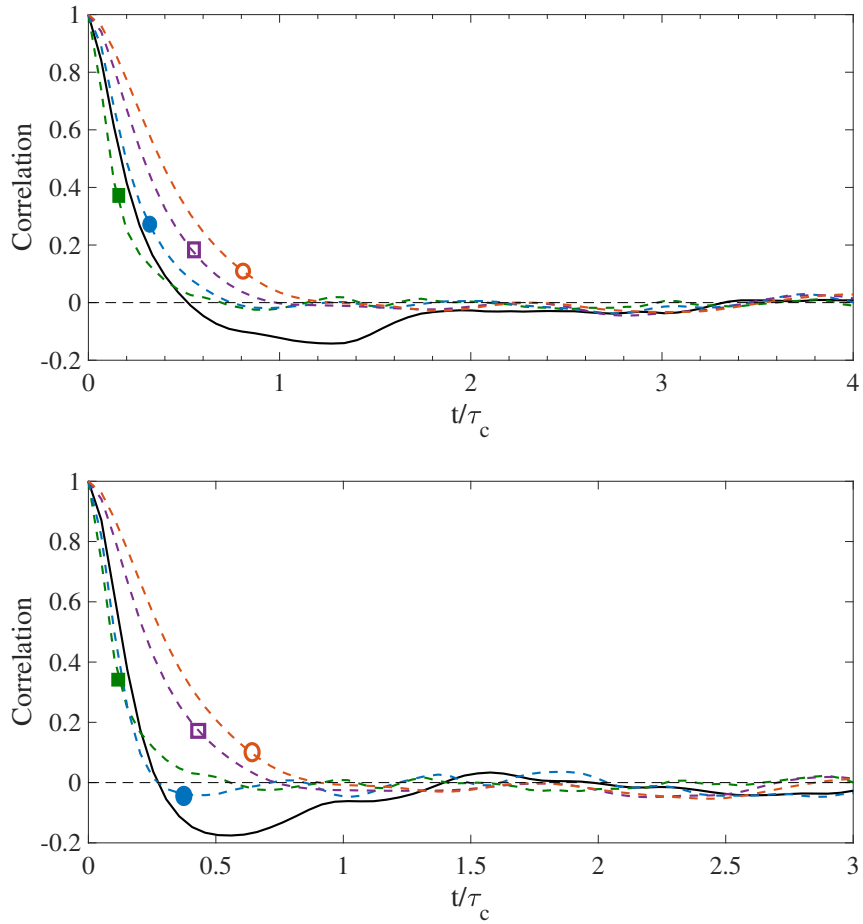


**Figure 3.5:** The solid lines show the auto-correlation of the cross-stream components of the couple acting on the sphere for  $Re_p = 80$  (upper panel) and  $Re_p = 150$ . The dashed lines are the auto-correlations of the vorticity averaged over spherical volumes with radius  $\frac{1}{2}a$  (solid square),  $a$  (solid circle),  $2a$  (open square) and  $3a$  (open circle).

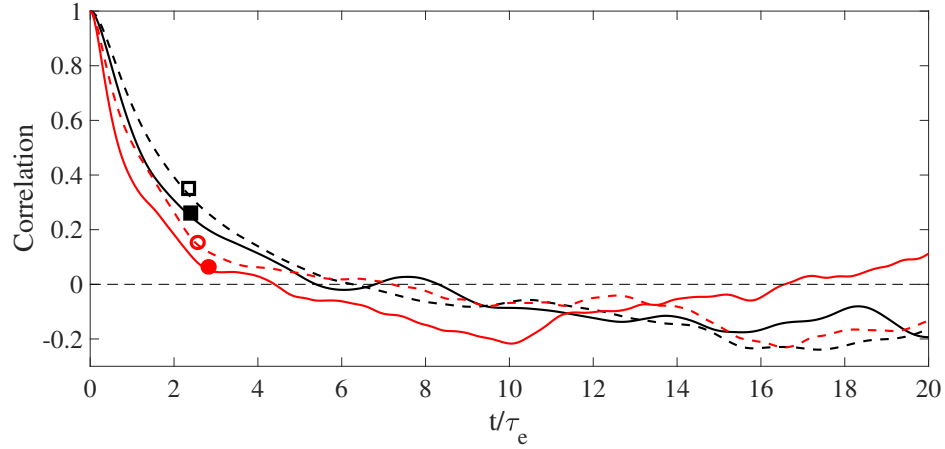


**Figure 3.6:** Auto-correlation of the horizontal components of the particle angular velocity. The solid lines are for the sphere and the dashed lines for the spherical shell. The squares are for  $Re_p = 80$  and the circles for  $Re_p = 150$ .

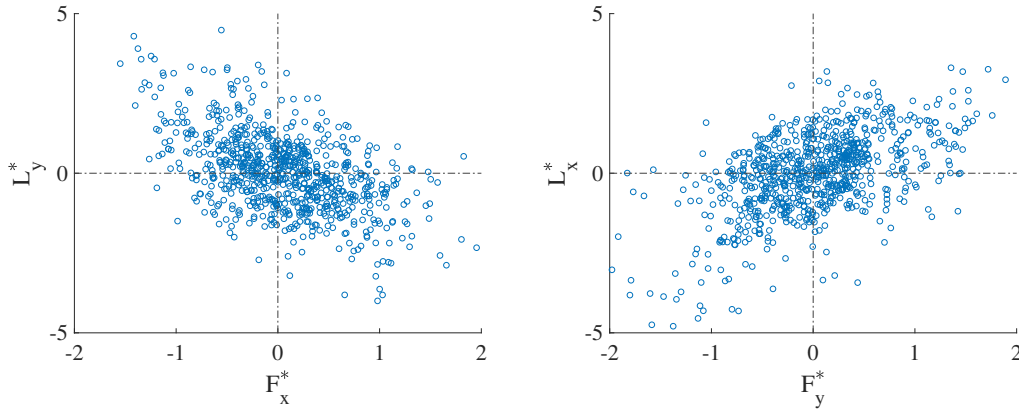
particle couple are confirmed by an analysis of the auto-correlation time of the couple and of the vorticity averaged over volumes of different sizes, which is shown in figure 3.5. Once again we see that, for  $Re_p = 80$ , the couple auto-correlation is closest to that of the vorticity averaged over volumes of radii  $\frac{1}{2}a$  and  $a$  while, for  $Re_p = 150$ , it is intermediate between that of the vorticity averaged over volumes of radii  $a$  and  $2a$ . The particle couple exhibits an extended time during which it is anti-correlated with itself, while the correlation of the averaged vorticity appears to simply decay to zero, the more slowly as the averaging volume increases, with little memory of its previous values. As  $Re_p$  increases, the first zero crossing of the couple occurs earlier and earlier, and significantly before a convection time has elapsed, indicative of the effect of smaller eddies quickly swept by the flow.

Figure 3.6 shows the auto-correlation of the particle angular velocity normalized by the eddy turn-over time. The effect of rotational inertia is evident

in the much longer correlation compared with the couple, in the fact that the first zero crossing for the shell occurs later than for the sphere, and in the longer sign persistence of the angular velocity (not shown). The auto-correlation decays faster at the larger  $Re_p$  for the same reason mentioned before in connection with the zero-crossing of the auto-correlation of the couple.

### 3.5 Forces

Although the force component in the flow direction is dominant, as expected, there are significant forces in the cross stream plane. A possible origin of these components are velocity fluctuations which essentially tilt the mean flow incident on the particle as found, for example, in Botto and Prosperetti (2012). Another possibility is vortex shedding. Although the mean-flow Reynolds numbers considered here are much below the threshold for this phenomenon, which in a uniform steady flow is close to 280 (see e.g. Natarajan and Acrivos, 1993), vortex shedding can be induced by the vorticity transported near the particle by the flow as found in Botto and Prosperetti (2012). These authors found that the vorticity attached on the sphere was occasionally destabilized by an incoming turbulent eddy and consequently shed. To distinguish this phenomenon from the normal vortex shedding, we refer to it as induced vortex shedding. A third possibility, investigated experimentally in Zimmermann et al. (2011a) for a neutrally buoyant particle in a homogeneous turbulent field, is a (pseudo-Magnus) lift force caused by the interaction of the particle rotation with the incident flow (Rubinov and Keller, 1961; Auton, 1987; Bagchi



**Figure 3.7:** Scatter plot of  $L_y^*$  vs.  $F_x^*$  (left) and  $L_x^*$  vs.  $F_y^*$  for the sphere with  $Re_p = 150$ . In spite of the large scatter, a trend compatible with vortex shedding from the particle is clearly visible.

and Balachandar, 2002; Bluemink et al., 2010).

The vortex shedding studied in Mathai et al. (2015) and Mathai et al. (2016) would tend to impose a relation between the sign of the force induced by the shedding and that of the shed vorticity. Indeed, a vortex shed on one side of the particle imparts to it a force directed toward the opposite side and conservation of angular momentum suggests that the particle would tend to rotate in the direction opposite to that of the shed vortex. While this remark is true, it cannot be directly applied to our situation as, when the particle sheds the vortex, it might already be rotating in the “wrong” direction due to prior encounters with turbulent eddies. For this reason it may be better to look at the couple acting on the particle to which, after all, the acquisition of rotation in the “right” direction would be due.

With the present choice of axes, a consideration of the signs of forces and couples shows that a positive/negative  $F_x$  should be associated with a negative/positive  $L_y$ , while  $F_y$  and  $L_x$  should have the same sign. The



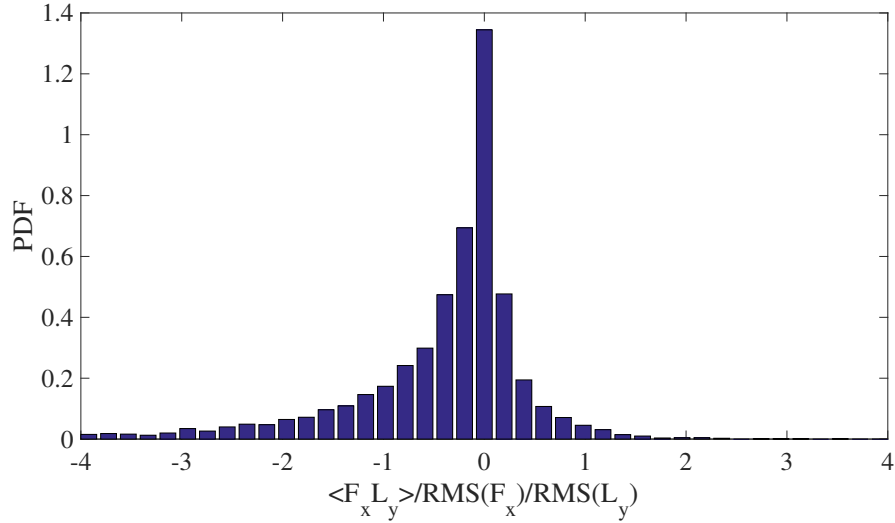


**Figure 3.8:** PDF of the product  $F_x L_y$  normalized by the respective RMS values for the sphere with  $Re_p = 150$ . The prevalence of negative values is compatible with the effect of vortex shedding in generating the cross-stream force component  $F_x$ .

two panels in figure 3.7 show scatter plots of  $L_y^*$  vs.  $F_x^*$  and  $L_x^*$  vs  $F_y^*$  for a single realization with  $Re_p = 150$ ; here the dimensionless force components are defined by

$$\mathbf{F}^* = \frac{\mathbf{F}}{\frac{1}{2}\pi a^2 \rho U^2} \quad (3.9)$$

while  $\mathbf{L}^*$  was defined in equation (3.8). Both figures show a significant amount of scatter, but a general trend compatible with the sign considerations just described is clear. This conclusion can be reinforced by a consideration of figure 3.8, which shows the PDF of the product  $F_x L_y$  normalized by the respective RMS values for all 7 simulations with  $Re_p = 150$ . The bias toward opposite signs is clear here. Numerous instances of vortex shedding can be seen in visualizations of the vorticity distribution. An example is shown in the sequence of figure 3.9.

Turning now to the possibility of a pseudo-Magnus force acting on the

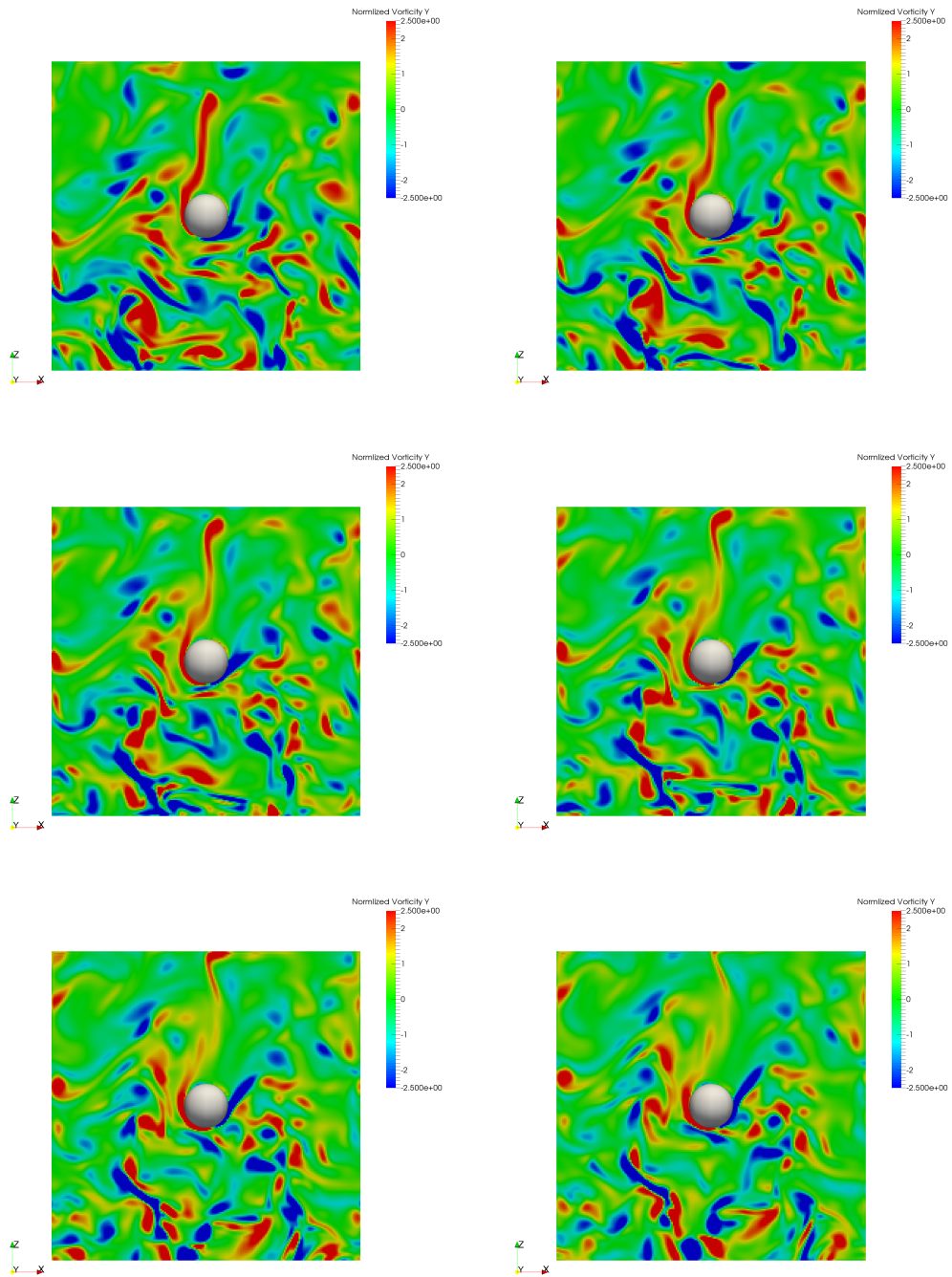


**Figure 3.9:** Six successive images separated by  $0.188 \tau_c$  showing an example of the induced shedding of positive vorticity  $\Omega_y^*$  from the sphere for  $Re_p = 150$ . The color scale ranges over  $-2.5 \leq \Omega_y^* \leq 2.5$ . As a consequence of this process a force  $F_x > 0$  (directed to the right) and a couple  $L_y < 0$  (counterclockwise) act on the particle.

particle we note that, if the incident flow were uniform, the two components of the lift force in the cross-stream plane produced by this mechanism would be

$$F_x = C_L \pi a^3 \rho \left[ \Omega_y (U + u'_z) - \Omega_z u'_y \right], \quad F_y = C_L \pi a^3 \rho \left[ \Omega_z u'_x - \Omega_x (U + u'_z) \right], \quad (3.10)$$

in which  $U$  is the imposed flow,  $u'_{xyz}$  denote the fluctuating velocity components and  $C_L$  is a numerical coefficient of order 1 (Bagchi and Balachandar (2002) report  $C_L \simeq 0.55$ , Auton (1987) reported  $C_L = 2/3$ ). In the present situation, at least for  $Re_p = 150$ ,  $U$  (which is positive) is dominant and therefore we should expect that, to a very rough approximation,

$$F_x \propto \Omega_y, \quad F_y \propto -\Omega_x. \quad (3.11)$$

To test for the presence of a lift force due to this mechanism we show in figure 3.10 the PDF of the product  $F_x \Omega_y$  normalized by the product of the RMS values. The PDF is slightly skewed to the left, showing a slight prevalence of negative values of  $F_x \Omega_y$ , which would be compatible with a vortex shedding mechanism rather than a Magnus force. The analogous PDF for  $F_y \Omega_x$  is very similarly skewed, but in the opposite direction, and leads to the same conclusion. These results suggest that this mechanism, even if it exists, is not dominant. This conclusion is different from that reached in Zimmermann et al. (2011a), but it should be kept in mind that the Reynolds numbers investigated in that paper were much larger than here and the particle was free to move.

Plots analogous to that of figure 3.10 for  $Re_p = 80$  give PDF's that are very nearly symmetric about zero. In this case turbulence intensity is very large

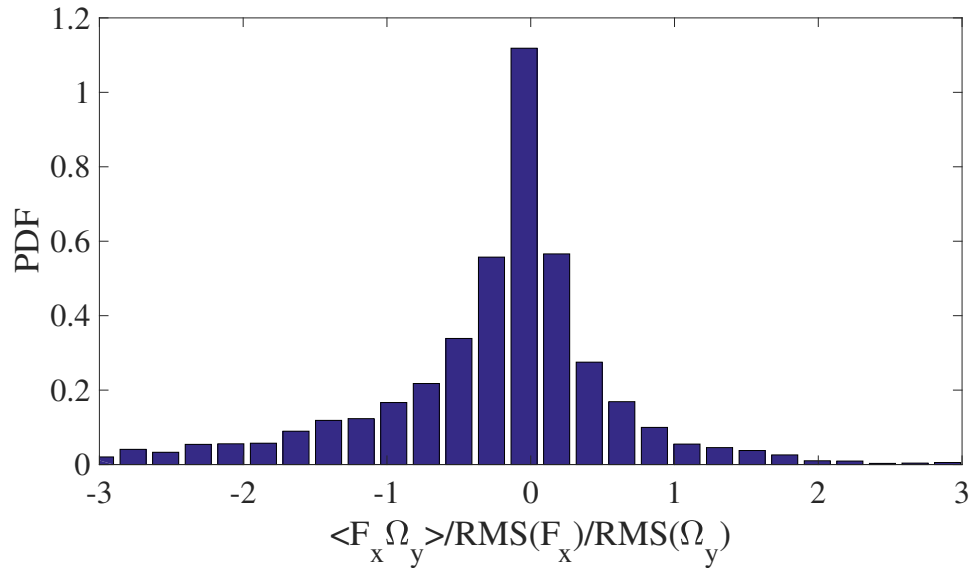


**Figure 3.10:** PDF of the normalized product  $F_x \Omega_y$  for the sphere with  $Re_p = 150$ . A frequent occurrence of a cross-stream force component due to a Magnus-like mechanism would cause a prevalence of positive values of  $F_x \Omega_y$  rather than the negative values indicated by the figure.

(close to 100% in fact, as shown in Table 3.1) and force components in the cross-stream directions are mostly due to the rapidly changing direction of the incident flow rather than to vortex shedding (weakened by the smaller incident velocity) or Magnus mechanisms.

We can analyze these issues further by noting the occurrences of large positive or negative values of  $F_x \Omega_y$  (in practice larger than 1 in modulus in the PDF of figure 3.10) in concomitance with values of  $F_x$  and  $\Omega_y$  with the same or opposite signs. Instants of time when these two quantities have opposite signs are marked by filled (green) circles in the graphs of  $F_x^*$  and  $\Omega_y^*$  vs. time shown in figure 3.11, while instants of time when they have equal signs are marked by open squares (red). It is seen here that, while a few instances of equal signs, compatible with the Magnus mechanism, can be found, they are

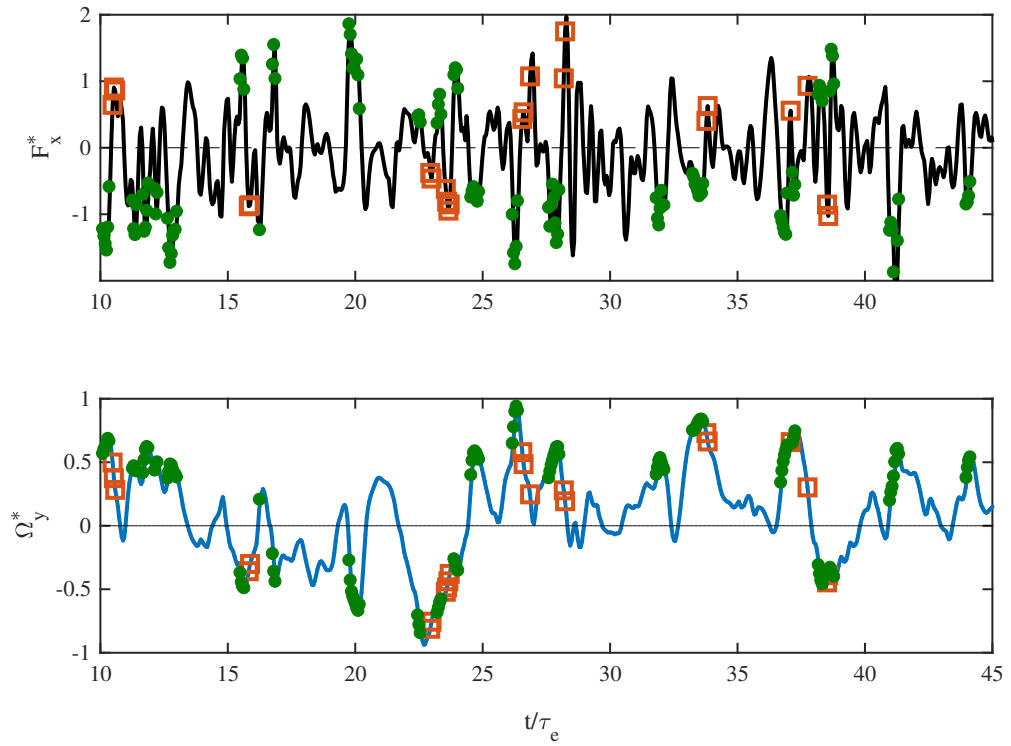


**Figure 3.11:**  $F_x^*$  (upper panel) and  $\Omega_y^*$  vs. time for one realization of the flow past a sphere with  $Re_p = 150$ . The closed circles (green) mark instants where the product  $F_x \Omega_y$  (normalized as in figure 3.10) is less than -1 while at the instants marked by open squares (red) the normalized product  $F_x \Omega_y$  is greater than 1.

far outnumbered by instances in which the two quantities have opposite signs, compatibly with the vortex shedding mechanism. Very similar results are found from the analogous plots of  $F_y^*$  and  $\Omega_x^*$  vs. time.

### 3.6 Summary and Conclusion

In this chapter we have presented results of the fully-resolved numerical simulation of turbulent flow ( $Re_\lambda$  from 31 to 36) past a sphere or spherical shell free to rotate around a fixed center. This situation approximates the behavior of a particle whose relative motion with respect to the fluid is driven by density difference. The somewhat artificial condition imposed by the fixity of the particle center is balanced by the advantage of being able to have precise information on the turbulent flow incident on the particle by repeating the same simulations with the particle removed.

By studying the auto-correlation of the couples acting on the particle and the persistence of their sign we have concluded that, at the lower Reynolds number considered,  $Re_p = 80$ , the particle is mostly influenced by turbulent eddies somewhat smaller than itself. As the Reynolds number of the incident flow increases to  $Re_p = 150$ , the scale of the interacting eddies increases because the rotational inertia requires exposure to the fluid couple over a certain amount of time for the particle to acquire a significant angular velocity. These results are in qualitative agreement with the experimental observations reported in Klein et al. (2013) (at a higher Reynolds number and with  $Re_\lambda = 400$ ) according to which the particle is influenced by flow structures with a scale of the order of its diameter. It may also be noted that the distortion of the

incident eddies caused by interaction with the particle may stretch them to a larger size than without the particle. While vortex structures of these scales appear to be most important for the rotational dynamics of the particle, the high frequency of sign reversals of the couple implies that the effect of these relatively large eddies is modulated by the smaller eddies that they contain.

We have examined the numerical results to detect the presence of cross-stream forces due to vortex shedding and to a Magnus-like mechanism due to the interaction of the particle rotation with the incident flow. Vortex shedding is found to be clearly detectable for  $Re_p = 150$ , in spite of the fact that this Reynolds number is much below that for spontaneous vortex shedding in a uniform flow. The vortex shedding that we find is induced by the interaction with the turbulence transported by the incident flow as in an earlier work (Botto and Prosperetti, 2012). The Magnus mechanism, on the other hand, even if present, cannot account for the frequency and magnitude of the force components in the cross-stream plane that we observe.

## References

- Auton, T. R. (1987). "The lift force on a spherical body in a rotational flow". In: *J. Fluid Mech.* 183, pp. 447–459.
- Bagchi, P. and S. Balachandar (2002). "Effect of free rotation on the motion of a solid sphere in linear shear flow at moderate  $Re$ ". In: *J. Fluid Mech.* 14, p. 2719.
- Balachandar, S. and J. K. Eaton (2010). "Turbulent Dispersed Multiphase Flow". In: *Annu. Rev. Fluid Mech.* 42, pp. 111–133.
- Bellani, G., M. L. Byron, A. G. Collignon, C.R. Meyer, and E. Variano (2012). "Shape effects on turbulent modulation by large nearly neutrally buoyant particles". In: *J. Fluid Mech.* 712, pp. 41–60.
- Bluemink, J. J., D. Lohse, A. Prosperetti, and L. van Wijngaarden (2010). "Drag and lift forces on particles in a rotating flow". In: *J. Fluid Mech.* 643, pp. 1–31.
- Botto, L. and A. Prosperetti (2012). "A fully resolved numerical simulation of turbulent flow past one or several spherical particles". In: *Phys. Fluids* 24, p. 013303.
- Byron, M., J. Einarsson, K. Gustavsson, G. Voth, B. Mehlig, and E. Variano (2015). "Shape-dependence of particle rotation in isotropic turbulence". In: *J. Fluid Mech.* 27, p. 035101.
- Calzavarini, E., R. Volk, E. L ev eque, J.-F. Pinton, and F. Toschi (2012). "Impact of trailing wake drag on the statistical properties and dynamics of finite-sized particle in turbulence". In: *Physica D* 241, pp. 237–244.
- Carroll, P. L. and G. Blanquart (2013). "A proposed modification to Lundgren's physical space velocity forcing method for isotropic turbulence". In: *Phys. Fluids* 25, p. 105114.
- Clift, R. C., J. R. Grace, and M. E. Weber (1978). *Bubbles, Drops, and Particles*. New York NY: Academic Press.
- Crowe, C., M. Sommerfield, and Y. Tsuji (1998). *Multiphase Flows with Droplets and Particles*. Boca Raton FL: CRC.



- Glowinski, R., T. W. Pan, T. I. Hesla, D. D. Joseph, and J. Periaux (2001). "A fictitious domain approach to the direct numerical simulation of incompressible viscous flow past moving rigid bodies: Application to particulate flow." In: *J. Comput. Phys.* 169, pp. 363–426.
- Gudmundsson, K. and A. Prosperetti (2013). "Improved procedure for the computation of Lamb's coefficients in the PHYSALIS method for particle simulation". In: *J. Comput. Phys.* 234, pp. 44–59.
- Kim, S. and S. J. Karrila (1991). *Microhydrodynamics: Principles and Selected Applications*. Boston MA: Butterworth-Heinemann.
- Klein, S., M. Gibert, A. Bérut, and E. Bodenschatz (2013). "Simultaneous 3D measurement of the translation and rotation of finite-size particles and the flow field in a fully developed turbulent water flow". In: *Meas. Sci. Technol.* 24, p. 024006.
- Lamb, H. (1932). *Hydrodynamics*. 6th edition. New York NY: Dover.
- Lundgren, T. S. (2003). *Linearly forced isotropic turbulence*. Tech. rep. Stanford University, pp. 461–473.
- Mathai, V., V. Prakash, J. Brons, C. Sun, and D. Lohse (2015). "Wake-Driven Dynamics of Finite-Sized Buoyant Spheres in Turbulence". In: *Phys. Rev. Lett.* 115, p. 124501.
- Mathai, V., M. Neut, E. van der Poel, and C. Sun (2016). "Translational and rotational dynamics of a large buoyant sphere in turbulence". In: *Exp. Fluids* 57, p. 51.
- Mehrabadi, M., S. Tenneti, R. Garg, and S. Subramaniam (2015). "Pseudo-turbulent gas-phase velocity fluctuations in homogeneous gas?solid flow: fixed particle assemblies and freely evolving suspensions". In: *J. Fluid Mech.* 770, pp. 210–246.
- Naso, A. and A. Prosperetti (2010). "The interaction between a solid particle and a turbulent flow". In: *New J. Phys.* 12, p. 033040.
- Natarajan, R. and A. Acrivos (1993). "The instability of the steady flow past spheres and disks". In: *J. Fluid Mech.* 254, pp. 323–344.
- Noorani, A., G. Sardina, L. Brandt, and P. Schlatter (2016). "Particle transport in turbulent curved pipe flow". In: *J. Fluid Mech.* 793, pp. 248–279.
- Parsa, S. and G. A. Voth (2014). "Inertial Range Scaling in Rotations of Long Rods in Turbulence". In: *Phys. Rev. Lett.* 112, p. 024501.
- Picano, F., W.-P. Breugem, and L. Brandt (2015). "Turbulent channel flow of dense suspensions of neutrally buoyant spheres". In: *J. Fluid Mech.* 764, pp. 463–487.
- Pope, S. B. (2000). *Turbulent Flows*. Cambridge: Cambridge U.P.

- Roos, F. W. and W. W. Willmarth (1971). "Some experimental results on sphere and disk drag". In: *AIAA J.* 9, pp. 285–291.
- Rosales, C. and C. Meneveau (2005). "Linear forcing in numerical simulations of isotropic turbulence: Physical space implementations and convergence properties". In: *Phys. Fluids* 17, p. 095106.
- Rubinov, R. and J. B. Keller (1961). "The transverse force on a spinning sphere moving in a viscous fluid". In: *J. Fluid Mech.* 11, pp. 447–459.
- Sierakowski, A. J. (2016). "GPU-centric resolved-particle disperse two-phase flow simulation using the Physalis method". In: *Phys. Commun.* 207, pp. 24–34.
- Sierakowski, A. J. and A. Prosperetti (2016). "Resolved-particle simulation by the Physalis method: Enhancements and new capabilities". In: *J. Comput. Phys.* 309, pp. 164–184.
- Uhlmann, M. (2005). "An immersed boundary method with direct forcing for the simulation of particulate flows". In: *J. Comput. Phys.* 209, pp. 448–476.
- Uhlmann, M. (2008). "Interface-resolved direct numerical simulation of vertical particulate channel flow in the turbulent regime". In: *Phys. Fluids* 20, p. 053305.
- Zimmermann, R., Y. Gasteuil, M. Bourgoïn, R. Volk, A. Pumir, and J.-F. Pinton (2011a). "Rotational Intermittency and Turbulence Induced Lift Experienced by Large Particles in a Turbulent Flow". In: *Phys. Rev. Lett.* 106, p. 154501.
- Zimmermann, R., Y. Gasteuil, M. Bourgoïn, R. Volk, A. Pumir, and J.-F. Pinton (2011b). "Tracking the dynamics of translation and absolute orientation of a sphere in a turbulent flow". In: *Rev. Sci. Instr.* 82, p. 033906.

## Chapter 4

# A new DNS method –PHYSALIS for non-isothermal system<sup>1</sup>

In this chapter, we will introduce a new DNS method —PHYSALIS for non-isothermal system. As mentioned before, PHYSALIS is an alternative numerical simulation method for the solution of the momentum equations, based on the use of local analytic solutions as “bridges” between the particle surfaces and a fixed underlying Cartesian grid (see, e.g., Gudmundsson and Prosperetti, 2013; Sierakowski and Prosperetti, 2016). The method has several advantages including the possibility of achieving an excellent accuracy with a relatively coarse discretization. In this chapter we describe an extension of the same approach to the energy equation for an incompressible fluid and encounter similar beneficial features. Although the fluid properties are considered constant, natural convection is included in the Boussinesq approximation. The particle Biot number is assumed to be small so that a lumped-capacitance treatment is justified, although extensions to other cases are also possible.

---

<sup>1</sup>This chapter is based on a paper “Fully-resolved simulation of particulate flows with particles-fluid heat transfer” authored by Y. Wang, A.J. Serakowski and A. Prosperetti, published in *J. Comput. Phys.*, vol 350, pp 638-656, 2017.

After stating the mathematical problem, we then describe its extension to the energy equation and provide a verification of the method with several examples with fixed particles. In the final section we show examples in which the particles can move under the action of buoyancy-induced convection.

## 4.1 Mathematical formulation

We consider spherical particles in a non-isothermal, incompressible Newtonian fluid under conditions such that the Boussinesq approximation is applicable. The Navier-Stokes equations then take the form

$$\nabla \cdot \mathbf{u} = 0, \quad (4.1)$$

$$\frac{\partial \mathbf{u}}{\partial t} + \mathbf{u} \cdot \nabla \mathbf{u} = -\frac{1}{\rho} \nabla p + \nu \nabla^2 \mathbf{u} - \beta T \mathbf{g}. \quad (4.2)$$

Here  $\mathbf{u}$  is the velocity field,  $p$  the pressure in excess of a mean hydrostatic pressure,  $T$  the temperature in excess of some constant reference temperature  $T_{ref}$  (so that, here and in the following, in reality  $T$  stands for  $T - T_{ref}$ ) and  $\mathbf{g}$  the acceleration of gravity. The fluid density is denoted by  $\rho$ , the kinematic viscosity by  $\nu$  and the thermal expansion coefficient by  $\beta$ . The energy equation is

$$\frac{\partial T}{\partial t} + \mathbf{u} \cdot \nabla T = D \nabla^2 T, \quad (4.3)$$

with  $D = k/(\rho c_p)$  the thermal diffusivity of the fluid;  $k$  and  $c_p$  are the fluid thermal conductivity and specific heat, respectively. Following the standard procedure in the Rayleigh-Bénard literature, the contribution of the dissipation

function (i.e., viscous heating) is neglected here on account of the smallness of this effect.

For the particles we adopt a simple lumped-capacitance model according to which the particle temperature  $T_p$  is governed by

$$\tau_p \frac{dT_p}{dt} = -\frac{a}{s_p} \oint_{s_p} \nabla T \cdot \mathbf{n}_p ds_p, \quad (4.4)$$

Here  $a$  is the particle radius,  $s_p = 4\pi a^2$  is the particle surface,  $\mathbf{n}_p$  the outwardly-directed unit normal and

$$\tau_p = \frac{\rho_p c_{pp} a^2}{3k}. \quad (4.5)$$

is the particle thermal time constant with  $\rho_p$  and  $c_{pp}$  the particle density and specific heat and  $k$  the fluid thermal conductivity; the right-hand side of (4.4) is the integral of the normal fluid temperature gradient evaluated at the particle surface.

## 4.2 Modification of PHYSALIS method for momentum equation with buoyancy

In extending the method to the non-isothermal case with the Boussinesq approximation, one slight adjustment needs to be made in the way in which the momentum equation is reduced to the Stokes form. In the isothermal case, in transforming the frame of reference to the rest frame of the particle, it is necessary to introduce a modified pressure field  $\tilde{p}$  (equation (2.7)). Due to the adoption of the Boussinesq approximation, in order to reduce the right-hand side of the momentum equation to the Stokes form, it is necessary to eliminate the new Boussinesq term involving the temperature as well. In the immediate

neighborhood of the particle this objective can be achieved very simply, if approximately, by replacing  $T$  by the particle temperature  $T_p$  modifying (2.7) to

$$p = \tilde{p} + \rho(\dot{\mathbf{w}} - \mathbf{g}) \cdot \mathbf{r} + \frac{1}{2}\rho (\boldsymbol{\Omega} \times \mathbf{r})^2 - \beta\rho T_p \mathbf{g} \cdot \mathbf{r}. \quad (4.6)$$

The error incurred with this approximation is small as the temperature in the neighborhood of the particle is close to  $T_p$  and the fluid volume over which the approximation is applied is a thin layer near the particle. A quantitative estimate of this error is provided in the next section. It would also be possible to modify the Lamb solution so as to allow for a spatially varying temperature field, but the necessary analytical and computational effort would be substantial and seems unwarranted given the smallness of the error.

### 4.3 The local solution

Due to the invariance of the convective derivative upon a change of the reference frame, the velocity  $\mathbf{u}$  in equation (4.3) can be considered as the velocity in the rest frame of the particle. This velocity vanishes at the particle surface and, therefore, the convective term  $\mathbf{u} \cdot \nabla T$  will be very small near the particle surface so that equation (4.3) can be simplified to

$$\frac{\partial T}{\partial t} = D\nabla^2 T. \quad (4.7)$$

Changes in the value of the particle temperature reach a distance  $l$  in the fluid after a time of the order of  $l^2/D$ . If this time lag is much smaller than the time scale for the variation of the particle surface temperature, the time derivative

can also be dropped and the equation simply becomes

$$\nabla^2 T = 0. \quad (4.8)$$

The consequences of this quasi-steady approximation will be considered further below and a way to partially correct for the error incurred described.

The solution of equation (4.8) satisfying the condition  $T = T_p^\alpha$  on the surface  $|\mathbf{x} - \mathbf{x}^\alpha(t)| = a$  of the  $\alpha$ -th particle instantaneously centered at  $\mathbf{x}^\alpha(t)$  is given by

$$T(\mathbf{x}, t) = T_p^\alpha(t) + \sum_{\ell=1}^{\infty} \left[ \left( \frac{r}{a} \right)^\ell - \left( \frac{a}{r} \right)^{\ell+1} \right] \sum_{m=-\ell}^{\ell} T_{\ell m}(t) Y_\ell^m(\theta, \phi), \quad (4.9)$$

with  $r = |\mathbf{x} - \mathbf{x}^\alpha(t)|$ , the  $Y_\ell^m$  spherical harmonics and the  $T_{\ell m}(t)$  coefficients to be determined in such a way that the local solution (4.9) matches the solution of the complete energy equation (4.3). The Nusselt number at the particle surface, defined by

$$Nu_p = \frac{Q_p}{2\pi a k T_p}, \quad (4.10)$$

in which  $Q_p$  is the total heat flowing out of the particle,

$$Q_p \equiv - \oint_{s_p} k \nabla T \cdot \mathbf{n}_p ds_p, \quad (4.11)$$

is expressed in terms of the first coefficient  $T_{00}$  of the expansion (4.9) as

$$Nu_p = - \frac{T_{00}(t)}{\sqrt{\pi} T_p}. \quad (4.12)$$

The reader is reminded of the fact that, throughout this chapter,  $T$  denotes the temperature in excess of some reference value.

The coefficients  $T_{\ell m}(t)$  bear to the fluid temperature field evaluated on a

spherical surface of radius  $r_T$  concentric with the particle a relation similar to that shown in equation (2.9), namely

$$\begin{aligned} \left[ \left( \frac{r_T}{a} \right)^\ell - \left( \frac{a}{r_T} \right)^{\ell+1} \right] T_{\ell m}(t) &= \left( Y_\ell^m, [T(\mathbf{x}, t) - T_p(t)]_{|\mathbf{x}|=r_T} \right) \\ &= \int_{\Omega} \bar{Y}_\ell^m [T(r_T, \theta, \phi) - T_p(t)] d\Omega. \end{aligned} \quad (4.13)$$

It may be noted that there is no reason why the radius  $r_T$  of the integration surface used here should equal  $r_s$  used for the evaluation of the momentum integrals.

An approximate way to account for the omission of the time derivative in equation (4.7) consists in setting  $T = T_0 + T_1$  with  $T_0$  satisfying the steady equation (4.8) and  $T_1$  satisfying

$$D\nabla^2 T_1 \simeq \frac{\partial T_0}{\partial t}. \quad (4.14)$$

Since  $T_0$  already accounts for the particle temperature at the particle surface and the fluid temperature on the integration surface  $r = r_T$ , the solution  $T_1$  of equation (4.14) must vanish on these two surfaces. Upon substitution of (4.9) for  $T_0$  in the right-hand side, the equation can be solved with the result

$$\begin{aligned} T_1 &= \sum_{\ell=1}^{\infty} \sum_{m=-\ell}^{\ell} \left[ \left( r^{\ell+2} - \frac{r^\ell a^2 (s^{2\ell+3} - 1)}{s^{2\ell+1} - 1} + \frac{a^{2\ell+3} s^{2\ell+1} (s^2 - 1)}{r^{\ell+1} (s^{2\ell+1} - 1)} \right) A_{\ell m} \right. \\ &\quad \left. - \left( r^{-\ell+1} - \frac{r^\ell (s^2 - 1)}{a^{2\ell-1} (s^{2\ell+1} - 1)} + \frac{a^2 (s^2 - s^{2\ell+1})}{r^{\ell+1} (s^{2\ell+1} - 1)} \right) B_{\ell m} \right] Y_\ell^m(\theta, \phi), \end{aligned} \quad (4.15)$$



in which  $s = r_T/a$ . The coefficients  $A_{\ell m}(t)$  and  $B_{\ell m}(t)$  are given by

$$A_{\ell m} = \frac{\dot{T}_{lm}}{Da^\ell} + \frac{\sqrt{4\pi}}{D} \dot{T}_p \delta_{\ell 0}, \quad B_{\ell m} = \frac{a^{\ell+1}}{D} \dot{T}_{lm}, \quad (4.16)$$

where the superposed dots denote time derivatives. The correction to the temperature gradient at the particle surface is

$$\left. \frac{\partial T_1}{\partial r} \right|_{r=a} = \sum_{\ell=1}^{\infty} \sum_{m=-\ell}^{\ell} \left[ \frac{(2\ell+3)s^{2\ell+1} - (2\ell+1)s^{2\ell+3} - 2}{s^{2\ell+1} - 1} a^{\ell+1} A_{\ell m} - \frac{2s^{2\ell+1} - (2\ell+1)s^2 + 2\ell - 1}{a^\ell (s^{2\ell+1} - 1)} B_{\ell m} \right] Y_\ell^m(\theta, \phi). \quad (4.17)$$

The error incurred in replacing  $T$  by  $T_p$  in the Boussinesq term very near the particle in (4.6) can now be estimated. If the quasi-steady approximation (4.9) is used without the correction (4.15), we define

$$\epsilon_0 = \frac{1}{T_p v_p (s^3 - 1)} \int_a^{r_s} r^2 dr \int_{\Omega} (T_0 - T_p) d\Omega, \quad (4.18)$$

with  $v_p = \frac{4}{3}\pi a^3$  the particle volume, so that  $v_p(s^3 - 1)$  is the volume of the shell between the sphere of radius  $r_T$  and the particle surface. The result is

$$\epsilon_0 = \frac{1}{2\sqrt{4\pi}} \frac{(2s+1)(s-1)}{s^2 + s + 1} \frac{T_{00}}{T_p}. \quad (4.19)$$

We see from (4.13) that

$$(s-1)T_{00} = \frac{s}{\sqrt{4\pi}} \int_{\Omega} [T(r_T, \theta, \phi) - T_p(t)] d\Omega, \quad (4.20)$$

so that, since  $s$  is taken close to 1,  $\epsilon_0$  is of the order of the mean temperature difference between  $T_p$  and  $T(r_T, \theta, \phi)$  divided by  $4\pi T_p$ . In applications  $T_p - T(r_T, \theta, \phi)$  is a small fraction of  $T_p$  and, if the error incurred with the

approximation is considered as a re-definition the Rayleigh number based on the particle temperature and radius, the effect will be very small. By including the correction (4.15),  $\epsilon_0$  is augmented by

$$\begin{aligned}\epsilon_1 &\equiv \frac{1}{T_p v_p (s^3 - 1)} \int_a^{r_T} r^2 dr \int_{\Omega} T_1 d\Omega \\ &= - \frac{(s-1)^2 a^2}{20\sqrt{4\pi}(s^3-1)DT_p} \left[ (s-1)(8s^2+9s+3)\dot{T}_{00} + \frac{1}{\sqrt{\pi}}(4s^2+7s+4)\dot{T}_p \right].\end{aligned}\tag{4.21}$$

which is again small.

As a concluding comment it may be noted that, in place of (4.9) or (4.15), one could use the exact solution of the diffusion equation (4.7) which, however, would involve a convolution integral and make the calculation significantly more complex. Secondly, the form (4.9) of the local solution is suitable when the particle surface temperature is spatially uniform as assumed here with the use of the lumped capacitance approximation. A similar expansion can be written down whatever the particle surface temperature distribution. However, if the time scale for temperature homogeneization in the particle cannot be neglected, it becomes necessary to solve the conduction equation inside the particle and, again, the complexity of the calculation increases significantly.

## 4.4 Implementation

Here we describe a straightforward implementation of the mathematical model formulated in the previous section. Since much of it is the same as for the isothermal PHYSALIS implementation, which is described briefly in

Chapter 2 and in detail in: Gudmundsson and Prosperetti, 2013; Sierakowski and Prosperetti, 2016, we focus here mainly on the novel aspects that are introduced by the energy equation.

The equations are discretized on a staggered uniform grid with second-order accuracy. Time stepping is first-order accurate and explicit, which requires a limitation on the time step  $\Delta t$  given by

$$\Delta t = \frac{C}{\frac{\max|u_i|}{\Delta x} + \frac{2\min(\nu, D)}{\Delta x^2}}. \quad (4.22)$$

The maximum is over all the velocity components at all the nodes and  $\Delta x$  is the grid spacing; the constant  $C$  is typically taken as 0.5.

For the validity of the local approximations for momentum and energy, it is necessary that one - two points be located within the respective boundary layers. The relative thickness of these boundary layers depends on the Prandtl number. In our experience, the use of  $a/\Delta x$  about 10 is adequate for the momentum boundary layer up to Reynolds number of order 100. The analogous quantity for the energy equation is the Peclét number. When  $Pr > 1$ , the thermal boundary layer is thinner than the momentum boundary layer and the choice of  $\Delta x$  should be based on the  $Pe$  rather than  $Re$ .

The scalar products in (4.13) are effected by the same Lebedev quadrature method used e.g. for equation (2.9) and described in Sierakowski, 2016 and Sierakowski and Prosperetti, 2016. The temperature at the quadrature nodes is obtained by linear interpolation from the surrounding nodes. The summation in (4.9) is truncated at a maximum value  $\ell_{max}$ , which results in  $(2\ell_{max} + 1)^2$  coefficients  $T_{\ell m}$ .

The calculation proceeds according to the following steps:

1. First the velocity and pressure field are updated using the previous-time temperature according to the procedure described in section 2.2; the particle position is also updated;
2. For simplicity, as in Balachandar and Ha (2001), the particle temperature is updated by a first-order Euler discretization of equation (4.4):

$$T_p^{n+1} = T_p^n - \frac{1}{\tau s_p} \oint_{s_p} \nabla T^n \cdot \mathbf{n}_p ds_p = T_p^n - \frac{\Delta t}{\tau \sqrt{4\pi}} T_{00}^n, \quad (4.23)$$

with superscripts indicating the time level;

3. Eq. (4.9) with the updated  $T_p^{n+1}$  and the previous-time values of the coefficients  $T_{\ell m}$  is used to assign the temperature at the cage nodes (which are the same as the cage nodes for the pressure field);
4. The energy equation is solved with these boundary conditions and appropriate boundary conditions on the outer surface of the computational domain; the updated velocity field of step 1 is used in the energy equation;
5. From the temperature solution thus obtained a new set of coefficients  $T_{\ell m}$  is found by taking the appropriate scalar products (4.13), the temperature at the cage nodes is updated and the procedure, starting with step 3, is repeated to convergence of the  $T_{\ell m}$ .

When two particles get very close, it may happen that one or a few of the integration points for the Lebedev quadrature for one particle fall in the other

particle. To account for this possibility, the temperature at all nodes internal to a particle is defined to be the particle temperature. In principle, when two particles are very close, one may also need the analog of the lubrication force used for the momentum equation. This is a subtle problem that we leave for future work. This feature of the present method limits its applicability to situations in which particle contacts are short. Thus, for example, it would not be very accurate for a stationary particle bed or for particles resting on a surface for a long time.

## 4.5 Verification

We describe here the results of several tests of the accuracy of our method and of its implementation. Some examples are based on exact analytic solutions and others on the exact integral balance relations derived in the Appendix [4.A](#).

### 4.5.1 Stationary particle in a quiescent fluid

The simplest case is that of a single stationary particle in a quiescent fluid. We begin by considering an overall energy balance between the particle and the outer surface  $S_f$  of the computational domain. In steady conditions,  $Q_p$ , the heat flow out of the particle defined in equation (4.11), should equal the total heat flowing out of the computational domain (see Eq. (4.41) in the Appendix [4.A](#)) so that the ratio defined by

$$\Lambda_T = -\frac{1}{Q_p} \oint_{S_f} k \nabla T \cdot \mathbf{n} dS_f, \quad (4.24)$$

$r_T/a$	$\ell_{max}$	$\Lambda_T$
1.15	2, 3	1.00393
1.15	4	1.00229
1.2	2, 3	1.00345
1.2	4	1.00226
1.25	2, 3	0.99399
1.25	4	0.99329

**Table 4.1:** The deviation from 1 of the quantity  $\Lambda_T$ , defined in (4.24), is a measure of the error affecting the solution of the energy equation. The results in this table illustrate the sensitivity of the numerical error to the choice of the radius  $r_T/a$  of the integration surface and to different orders of truncation  $\ell_{max}$  of the series expansion (4.9). The situation simulated is a single particle at constant temperature in an enclosure subject to a constant heat flux with no fluid flow.

should equal 1 in the absence of errors. In the situation we consider a uniform heat flux is imposed on one of the outer faces of the computational domain, all the other faces being insulated, and the particle temperature held fixed as might be the case, for example, for a particle undergoing melting or freezing. We first show the results for single particle in table 4.1. The multiple particles results are showed in table 4.2 to indicate the effects on volume fraction.

Table 4.1 shows the computed values of  $\Lambda_T$  for different truncation orders  $\ell_{max}$  of the infinite sum (4.9) and different radii  $r_T/a$  of the integration surface for the scalar products (4.13). Here we use eight cells per radius. The volume fraction is 0.065 for all simulations. The error is consistently found to be a fraction of 1% and essentially insensitive to the details of the computation.

In table 4.2, we show the results for different volume fraction and conclude the general rule for choosing the order of expansion and integrate surface. In all the cases, particle surface temperature are different and held fixed. And the boundary conditions are the same as before. For smaller volume fraction,

$N_p$	$r_T/a$	$\ell_{max}$	$a/\Delta x$	$\alpha$	$D_c/a$	$D_{left}/a$	$D_{top}/a$	$\Lambda_T$
2	1.15	2	8	0.177	0.5	0.375	0.5	1.02010
2	1.15	4	8	0.177	0.5	0.375	0.5	1.01029
2	1.15	4	8	0.282	0.25	0.25	0.25	0.96598
2	1.15	4	16	0.282	0.25	0.25	0.25	1.00409
2	1.08	4	16	0.368	0.25	0.125	0.125	0.98457
2	1.04	4	32	0.368	0.25	0.125	0.125	0.99741
10	1.15	4	8	0.25	–	random	–	1.0083
10	1.15	4	16	0.25	–	random	–	1.0020
10	1.08	4	16	0.25	–	random	–	1.0017
27	1.08	4	16	0.368	0.25	0.125	0.125	1.0089
27	1.04	4	16	0.368	0.25	0.125	0.125	1.0288

**Table 4.2:** The deviation from 1 of the quantity  $\Lambda_T$ , defined in (4.24).  $N_p$  is the number of particles;  $a/\Delta x$  is the grid resolution, where  $a$  is the particle radius;  $\alpha$  is the volume fraction;  $D_c$  is the distance between two particle centers;  $D_{left}$  is the distance from the most left particle center to the left boundary;  $D_{top}$  is the distance between the most upper particle center the the top boundary.

a small grid resolution and lower order can provide a reasonable accurate results, though a higher order may increase the accuracy. When volume fraction is higher, only increasing the order of expansion is not enough to resolve the field and increasing the grid resolution is required to improve the accuracy. To get more accurate results, increasing the grid resolution as well as choosing a more reasonable integrate surface  $r_T/a$  can provide a better solution. By author's experience, the choice of  $r_T/a$  should be chosen based on grid resolution, typically it is chosen between the value  $1 + \Delta x/a \sim 1 + 2\Delta x/a$ .

Next we consider three situations chosen so as to investigate the error incurred with the simple quasi-steady approximation (4.9) and the effectiveness of the correction (4.15). We compare the computed results with the analytic solution corresponding to a fluid at the reference temperature far from the

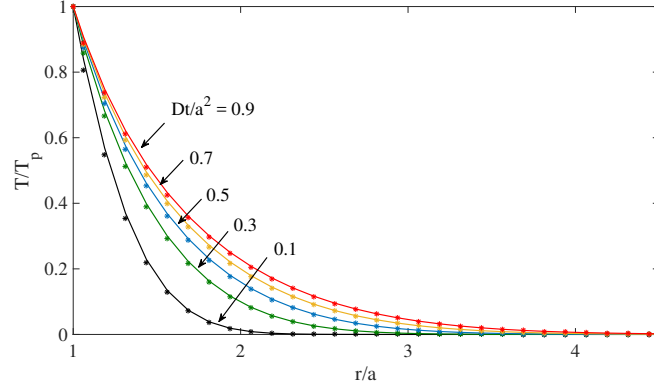


**Figure 4.1:** Temperature distribution in the neighborhood of a particle instantaneously brought to the temperature  $T_p$  higher than that of the surrounding medium which is at the reference temperature. The lines (in ascending order with increasing time) are the analytic solution (4.25) and the symbols the computed results.

particle. The computational domain is a cube of side  $16a$  with the particle centered at its center. On the cube surfaces the reference temperature is imposed since, up to the maximum times considered here, they are far enough from the particle that the difference with the analytic solution is negligible. In these simulations we use  $a/\Delta x = 8$ ,  $r_T/a = 1.15$  and  $\ell_{max} = 3$ .

In the first case the fluid is initially at the reference temperature while the particle temperature takes on the value  $T_p$  at  $t = 0+$ . The analytic solution for the fluid temperature is

$$\frac{T(r, t)}{T_p} = \frac{a}{r} \operatorname{erfc} \left( \frac{r - a}{2\sqrt{Dt}} \right), \quad (4.25)$$

and the corresponding Nusselt number at the particle surface defined in (4.10) is

$$Nu_p = \frac{Q_p}{2\pi a k T_p} = 2 + \frac{2a}{\sqrt{\pi Dt}}, \quad (4.26)$$

with  $Q_p$  as in (4.11).



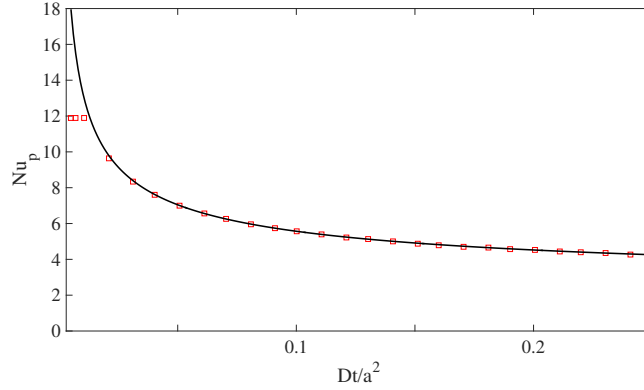


**Figure 4.2:** Early-time behavior of the particle Nusselt number for the situation of the previous figure. The line is the exact solution (4.26) and the symbols the numerical results.

In the second example the particle temperature is a linearly increasing function of time,  $T_p = t$ . The analytic solution for the fluid temperature is readily found by means of the Laplace transform and is

$$T(r, t) = \left( t + \frac{(r-a)^2}{2D} \right) \frac{a}{r} \operatorname{erfc} \left( \frac{r-a}{2\sqrt{Dt}} \right) - \frac{a(r-a)}{r} \sqrt{\frac{t}{\pi D}} \exp \left( -\frac{(r-a)^2}{4Dt} \right). \quad (4.27)$$

For the third example the particle temperature is a sinusoidal function of time oscillating with an angular frequency  $\omega$  and an amplitude  $T_A$ . When steady conditions have been reached, the analytic solution for the fluid temperature is the real part of

$$T(r, t) = \frac{a}{r} \exp \left( i\omega t - \sqrt{\frac{i\omega}{D}}(r-a) \right) T_A. \quad (4.28)$$

Figures 4.1 and 4.2 refer to the first example. The first figure shows a comparison of the computed temperature field (symbols) superimposed on the analytic solution (4.25) (continuous lines) at various instants of time. One

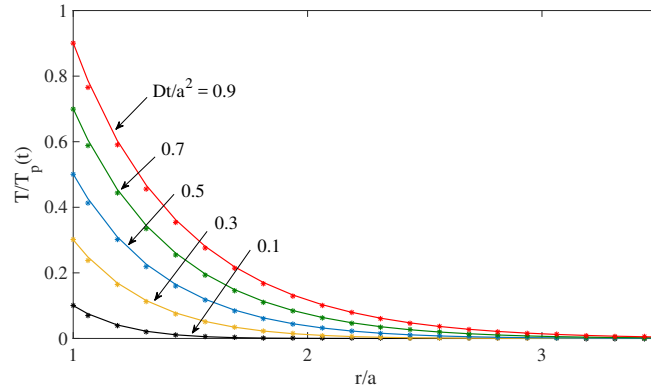
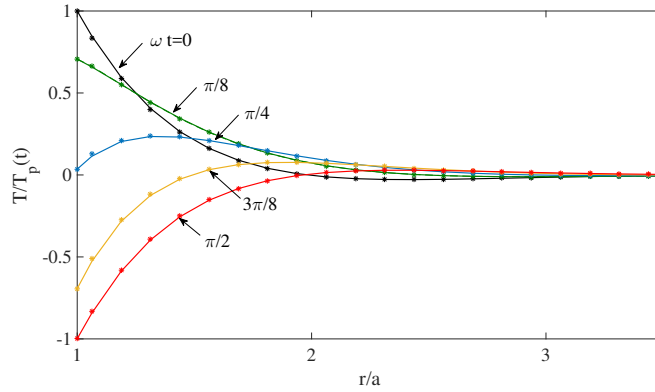


**Figure 4.3:** Temperature distribution in the neighborhood of a particle the temperature of which increases linearly with time. Initially both the particle and the medium surrounding it are at the reference temperature. The lines (in ascending order with increasing time) are the analytic solution (4.27) and the symbols the computed results.

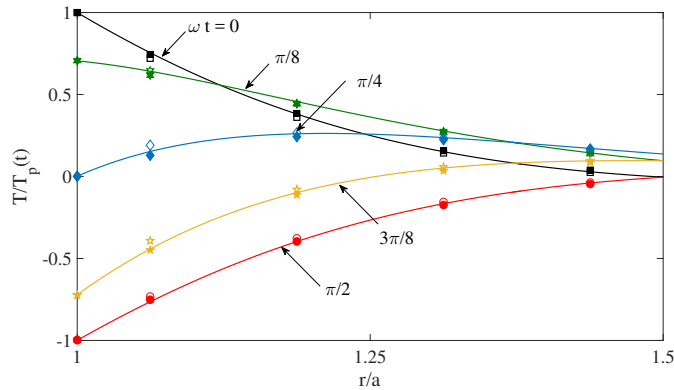
observes an excellent agreement at the times shown. At very early times, however, one expects some error which, indeed, is evident in figure 4.2. Here the particle Nusselt number is shown as a function of time with a focus on the early times. In this extreme case in which the time scale for the temperature variation of the particle is as short as possible – in fact, zero – the error is not small, but it very quickly decreases. The dimensionless time for the propagation of temperature information over a distance comparable to a mesh length away from the particle surface is of the order of  $Dt/a^2 = (\Delta x/a)^2$  which, with  $a/\Delta x = 8$  as used here, is about 0.0156. The figure shows that, after a time of this order, the error has indeed become negligible.

Figure 4.3 refers to the second example, with a linearly increasing particle temperature. Here the temperature change is gradual and the numerical and analytical solutions are always very close.

The third example, oscillating particle temperature, offers us the possibility



**Figure 4.4:** Steady-state temperature distribution in the medium surrounding a particle the temperature of which oscillates in time with a frequency  $\omega$  at different instants of time. The Péclet number is  $\omega a^2/D = 5$ . The lines are the exact solution (4.28) and the symbols the computational results.



**Figure 4.5:** Steady-state temperature distribution in the medium surrounding a particle the temperature of which oscillates in time with a frequency  $\omega$  at different instants of time. The Péclet number is  $\omega a^2/D = 20$ . The lines are the exact solution (4.28), the open symbols the computational results found using (4.9) for the temperature at the temperature cage nodes, and the filled symbols the computational results found by adding the correction (4.15) to the temperature at the cage nodes.

of modulating between a very short time scale (large  $\omega$ ) and a long one. Figure 4.4 shows the results for a case with a dimensionless frequency, or Péclet number  $Pe = \omega a^2/D = 5$ . Agreement between the analytical and computational results (lines and asterisks, respectively) is essentially perfect. If the dimensionless frequency is increased to  $Pe = 20$  as in figure 4.5, however, one notices some errors of the quasi-steady approximation (open symbols). The filled symbols show the results after the application of the correction  $T_1$  given in (4.15). The difference is small, but it somewhat improves the agreement. Figure 4.6 is a graph of the error of the numerical solution with respect to the analytical one as a function of the Péclet number. The error  $\epsilon$  shown here is defined as

$$\epsilon = \frac{1}{T_A} \sqrt{\sum_{i=1}^{N_{pnts}} \langle [T_{num}(\mathbf{x}_i, t) - T_{ex}(\mathbf{x}_i, t)]^2 \rangle}, \quad (4.29)$$

where the  $N_{pnts} = 56$  points  $\mathbf{x}_i$  are taken along a line through the sphere center and perpendicular to one of the sides of the enclosure and the angle brackets indicate the average over one cycle of oscillation. The solid line is the error of the corrected and the dashed line that of the uncorrected numerical result. It can be seen that the correction is beneficial up to  $Pe \sim 50$ , but becomes detrimental for larger values of  $Pe$ . This feature is due to the fact that, at frequencies of this order, the phase of the temperature oscillation reverses during the diffusion time over a distance of the order of the mesh length  $(\Delta x)^2/D$ . Indeed  $\omega(\Delta x)^2/D \sim 1$  is equivalent to  $Pe \sim (a/\Delta x)^2$  which, with the present parameter values, is  $Pe \sim 64$ .

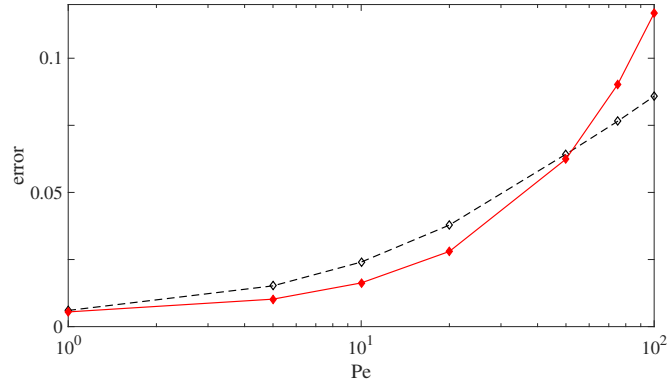


**Figure 4.6:** Cumulative error, defined in (4.29) of the corrected (solid line) and uncorrected numerical result for a particle the surface temperature of which oscillates sinusoidally. The horizontal axis is the Péclet number  $Pe = \omega a^2 / D$ .

### 4.5.2 Stationary particles in a moving fluid

We now turn to the steady flow past a fixed sphere at a Reynolds number  $Re = 2aU/\nu = 50$ ;  $U$  is the incident velocity. The momentum aspects of the PHYSALIS method have been extensively validated in: see e.g., Gudmundsson and Prosperetti, 2013; Sierakowski and Prosperetti, 2016 and we do not dwell on them. We simply note that we have repeated some of the earlier tests, and particularly those with flow past a periodic array of spheres for which exact balance relations are available, with similar results.

Some computed results for the drag coefficient for a single sphere in steady uniform flow are shown in Table 4.3 for different orders of truncation and cells per radius. The computed values are seen to vary little with the parameters of the calculation. An exception is the last entry, for a coarser discretization with  $a/\Delta x = 6$ , which gives a somewhat larger drag coefficient than the others.

To gain some perspective on these results we show in Table 4.4 a collection

$r_s/a$	$\ell_{max}$	$a/\Delta x$	domain size	$C_D$	$Nu_p$	$\Lambda_q$
1.2	3	8	$20a \times 20a \times 40a$	1.6272	5.4119	1.0078
1.2	3	8	$20a \times 20a \times 40a$	1.6274	5.4123	1.0078
1.25	3	8	$20a \times 20a \times 40a$	1.6381	5.4111	1.0079
1.15	3	8	$20a \times 20a \times 40a$	1.6288	5.4130	1.0078
1.2	2	8	$20a \times 20a \times 40a$	1.6266	5.4115	1.0080
1.2	3	10	$16a \times 16a \times 32a$	1.6526	5.4548	1.0034
1.2	3	6	$20a \times 20a \times 40a$	1.6540	5.3193	1.0226

**Table 4.3:** Calculated drag coefficient  $C_D$  and particle Nusselt number  $Nu_p$  for steady uniform flow past a single spherical particle at  $Re = 50$  for various values of the radius  $r_s$  of the momentum integration surface, order of truncation  $\ell_{max}$  of the infinite summations, mesh lengths per radius  $a/\Delta x$  and domain size. The deviation from 1 of the quantity  $\Lambda_q$ , defined in (4.30), is a measure of the numerical error affecting the solution of the energy equation. For all these simulations, the radius of the integration surface for the temperature is  $r_T/a = 1.15$  and the order of truncation in (4.9)  $\ell_{max} = 3$ .

of results from the literature. With a few exceptions, the reported values are somewhat lower than our computed values but they all agree within a few percent.

The next-to-last column of Table 4.3 shows the computed results for the single-particle Nusselt number  $Nu_p$  with the various parameter values used for the velocity calculation. To generate these results, in solving the energy equation we used  $a/\Delta x = 8$ ,  $r_T/a = 1.15$  and  $\ell_{max} = 3$ ; the fluid enters the domain at the reference temperature and homogeneous Neumann conditions are imposed to the temperature field on the rest of the boundary.

By the methods demonstrated in the Appendix 4.A it is easy to show that, for flow over one or more heated bodies, at steady conditions the overall energy balance over the computational domain requires that the quantity

$$\Lambda_q = \frac{\rho c_p}{\sum_{\alpha=1}^{N_p} Q_p} \oint_{S_f} T \mathbf{u} \cdot \mathbf{n} dS_f, \quad (4.30)$$

	type	$C_D(Re = 50)$	$Nu_p(Re = 50)$
Xia, Luo, and Fan, 2014	S	1.53	5.33
Richter and Nikrityuk, 2012	S	1.577	5.49
Schlichting and Gersten, 2003		1.61	–
Bagchi, Ha, and Balachandar, 2001	S	1.57	5.4
Mittal, 1999	S	1.57	–
Tabata and Itakura, 1998	S	1.579	–
Haider and Levenspiel, 1989	C	1.633	–
Clift, Grace, and Weber, 1978	C	1.57	–
Whitaker, 1972	C	–	5.19
Feng and Michaelides, 2000	C	–	5.51
Ranz and Marshall, 1952	C	–	5.81
Roos and Willmarth, 1971	E	1.60	–

**Table 4.4:** Drag coefficient  $C_D$  and particle Nusselt number  $Nu_p$  for steady uniform flow past a single spherical particle at  $Re = 50$  from the literature. The data in the first group are from numerical simulations (label “S”), those in the second one from empirical correlations (label “C”); the last line is an experimental value (label “E”).

equal 1; the summation is over all the particles in the domain. The values of  $\Lambda_q$  for the single-particle case are shown in the last column of Table 4.3. The result closest to 1 is found with the finest discretization  $a/\Delta x = 10$ , but all the Nusselt numbers calculated with  $a/\Delta x = 8$  differ by less than 1% from this value. The error with the coarser discretization  $a/\Delta x = 6$  is somewhat larger, about 2%.

Figure 4.7 compares the local Nusselt number over the particle surface, defined by,

$$Nu_{loc} = -\frac{2a}{T_p} \nabla T \cdot \mathbf{n}_p, \quad (4.31)$$

with the values reported by Bagchi, Ha, and Balachandar (2001). There is a very good agreement over the entire surface of the sphere, except near the front stagnation point where one observes a difference of 4.5%. This prediction

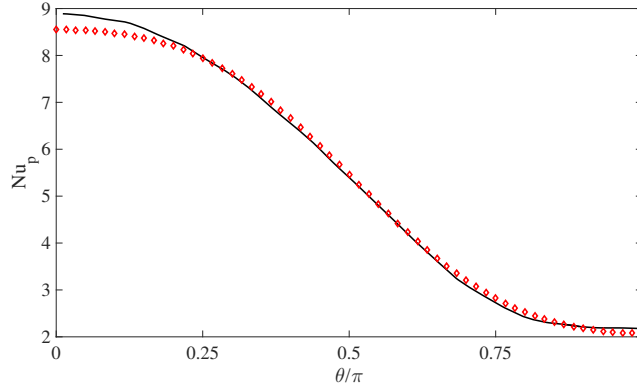


**Figure 4.7:** The local Nusselt number, or dimensionless heat flux, defined in (4.31), at the surface of a sphere immersed in a steady uniform flow at a Reynolds number 50 as a function of the azimuthal angle. The solid line is the result of Bagchi, Ha, and Balachandar (2001) and the points the present results.

is robust with respect to variations of the parameters of our calculation; we may note that a very similar difference is reported by Xia, Luo, and Fan (2014). This result has been obtained with  $r_s/a = 1.2$ ,  $r_T/a = 1.15$ ,  $a/\Delta x = 8$  and  $\ell_{max} = 3$  for both the momentum and the energy calculation.

We also carried out a test with 10 equal particles simultaneously present in the domain, subjected to the same incident flow with  $Re = 50$ , having different temperatures randomly assigned between 80% and 120% of a mean temperature equal to 1; the temperature of the incoming flow is 0. In this test we used again  $a/\Delta x = 8$  and for the parameter defined in (4.30) found the value  $\Lambda_q = 1.003$ . Figure 4.8 shows two views of the temperature iso-surfaces corresponding to a temperature of 0.2; the color shows the temperature distribution on two orthogonal planes.



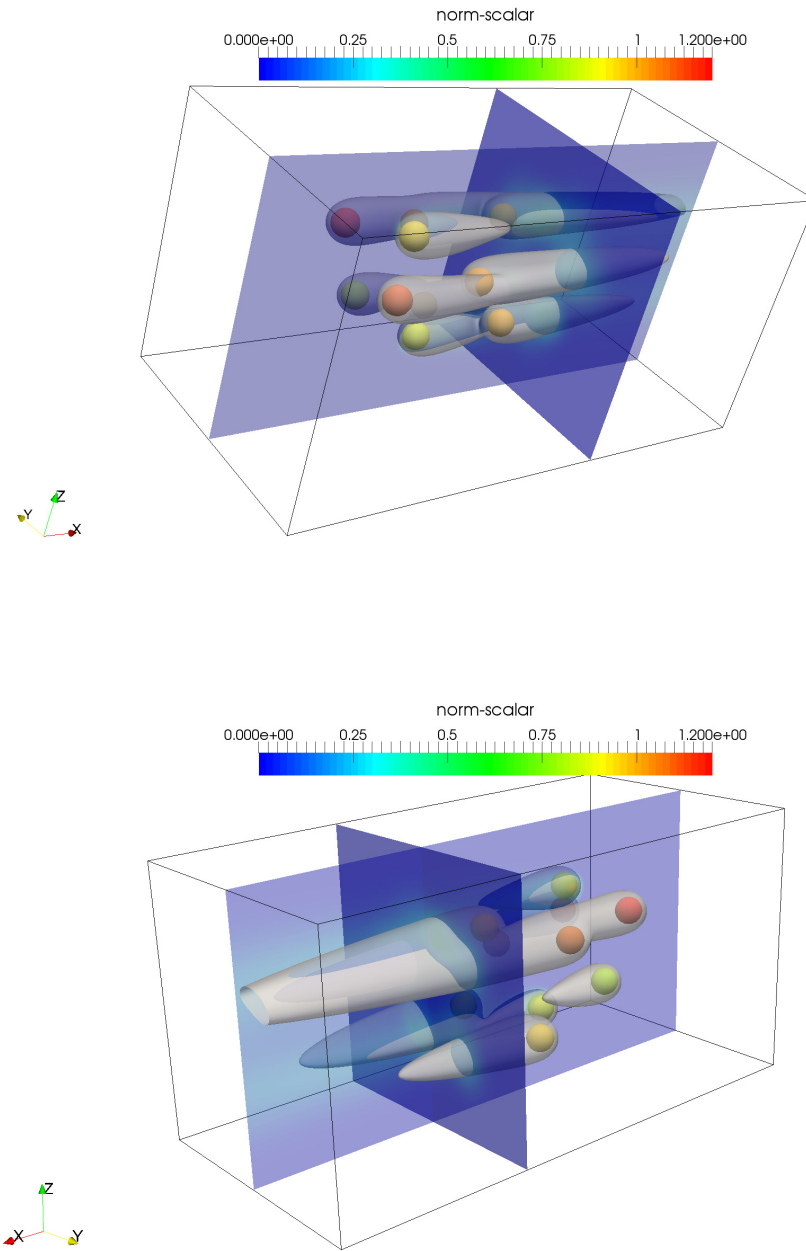


**Figure 4.8:** Two views of the steady temperature distribution and thermal wakes produced by 10 randomly arranged particles immersed in a cold stream; the color indicates the temperature. The particle temperature is fixed and is randomly assigned between 80% and 120% of the mean value 1 and the temperature of the incoming fluid is 0.

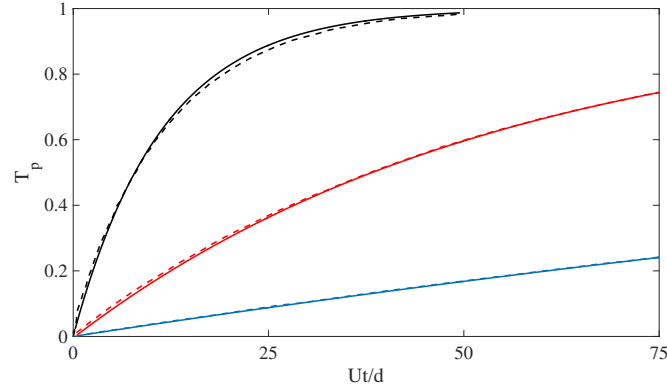


**Figure 4.9:** Time-dependence of the temperature of a particle immersed in a warmer uniform flow with  $Re = 50$ . The solid lines are the present results and the dashed lines the results of Balachandar and Ha (2001). The three sets of curves correspond, in ascending order, to different values of the ratio  $\rho c_p / (\rho_p c_{pp}) = 0.004, 0.02$  and  $0.1$ .

### 4.5.3 Transient heating of a sphere in a flow

For our last example we consider the transient heating of a particle exposed to a warmer incident flow with  $Re = 50$ . The simulation set-up is the same as in the previous steady example. All the temperature boundary conditions on the boundary of the computational domain are homogeneous-Neumann except for the inlet plane, where the temperature is held fixed at a value above the reference temperature; the initial particle temperature is the reference temperature. We waited for steady, fully developed flow conditions to be established before allowing the particle temperature to vary according to (4.4); this instant is chosen as  $t = 0$ . The results for three values of the ratio  $\rho c_p / (\rho_p c_{pp}) = 0.004, 0.02$  and  $0.1$  are shown in ascending order by the solid lines in figure 4.9, where they are compared with the results of Balachandar and Ha (2001) (dashed lines). The corresponding values of the parameter  $U\tau_p/a$ , with  $\tau_p$  the particle time constant defined in (4.5), are 1458.3, 291.68

and 58.333. Here we used  $\ell_{max} = 3$  for both the momentum and energy expansions,  $r_s/a = 1.2$  for the momentum equation and  $r_T/a = 1.15$  for the energy equation. The agreement between the two sets of results is excellent (with a maximum difference about 1.1%).

	$Ra$	$Pr$	$N_x \times N_y \times N_z$	$Nu$	$Nu_h/Nu_c$	$\Lambda_u$	$\Lambda_\theta$
Present	$2 \times 10^5$	1.75	$50 \times 50 \times 100$	5.163	1.000	0.955	0.996
Present	$2 \times 10^5$	1.75	$65 \times 65 \times 130$	5.162	1.000	0.972	0.998
Present	$2 \times 10^6$	0.7	$65 \times 65 \times 130$	11.510	0.998	0.903	0.979
Present	$2 \times 10^6$	0.7	$75 \times 75 \times 150$	11.485	0.999	0.924	0.985
Present	$2 \times 10^6$	0.7	$100 \times 100 \times 200$	11.216	0.998	0.955	0.993
Present	$2 \times 10^6$	0.7	$110 \times 110 \times 220$	11.556	1.005	0.961	0.994
Ref.	$2 \times 10^6$	0.7	$97 \times 49 \times 129$	10.32	-	0.973	0.978
Ref.	$2 \times 10^6$	0.7	$193 \times 97 \times 257$	11.03	-	0.974	0.991

**Table 4.5:** Overall energy balance for single-phase natural convection for two values of the Rayleigh number  $Ra$  and Prandtl number  $Pr$  and different domain discretizations. The convection cell is a parallelepiped with a square cross section and aspect ratio (side/height) = 1/2;  $N_x$ ,  $N_y$  and  $N_z$  are the number of grid points in the two horizontal and the vertical directions; the Nusselt number shown is  $Nu = \frac{1}{2}(Nu_c + Nu_h)$ . The quantities in the last three columns should all be equal to 1 in the absence of errors;  $\Lambda_u$  is the ratio of the computed kinetic energy dissipation rate to the theoretical result given in (4.56);  $\Lambda_\theta$  is the ratio of the temperature dissipation rate to the theoretical result given in (4.52). Ref. represents the work by Stevens, Verzicco, and Lohse (2010). Note that in the work of Stevens, Verzicco, and Lohse (2010), the convection cell is a cylinder rather than a parallelepiped and the numbers of cells quoted are in the azimuthal, radial and axial directions.

## 4.6 Examples with natural convection

In closing we consider a few examples with natural convection, beginning with a single-phase example. The simulation domain is a parallelepiped with a square cross section with an aspect ratio (side/height) equal to  $\frac{1}{2}$ . The bottom surface is heated to a temperature  $T_h$  and the top one is cooled to a

temperature  $T_c$ . For the Rayleigh number, defined by

$$Ra = \frac{g\beta(T_h - T_c)L_z^3}{\nu D}, \quad (4.32)$$

we consider two values,  $Ra = 2 \times 10^5$  and  $Ra = 2 \times 10^6$ ;  $L_z$  is the height of the domain. In the first case the flow field is steady while, in the second one, the flow is slightly turbulent; in this latter case the results reported are time-average values obtained after stationary conditions have been reached. Table 4.5 shows the simulation parameters and the overall balances for the heat flux, kinetic energy dissipation and temperature dissipation; the latter two quantities are defined, respectively, by

$$\Lambda_u = \frac{\langle \Phi \rangle / \rho}{\epsilon_u} \quad \text{and} \quad \Lambda_\theta = \frac{D \langle |\nabla T|^2 \rangle}{\epsilon_\theta}, \quad (4.33)$$

with  $\Phi = \rho\nu \sum_{i,j=1}^3 (\partial u_i / \partial x_j)(\partial u_i / \partial x_j)$  the dissipation function; the angle brackets denote volume and time averages. The quantities  $\epsilon_u$  and  $\epsilon_\theta$  are defined by the numerators of these fractions and, as proven in the Appendix, they can be related to the Nusselt numbers and other quantities of the flow as shown in (4.56) and (4.52). Thus, both  $\Lambda_u$  and  $\Lambda_\theta$  should equal 1 in the absence of errors. It is noticed in Table 4.5 that, when the number of nodes increases, a better performance for the overall balances is obtained with errors approaching 1% or less.

In the second example, we introduce 1, 5 or 8 particles into the same domain; the Rayleigh number defined in the same way as shown in (4.32) is  $2 \times 10^5$  and  $Pr = 1.75$ . For the one-particle cases the particle temperature is fixed above or below the reference temperature taken as  $T_{ref} = \frac{1}{2}(T_h + T_c) =$

0. In the other two cases the particles are randomly distributed and the particle temperature is also fixed and randomly assigned in the range shown in Table 4.6;  $\Lambda_u$  and  $\Lambda_\theta$  are as defined before, while the quantity  $\Lambda_{Nu}$  is defined as

$$\Lambda_{Nu} \equiv \frac{kS_f(T_h - T_c)}{L_z} \frac{Nu_c - Nu_h}{\sum_{\alpha=1}^{N_p} Q^\alpha}, \quad (4.34)$$

and should equal 1 in the absence of errors (see Appendix 4.A). Here  $Nu_c$  and  $Nu_h$  are the Nusselt numbers at the cold and hot bases of the computational cell defined by

$$Nu_{h,c} = -\frac{L_z}{T_h - T_c} \left\langle \frac{\partial T}{\partial z} \right\rangle \Big|_{z=0, L_z}, \quad (4.35)$$

in which angle brackets denote averages over the bases of the cell (and also over time for  $Ra = 2 \times 10^6$ ). These results were obtained by using  $r_s/a = 1.2$ ,  $r_T/a = 1.15$  and  $\ell_{max} = 3$  for both the momentum and temperature expansions. In all cases  $\Lambda_{Nu}$  and  $\Lambda_\theta$  deviate from the exact value 1 by much less than 1%. The deviation of  $\Lambda_u$  from 1 is somewhat greater, probably because of the error affecting the calculation of the velocity derivatives. In any case, this error is always less than 5% and is seen to decrease as the number of nodes is increased.

It should be noted that the parameter  $\Lambda$  defined above include volume averaged quantities, and are therefore sensitive to the particle volume fraction. For the three examples in table 4.6, the particle volume fractions were 0.71%, 1.0%, 1.7% for 1, 5, 8 particles respectively. These volume fractions are small, and they could mask the numerical error. However, at least for the largest volume fraction, a significant error may be expected to become evident. A comparison of table 4.5 and 4.6 does not show a significant increase in the

error.

In the last example, we allow 8 particles to translate and rotate freely for a case with parameters chosen so that  $Ra = 2 \times 10^5$  and  $Pr = 1.75$  as for the fixed-particles cases. The particles adjust their temperature according to (4.4). The values of the other parameters are  $\rho_p/\rho = 70$  and  $\rho c_p/(\rho_p c_{pp}) = 0.1$ ; the calculation was carried out with  $a/\Delta x = 8$ ,  $r_s/a = 1.2$ ,  $r_T/a = 1.15$  and  $\ell_{max} = 3$  for both the momentum and energy expansions. Figure 4.10, where color indicates the temperature, shows three snapshots of the system. One notices the motion of the particles as they are carried around the cell by the circulating natural convection flow and their varying temperature.

It follows from (4.51) in the Appendix that the quantity defined by the generalization of (4.34) to the unsteady case:

$$\Lambda_\theta = \frac{D\langle |\nabla T|^2 \rangle}{\epsilon_\theta + \frac{d}{dt} \int_{V_f} \frac{1}{2} \theta^2 dV_f}, \quad (4.36)$$

with  $\theta = T - \frac{1}{2}(T_h + T_c)$ , should equal 1. We find that this balance differs from 1 by about 5% for the duration of the simulation, although we observe fairly strong deviations when particles get close to the hot or cold cell bases. This is due to the fairly coarse procedure that we have adopted for simplicity to estimate the temperature gradient at the cell bases for use in the definitions (4.35) (of course, the temperature gradients at the particles surface are calculated from the expansion (4.12) as stated previously).

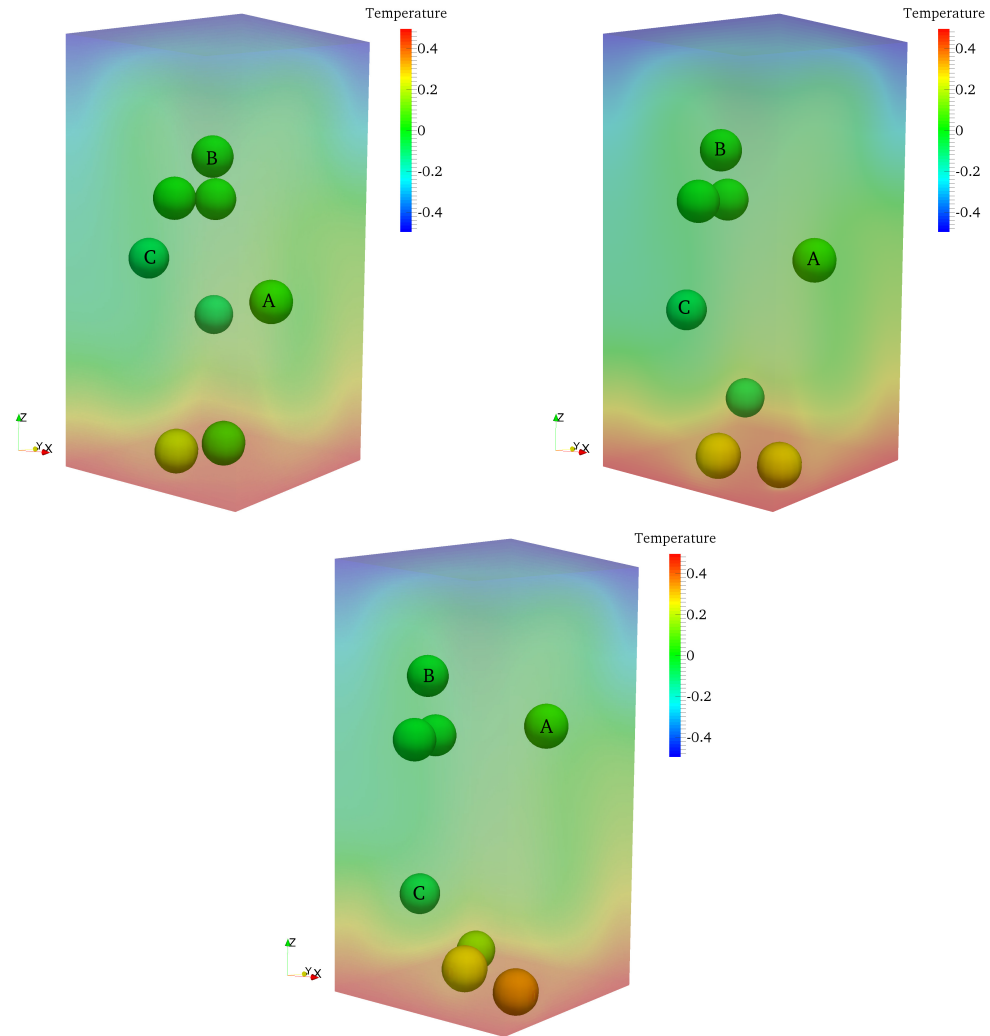


**Figure 4.10:** Successive configurations of an eight-particle system in naturally convecting flow with  $Ra = 2 \times 10^5$  and  $Pr = 1.75$ ; the color indicates the temperature normalized by  $T_h - T_c$ , which ranges from -0.5 at the bottom to 0.5 at the top of the cell. The frames are separated by a dimensionless time interval  $\sqrt{g\beta(T_h - T_c)L_z} \Delta t / L_z \simeq 2.07$ . The particle temperature adjusts according to (4.4);  $\rho c_p / (\rho_p c_{pp}) = 0.1$ . Note the response of the particles to the recirculating motion established by the natural convection in the cell as well as their changing temperature.

$Nu_c$	$Nu_h$	$N_p$	$L_z/a$	$T_p/(T_h - T_c)$	$N_x \times N_y \times N_z$	$\Lambda_{Nu}$	$\Lambda_u$	$\Lambda_\theta$
5.745	4.534	1	13.3	0.2	$50 \times 50 \times 100$	1.0016	0.9564	0.9937
4.881	5.506	1	13.3	-0.1	$50 \times 50 \times 100$	0.9934	0.9558	0.9951
3.309	5.844	5	20.0	$-0.5 \sim 0$	$80 \times 80 \times 160$	0.9985	0.9749	0.9906
4.797	4.567	8	20.0	$-0.35 \sim 0.35$	$80 \times 80 \times 160$	0.9962	0.9826	0.9847

**Table 4.6:** Natural convection with  $N_p$  fixed particles and  $Ra = 2 \times 10^5$ ,  $Pr = 1.75$ . The convection cell is a parallelepiped with a square cross section and aspect ratio (side/height) = 1/2;  $N_x$ ,  $N_y$  and  $N_z$  are the number of grid points in the two horizontal and the vertical directions. The quantities in the last three columns should all be equal to 1 in the absence of errors;  $\Lambda_{Nu}$  is the normalized heat-flux balance given in (4.34);  $\Lambda_u$  is the ratio of the computed kinetic energy dissipation rate to the theoretical result given in (4.56);  $\Lambda_\theta$  is the ratio of the temperature dissipation rate to the theoretical result given in (4.52). In the multi-particle cases, the particle position is randomly assigned and the particle temperature randomly fixed in the range shown. The volume fraction for  $N_p = 1$  is 0.71%, for  $N_p = 5$  is 1.0% and for  $N_p = 8$  is 1.7%.

## 4.7 Summary and Conclusion

We have extended to the energy equation the basic idea underlying the PHYSALIS algorithm, namely the use of local solutions as bridges between the particle surface and the fixed grid. This has permitted us to carry out fully-resolved simulations of moving particles exchanging energy, as well as momentum, with the surrounding fluid. We have demonstrated the method for several situations for which the use of integral balances gives exact results. In this way we were led to the conclusion that the numerical errors of our procedure do not exceed a few percent at most and decrease as the grid is refined. For many quantities, the errors were much less than 1%. Just as in the isothermal case considered in earlier papers, the method gives accurate results even with the use of a fairly coarse discretization. Important quantities, such as the particle Nusselt number, do not require separate calculations but are



found directly in the course of the solution procedure, almost as a by-product of the algorithm.

We considered a fluid with constant properties, but treated also examples with natural convection in the Boussinesq approximation. For the particles we assumed a lumped-capacitance model, and we have pointed out how more general thermal properties can be handled in a similar way.

Our implementation was second-order accurate in space but, due to the use of explicit time stepping, only first-order accurate in time. More accurate implementations are also possible.

Mathematically, the energy equation is parabolic just as other important equations, such as the one governing mass diffusion. Thus, the same method can be used for dissolving or accreting particles, as long as they can be assumed to remain spherical. In the case of dissolution, however, it may be necessary to use a very fine grid to accurately follow the decreasing size of the particle. Another situation that can be addressed in the same way is, for example, the absorption of an organic pollutant dissolved in water by activated carbon particles. Our experience with the momentum equation suggests that it may be equally possible to treat problems governed by non-linear parabolic equations.

# Appendices

## 4.A Integral balances

We give here a derivation of the integral balances used in the validation of the method in sections 4.5 and 4.6. These relations are well-known in the theory of single-phase Rayleigh-Bénard convection (see e.g. Ahlers, Grossmann, and Lohse, 2009), but the presence of particles modifies them so that it is worth while to present a specific derivation for this case.

We consider a computational domain in the form of a parallelepiped with or without  $N_p$  spherical particles, fixed or mobile, in its interior. The velocity boundary conditions on the surface  $S_f$  of the parallelepiped enforce inflow/outflow, no-slip or periodicity. In the absence of natural convection effects, for temperature we assume a prescribed temperature, periodicity or insulation conditions on  $S_f$ . When natural convection effects are accounted for, no-slip applies over the entire  $S_f$  and insulation conditions apply on the lateral portion of  $S_f$  while the lower and upper bases,  $S_h$  and  $S_c$ , are at constant uniform temperatures  $T_h$  and  $T_c$ , respectively; the  $z$ -axis is taken parallel to the acceleration of gravity and directed upward. The derivation apply specifically to these conditions.

In the derivation we make use of the extended Reynolds's transport theorem for a generic quantity  $\phi$  applicable to a fluid domain the boundary of which is in arbitrary motion:

$$\frac{d}{dt} \int_{V_f} \phi dV_f = \int_{V_f} \frac{\partial \phi}{\partial t} dV_f + \oint_{S_t} \phi \mathbf{v} \cdot \mathbf{n} dS_t. \quad (4.37)$$

Here  $V_f$  is the volume occupied by the fluid and  $S_t$  the total boundary of this volume consisting, in the present application, of the particle surfaces and of the external boundary  $S_f$  of the computational domain. The quantity  $\phi$  satisfies a general balance equation of the form

$$\frac{\partial \phi}{\partial t} + \mathbf{u} \cdot \nabla \phi = \nabla \cdot \mathbf{j} + \Sigma, \quad (4.38)$$

with  $\mathbf{j}$  the flux of  $\phi$  and  $\Sigma$  its volume source. Upon using this equation and the divergence theorem, (4.37) may be written as

$$\frac{d}{dt} \int_{V_f} \phi dV_f = \oint_{S_t} \phi (\mathbf{v} - \mathbf{u}) \cdot \mathbf{n} dS_t + \oint_{S_f} \mathbf{j} \cdot \mathbf{n} dS_t + \int_{V_f} \Sigma dV_f. \quad (4.39)$$

We now specialize this relation to the problem at hand recognizing that, on the particle surfaces,  $(\mathbf{v} - \mathbf{u}) \cdot \mathbf{n} = 0$  while, on the outer surface,  $\mathbf{v} = 0$ . Thus the equation becomes

$$\frac{d}{dt} \int_{V_f} \phi dV_f = \oint_{S_f} (\mathbf{j} - \phi \mathbf{u}) \cdot \mathbf{n} dS_f - \sum_{\alpha=1}^{N_p} \oint_{S_p^\alpha} \mathbf{j} \cdot \mathbf{n}_p^\alpha ds_p^\alpha + \int_{V_f} \Sigma dV_f. \quad (4.40)$$

Here  $\mathbf{n}_p^\alpha$  is the unit normal outwardly directed on the surface  $s_p^\alpha$  of the  $\alpha$ -th particle.

If we apply this relation to the energy equation (4.3) we have

$$\frac{d}{dt} \int_{V_f} T dV_f = - \oint_{S_f} (D\nabla T + T\mathbf{u}) \cdot \mathbf{n} dS_f + \sum_{\alpha=1}^{N_p} \oint_{S_p^\alpha} D\nabla T \cdot \mathbf{n}_p^\alpha dS_p^\alpha. \quad (4.41)$$

With the boundary conditions specified above, the contribution of the convection term to the integral over  $S_f$  vanishes. The contribution of  $\nabla T$  to the integral over the lateral surfaces of  $S_f$  also vanishes so that the first integral in the right-hand side reduces to

$$\oint_{S_f} \nabla T \cdot \mathbf{n} dS_f = \int_{S_h} \nabla T \cdot \mathbf{n}_h dS_h + \int_{S_c} \nabla T \cdot \mathbf{n}_c dS_c. \quad (4.42)$$

We define the Nusselt number on the lower surface as the normalized heat flux into the computational domain:

$$Nu_h = -\frac{L_z}{S_h(T_h - T_c)} \int_{S_h} \nabla T \cdot \mathbf{n}_h dS_h, \quad (4.43)$$

with  $L_z$  the vertical extent of the domain, and on the upper surface as the normalized heat flux out of the computational domain:

$$Nu_c = \frac{L_z}{S_c(T_h - T_c)} \int_{S_c} \nabla T \cdot \mathbf{n}_c dS_c. \quad (4.44)$$

If  $T_h = T_c$ , both Nusselt numbers are defined to vanish. With these definitions, since the surface areas of the lower and upper horizontal surfaces are equal, (4.42) becomes

$$\oint_{S_f} \nabla T \cdot \mathbf{n} dS_f = -\frac{S_h}{L_z}(T_h - T_c)(Nu_c - Nu_h). \quad (4.45)$$

and (4.41) itself reduces to

$$\frac{d}{dt} \int_{V_f} T dV_f = -\frac{DS_h}{L_z} (T_h - T_c) (Nu_c - Nu_h) - \frac{1}{k} \sum_{\alpha=1}^{N_p} Q^\alpha, \quad (4.46)$$

where

$$Q^\alpha = - \oint_{s_p^\alpha} k \nabla T \cdot \mathbf{n}_p^\alpha ds_p^\alpha, \quad (4.47)$$

is the heat flow out of the  $\alpha$ -th particle. In particular, without particles and in steady conditions (4.46) reduces to  $Nu_h = Nu_c$  as expected. In steady conditions and in the presence of particles we deduce from this relation that the quantity  $\Lambda_{Nu}$  defined in (4.34) should equal 1.

Another test that can be based on the steady-state version of (4.41) concerns a single stationary particle at a fixed temperature in an enclosure with walls at a uniform, different fixed temperature in the absence of flow. In this case conservation of energy requires that the ratio

$$\Lambda_T = \frac{\oint_{s_p} \nabla T \cdot \mathbf{n}_p ds_p}{\int_{S_f} \nabla T \cdot \mathbf{n} dS_f}, \quad (4.48)$$

be equal to 1. We have used this result in the first example of section 4.5.

The so-called thermal, or temperature, dissipation is defined as the integral over the fluid volume of  $k|\nabla\theta|^2$  with  $\theta = T - \frac{1}{2}(T_h + T_c)$ . A balance equation for the square of this quantity readily follows from the energy equation and is

$$\frac{\partial}{\partial t} \frac{1}{2} \theta^2 + \mathbf{u} \cdot \nabla \frac{1}{2} \theta^2 = D \left[ \nabla \cdot (\theta \nabla \theta) - |\nabla \theta|^2 \right]. \quad (4.49)$$

In this case, therefore, the general equation (4.40) becomes

$$\frac{d}{dt} \int_{V_f} \frac{1}{2} \theta^2 dV_f + D \oint_{S_f} \theta \nabla \theta \cdot \mathbf{n} dS_f - D \sum_{\alpha=1}^{N_p} \oint_{S_p^\alpha} \theta \nabla \theta \cdot \mathbf{n}_p^\alpha dS_p^\alpha = D \int_{V_f} |\nabla \theta|^2 dV_f. \quad (4.50)$$

In writing this equation the convective term has been omitted since it vanishes with the boundary conditions that we consider. Thus we find

$$D \int_{V_f} |\nabla \theta|^2 dV_f = \frac{d}{dt} \int_{V_f} \frac{1}{2} \theta^2 dV_f + \frac{DS_h(T_h - T_c)^2}{2L_z} (Nu_h + Nu_c) + \frac{D}{k} \sum_{\alpha=1}^{N_p} \theta_p^\alpha Q^\alpha. \quad (4.51)$$

in writing which we have used the fact that  $\theta = \theta_p^\alpha$  is a constant over the surface of the  $\alpha$ -th particle; here  $Nu_h$  and  $Nu_c$  denote instantaneous values. After reaching statistically steady conditions we have

$$\epsilon_\theta = \frac{D(T_h - T_c)^2}{2L_z^2} (Nu_c + Nu_h) + \frac{D}{V_f k} \sum_{\alpha=1}^{N_p} \theta_p^\alpha Q^\alpha, \quad (4.52)$$

in which  $\epsilon_\theta = k \langle |\nabla \theta|^2 \rangle$  is the volume and time average of  $k |\nabla \theta|^2$ .

The final balance relation concerns the integral of the total energy  $\mathcal{E} = \frac{1}{2} \rho u^2 + \rho \beta \mathbf{x} \cdot \mathbf{g} T$  given by the sum of of the kinetic and potential energies. Upon using the momentum and energy equations (4.2) and (4.3) we find

$$\frac{\partial \mathcal{E}}{\partial t} + \mathbf{u} \cdot \nabla \mathcal{E} = \nabla \cdot [\mathbf{u} \cdot \boldsymbol{\sigma} + \rho \beta (\mathbf{x} \cdot \mathbf{g}) \nabla T - T \mathbf{g}] - \Phi, \quad (4.53)$$

in which  $\boldsymbol{\sigma}$  is the total stress and  $\Phi = \rho \nu (\partial u_j / \partial x_i) (\partial u_j / \partial x_i)$  is the dissipation function. The flux  $\mathbf{j}$  and volume source  $\Sigma$  appearing in (4.40) can be read off from this relation and substituted into (4.40). The convective terms vanish by

the boundary conditions and we are left with

$$\begin{aligned} \frac{d}{dt} \int_{V_f} \mathcal{E} dV_f = & \rho\beta D \oint_{S_f} [(\mathbf{x} \cdot \mathbf{g}) \nabla T - T \mathbf{g}] \cdot \mathbf{n} dS_f \\ & - \sum_{\alpha=1}^{N_p} \oint_{s_p^\alpha} [\mathbf{u} \cdot \boldsymbol{\sigma} + \rho\beta D (\mathbf{x} \cdot \mathbf{g}) \nabla T] \cdot \mathbf{n}_p^\alpha ds_p^\alpha - \int_{V_f} \Phi dV_f, \end{aligned} \quad (4.54)$$

where terms that do not contribute have been omitted. The result takes on a slightly simpler form if the origin is taken at the center of the domain so that the  $z$  coordinates of the two bases are  $\pm \frac{1}{2} L_z$ . With this choice we find

$$\begin{aligned} \int_{V_f} \Phi dV_f = & - \frac{d}{dt} \int_{V_f} \mathcal{E} dV_f + \rho\beta D g S_h (T_h - T_c) \left[ \frac{1}{2} (Nu_h + Nu_c) - 1 \right] \\ & - \sum_{\alpha=1}^{N_p} \left[ \mathbf{w}^\alpha \cdot \mathbf{F}^\alpha + \boldsymbol{\Omega}^\alpha \cdot \mathbf{L}^\alpha + \rho\beta D \oint_{s_p^\alpha} (\mathbf{x} \cdot \mathbf{g}) \nabla T \cdot \mathbf{n}_p^\alpha ds_p^\alpha \right], \end{aligned} \quad (4.55)$$

in which  $g = |\mathbf{g}|$  and  $\mathbf{F}^\alpha$  and  $\mathbf{L}^\alpha$  are the hydrodynamic forces and couples on the particles. In statistically steady conditions this result may be written as

$$\begin{aligned} \epsilon_u = & \frac{\nu^3 Ra}{L_z^4 Pr^2} \left[ \frac{1}{2} (Nu_h + Nu_c) - 1 \right] \\ & - \frac{1}{V_f \rho} \sum_{\alpha=1}^{N_p} \left[ \mathbf{w}^\alpha \cdot \mathbf{F}^\alpha + \boldsymbol{\Omega}^\alpha \cdot \mathbf{L}^\alpha + \rho\beta D \oint_{s_p^\alpha} (\mathbf{x} \cdot \mathbf{g}) \nabla T \cdot \mathbf{n}_p^\alpha ds_p^\alpha \right]. \end{aligned} \quad (4.56)$$

In the absence of numerical error, and at true steady state,  $\epsilon_u$  should equal  $\langle \Phi / \rho \rangle$ , the volume and time average of  $\Phi / \rho$ , as calculated from a direct calculation of the dissipation.

## References

- Ahlers, G., S. Grossmann, and D. Lohse (2009). "Heat transfer and large scale dynamics in turbulent Rayleigh-Bénard convection". In: *Revs. Mod. Phys.* 81, pp. 503–537.
- Bagchi, P., M. Y. Ha, and S. Balachandar (2001). "Direct numerical simulation of flow and heat transfer from a sphere in a uniform cross-flow". In: *J. Fluids Eng. Trans. ASME* 123, pp. 347–358.
- Balachandar, S. and M. Y. Ha (2001). "Unsteady heat transfer from a sphere in a uniform cross-flow". In: *Phys. Fluids* 13, p. 3714.
- Clift, R. C., J. R. Grace, and M. E. Weber (1978). *Bubbles, Drops, and Particles*. Academic Press.
- Feng, Z. G. and E. E. Michaelides (2000). "A numerical study on the transient heat transfer from a sphere at high Reynolds and Péclet numbers". In: *Int. J. Heat Mass Transfer* 43, pp. 219–229.
- Gudmundsson, K. and A. Prosperetti (2013). "Improved procedure for the computation of Lamb's coefficients in the PHYSALIS method for particle simulation". In: *J. Comput. Phys.* 234, pp. 44–59.
- Haider, A. and O. Levenspiel (1989). "Drag coefficient and terminal velocity of spherical and nonspherical particles". In: *Powder technol.* 58, pp. 63–70.
- Mittal, R. (1999). "A Fourier-Chebyshev spectral collocation method for simulating flow past spheres and spheroids". In: *Int. J. Numer. Meth. Fluids* 30, pp. 921–937.
- Ranz, W. E. and W. R. Marshall (1952). "Evaporation from Drops, Part II". In: *Chem. Eng. Prog* 48, pp. 173–180.
- Richter, A. and P. Nikrityuk (2012). "Drag forces and heat transfer coefficients for spherical, cuboidal and ellipsoidal particles in cross flow at sub-critical Reynolds numbers". In: *Int. J. Heat Mass Transfer* 55, pp. 1343–1354.
- Roos, F. W. and W. W. Willmarth (1971). "Some experimental results on sphere and disk drag". In: *AIAA J.* 9, pp. 285–291.



- Schlichting, H. and K. Gersten (2003). *Boundary-layer Theory*. Springer Science & Business Media.
- Sierakowski, A. J. (2016). "GPU-centric resolved-particle disperse two-phase flow simulation using the Physalis method". In: *Phys. Commun.* 207, pp. 24–34.
- Sierakowski, A. J. and A. Prosperetti (2016). "Resolved-particle simulation by the Physalis method: Enhancements and new capabilities". In: *J. Comput. Phys.* 309, pp. 164–184.
- Stevens, R. J. A. M., R. Verzicco, and D. Lohse (2010). "Radial boundary layer structure and Nusselt number in Rayleigh-Bénard convection". In: *J. Fluid Mech.* 643, pp. 495–507.
- Tabata, M. and K. Itakura (1998). "A precise computation of drag coefficients of a sphere". In: *Int. J. Comput. Fluid Dyn.* 9, pp. 303–311.
- Whitaker, S. (1972). "Forced convection heat transfer correlations for flow in pipes, past flat plates, single cylinders, single spheres, and for flow in packed beds and tube bundles". In: *AIChE J* 18, pp. 361–371.
- Xia, J., K. Luo, and J. Fan (2014). "A ghost-cell based high-order immersed boundary method for inter-phase heat transfer simulation". In: *Int. J. Heat Mass Transfer* 75, pp. 302–312.

## Chapter 5

# Heat transfer from an array of fully-resolved particles in turbulent flow<sup>1</sup>

Much of what is currently theoretically known about the thermo-fluid-mechanics of the interaction of particles and a fluid is based on the point-particle model (see e.g. Zonta, Marchioli, and Soldati, 2011; Arcen, Tanière, and Khalij, 2012; Balachandar and Eaton, 2010) or the discrete-element model (see e.g. Hoef et al., 2008; Zhu et al., 2008). Both approaches suffer from the use of parameterized expressions for the hydrodynamic force and heat transfer coefficient in place of their evaluation on the basis of first principles. A few fully resolved simulations of the flow past individual particles exist, both in the laminar (e.g. Dennis, Walker, and Hudson, 1973; Kurose et al., 2012; Dandy and Dwyer, 1990; Kim and Choi, 2004) and turbulent (e.g. Dhole, Chhabra, and Eswaran, 2006; Bagchi and Kottam, 2008; Stadler, Rapaka, and Sarkar, 2014) regimes, but these studies do not provide information on the effects of particle-particle

---

<sup>1</sup>This chapter is based on a paper by the same title authored by Y. Wang and A. Prosperetti, submitted to *Phys. Rev. Fluid.*

interactions.

It is only recently that the situation has begun to change thanks to the development of various numerical methods capable of providing fully-resolved simulations of flows with many particles (see e.g. Glowinski et al., 2001; Uhlmann, 2005; Breugem, 2012; Tenneti and Subramaniam, 2014; Picano, Breugem, and Brandt, 2015; Sierakowski and Prosperetti, 2016; Uhlmann and Chouippe, 2017), which have begun to be extended to simulate thermal, in addition to mechanical, interactions (see e.g. Yu, Xiao, and Wachs, 2006; Feng and Michaelides, 2008; Feng and Michaelides, 2009; Wang et al., 2009; Deen et al., 2012; Deen et al., 2014; Tavassoli et al., 2013; Tenneti et al., 2013; Feng and Musong, 2014; Sun et al., 2016; Wang, Sierakowski, and Prosperetti, 2017; Ardekani et al., 2018).

These studies have begun to open up this field, which is of obvious importance for many applications such as fluidized beds, cooling towers, cloud formation and many others. Much work still remains to be done. For example, while Bagchi and Kottam (2008) studied a single particle in a turbulent flow, and many others studied particle interactions in pseudo-turbulence, no studies exist of particle interactions in a truly turbulent flow. The present study is a first contribution in this direction. By means of the recent extension of the PHYSALIS method to heat transfer problems (Wang, Sierakowski, and Prosperetti, 2017), we carry out resolved simulations of a planar array of fixed particles immersed in a decaying turbulent flow. Our focus is providing detailed information on the flow and heat transfer processes rather than developing correlations for engineering use. A simple analytic point-particle model

based on the Oseen equations sheds light on some of the numerical results.

## 5.1 Mathematical model and numerical method

We consider spherical particles in a non-isothermal, incompressible, constant properties Newtonian fluid. The Navier-Stokes equations are

$$\nabla \cdot \mathbf{u} = 0, \quad (5.1)$$

$$\frac{\partial \mathbf{u}}{\partial t} + \mathbf{u} \cdot \nabla \mathbf{u} = -\frac{1}{\rho} \nabla p + \nu \nabla^2 \mathbf{u}. \quad (5.2)$$

Here  $\mathbf{u}$ ,  $p$  are the velocity and pressure fields; the fluid density is denoted by  $\rho$  and the kinematic viscosity by  $\nu$ . The energy equation is

$$\frac{\partial T}{\partial t} + \mathbf{u} \cdot \nabla T = D \nabla^2 T, \quad (5.3)$$

with  $D = k/(\rho c_p)$  the thermal diffusivity of the fluid expressed in terms of the thermal conductivity  $k$  and specific heat  $c_p$ ; viscous heating is neglected on account of the smallness of this effect.

For simplicity, the particle temperature will be taken as  $T_p$ , fixed and the same for all the particles. The heat flow rate *into* the particles  $Q$  is given by

$$Q = k \oint_{s_p} \nabla T \cdot \mathbf{n}_p ds_p, \quad (5.4)$$

where  $s_p = 4\pi a^2$ , with  $a$  the particle radius, is the particle surface and  $\mathbf{n}_p$  is the outwardly-directed unit normal. The instantaneous Nusselt number for

each particle is defined by

$$Nu = \frac{2aQ/s_p}{k(T_i - T_p)} = \frac{1}{2\pi a(T_i - T_p)} \oint_{s_p} \nabla T \cdot \mathbf{n}_p ds_p, \quad (5.5)$$

in which  $k$  is the fluid thermal conductivity,  $T_i$  the temperature of the fluid far upstream of the particle and  $T_p$  is the particle temperature.

The problem is solved numerically by the PHYSALIS method, which is described briefly in Chapter 2 and in detail in several papers (see e.g. Gudmundsson and Prosperetti, 2013; Sierakowski and Prosperetti, 2016) for what concerns the particles-fluid momentum interaction and, in Chapter 4 for what concerns the particles-fluid thermal interaction.

## 5.2 Description of the simulations

We simulate the decaying turbulent flow past an array of nine equal spherical particles arranged in a regular square array of side  $d = 5a$  on a plane perpendicular to the mean velocity  $U$  of the incident flow. The particle Reynolds number based on the mean streamwise velocity  $U$  is  $Re_p = 2aU/\nu = 120$  and the turbulence Taylor Reynolds number at the particle plane is  $Re_\lambda = 30.2$ . The Kolmogorov length scale is  $\eta \sim a/10$  and the Prandtl number  $Pr = 1$ .

The computational domain is a parallelepiped with a square cross section with sides of length  $15a$  in the cross-stream direction and a length of  $24a$  in the flow direction. The particle array is centered on the parallelepiped cross section, with the outermost particles at a distance  $d/2$  from the surfaces of the computational domain parallel to the flow. Thus, as far as the geometry is concerned, the situation considered is equivalent to the infinite repetition of a

fundamental unit consisting of a parallelepiped with a square cross section of size  $d \times d$  perpendicular to the mean flow and having a single particle on its axis. Since the flow is unsteady and turbulent, this periodicity holds only in a time-average sense but not instantaneously. On the sides of the computational domain parallel to the mean flow we impose periodicity conditions, which enforce instantaneous periodicity across these surfaces. At the exit of the computational domain the normal derivative of the normal velocity vanishes and the in-plane derivatives of the tangential velocity components also vanish.

Isotropic, homogeneous turbulence with  $Re_\lambda = 43$  is generated in an auxiliary cubic domain with sides of length  $15a$  using the linear forcing scheme of Lundgren (2003) (see also Rosales and Meneveau, 2005; Carroll and Blanquart, 2013). This turbulent field, augmented by a constant velocity  $U$  along the  $z$  direction, is then imposed at the inlet of the primary domain containing the particles, in the manner described in Botto and Prosperetti (2012) and Wang, Sierakowski, and Prosperetti (2017). The eddy turn-over time is 3.5 times shorter than the convection time over the length of the computational domain, which ensures the absence of artificial periodicity as discussed in Botto and Prosperetti (2012). We checked that the features of the turbulence, and in particular the intensity and integral length scales, matched the results reported in Rosales and Meneveau (2005). The characteristics of the incident flow at the plane occupied by the particles are summarized in Table 5.1.

The particle centers are placed on the plane  $z = 0$  at a distance of  $4.5a$  from the inlet face of the domain, which is sufficient to avoid an interference between the particles and the inlet boundary condition. The incident flow

$Re_\lambda$	$a/\eta$	$\tau_E v/a^2$	$\lambda_g/a$	$\ell/a$	$u'/U$
30.2	10.4	0.114	1.07	2.18	45%

**Table 5.1:** Characteristics of the incident turbulence at the particles plane;  $Re_\lambda$  is the Taylor Reynolds number,  $\eta$  is the Kolmogorov length,  $a$  the particle radius,  $\tau_E$  the eddy turn-over time,  $\ell$  the integral length scale and  $u'$  the root-mean square turbulent velocity fluctuations.

is at the reference temperature  $T_i$  while all the particles are kept at a fixed temperature  $T_p < T_i$ . In order to calculate reasonably converged average values, we performed simulations corresponding to 10 different realizations of the incident turbulent flow, each one lasting 45 eddy turn-over times  $\tau_E$ . Averages were collected excluding an initial period of duration  $10\tau_E$ . For each realization, we performed two different simulations, with and without the particles in place. The latter simulations were used to characterize the flow incident on the particles. Another simulation of the laminar flow at the same Reynolds number was also run.

In the numerical implementation of the PHYSALIS method we use 15 cells per radius to guarantee an adequate description of the interaction of the particle with the intense turbulent gusts by which it is buffeted. The Lamb series on which the method is based (see e.g. Sierakowski and Prosperetti, 2016) is truncated at level 2 for the momentum and 4 for the temperature. The total number of cells is  $180 \times 180 \times 288$ . The Courant number was 0.5.

In view of the periodicity conditions on the lateral surfaces, upon integrating the momentum equation (5.2) over the entire computational domain,

using the divergence theorem and averaging over time we find

$$A(p_{-\infty} - p_{\infty}) = \sum_{j=1}^{N_p} \bar{f}_j, \quad (5.6)$$

in which  $A = (3d) \times (3d)$  is the cross-stream area of the computational domain,  $N_p = 9$  the number of particles and  $f_j$  is the component of the instantaneous hydrodynamic force on the  $j$ -th particle in the mean flow direction. If  $\langle \bar{f} \rangle$  is the mean force per particle, this relation gives

$$(p_{-\infty} - p_{\infty})d^2 = \langle \bar{f} \rangle, \quad (5.7)$$

where  $d^2$  is the area of the cross-stream section associated with each particle.

A similar procedure applied to the energy equation (5.3) gives

$$\rho c_p A (\overline{Tu_x}|_{\infty} - UT_i) = - \sum_{j=1}^{N_p} \bar{Q}_j, \quad (5.8)$$

where  $\overline{Tu_x}|_{\infty}$  denotes the average value of  $Tu_x$  far downstream of the particle plane. In terms of the average heat transferred by each particle, this is

$$\rho c_p d^2 (\overline{Tu_x} - UT_i) = - \langle \bar{Q} \rangle. \quad (5.9)$$

If the downstream boundary is taken far enough, we may expect that  $\overline{Tu_x} \simeq UT_{\infty}$ . With this approximation and (5.5) this relation gives

$$\frac{T_i - T_{\infty}}{T_i - T_p} \simeq \frac{4\pi a^2}{d^2} \frac{Nu}{Pr Re_p}, \quad (5.10)$$

in which  $Nu$  is interpreted as the Nusselt number averaged over time and all the particles. With the present result  $Nu \simeq 9.72$  (see section 5.4.1 below) the fraction in the right-hand side is approximately equal to 0.0407.



### 5.3 Simplified point-particle model

Before presenting the results of the simulation, it is useful to briefly discuss the predictions of a simple point-particle model, which is helpful to interpret some features of the numerical results.

We consider an infinite planar regular square array of point particles, separated by a distance  $d$  from their closest neighbors, located at  $z = 0$ , perpendicular to an incident laminar flow with constant velocity  $U$ . In view of symmetry, it is sufficient to study the problem in a domain  $-\frac{1}{2}d < x, y < \frac{1}{2}d, -\infty < z < \infty$ ) with a single particle located at  $x = y = z = 0$ . We solve the problem in the low-Reynolds-number limit by considering the continuity equation (5.1) and the momentum equation in the Oseen form:

$$U \frac{\partial \hat{\mathbf{u}}}{\partial z} = -\frac{1}{\rho} \nabla p + \nu \nabla^2 \hat{\mathbf{u}} - \frac{f}{\rho} \mathbf{k} \delta(x) \delta(y) \delta(z), \quad (5.11)$$

where  $\mathbf{k}$  is a unit vector in the flow direction,  $f$  is the force exerted by the fluid on the particle and  $\hat{\mathbf{u}}$  is the perturbation velocity defined so that the three components of the velocity field in the  $x$ ,  $y$  and  $z$  directions are given by  $\mathbf{u} = (\hat{u}_x, \hat{u}_y, U + \hat{u}_z)$ , respectively. We consider a similar approximation to the energy equation (5.3), namely

$$U \frac{\partial T}{\partial z} = D \nabla^2 T - \frac{Q}{\rho c_p} \delta(x) \delta(y) \delta(z), \quad (5.12)$$

with  $Q$  the heat absorbed by each particles from the fluid per unit time.

The solution of the problem can be expressed in the form (see e.g. Lagerstrom, 1964; Prosperetti, 1976)

$$\hat{\mathbf{u}} = \hat{\mathbf{u}}_L + \hat{\mathbf{u}}_T, \quad (5.13)$$

where

$$\hat{\mathbf{u}}_L = -\frac{\nabla\phi}{U}, \quad \hat{\mathbf{u}}_T = \chi\mathbf{k} - \frac{\nu}{U}\nabla\chi, \quad (5.14)$$

in which the scalar potential  $\phi$  satisfies the Poisson equation

$$\nabla^2\phi = -\frac{f}{\rho}\delta(x)\delta(y)\delta(z), \quad (5.15)$$

and the auxiliary function  $\chi$  satisfies

$$U\frac{\partial\chi}{\partial z} = \nu\nabla^2\chi - \frac{f}{\rho}\delta(x)\delta(y)\delta(z). \quad (5.16)$$

A remarkable aspect of this set-up is the identity in form of the energy equation (5.12) and the equation for  $\chi$ .

The solution of the problem is straightforward and is given in detail in 5.A. Here it is sufficient to show the results for  $\hat{u}_{L,z} = -(\partial\phi/\partial z)/U$  and  $\chi$  in the region downstream of the particles,  $z > 0$ . It is found that

$$\hat{u}_{L,z} = \frac{f}{2\rho Ud^2} \left( 1 + \sum_{k=-\infty}^{\infty} \sum_{n=-\infty}^{\infty} \exp[-\lambda_{nk}z/d + 2\pi i(kx + ny)/d] \right), \quad (5.17)$$

where

$$\lambda_{nk} = 2\pi\sqrt{n^2 + k^2}. \quad (5.18)$$

Correlation	Reference	$Nu$
$Nu = 2 + 0.6Re_p^{1/2}Pr^{1/3}$	Ranz and Marshall, 1952	8.57
$Nu = 2 + [0.4Re_p^{1/2} + 0.06Re_p^{2/3}]Pr^{0.4}$	Whitaker, 1972	7.84
$Nu = 0.922 + [1 + 0.1Re_p^{1/3}]Re_p^{1/3}Pr^{1/3}$	Feng and Michaelides, 2000	8.29
Equation (5.21), $\alpha = 0.97$	Gunn, 1978	9.41
Equation (5.21), $\alpha = 0.87$	Gunn, 1978	10.1
Present result	–	$9.72 \pm 0.78$

**Table 5.2:** Nusselt number predicted by several correlations for steady laminar flow past an isolated sphere, and by Gunn’s correlation for a sphere in a particle bed, compared with the result of the present simulations;  $\alpha$  is the fluid volume fraction.

The auxiliary function  $\chi$  is given by

$$\chi = -\frac{f}{\rho Ud^2} \sum_{n=-\infty}^{\infty} \sum_{k=-\infty}^{\infty} \frac{\exp[-\mu_{nk}z/d + 2\pi i(nx + ky)/d]}{\sqrt{1 + \frac{4\pi^2(n^2+k^2)}{(Ud/2v)^2}}} \quad (5.19)$$

with

$$\mu_{nk} = \left( \sqrt{1 + \frac{4\pi^2(n^2+k^2)}{(Ud/2v)^2}} - 1 \right) \frac{Ud}{2v}. \quad (5.20)$$

It is easily shown that  $\mu_{nk} < \lambda_{nk}$  for any non-negative value of  $Ud/2v$ . Thus, one would expect that the character of the velocity perturbation will be mostly determined by the auxiliary function  $\chi$  and should therefore have strong similarities with that of the temperature perturbation. It may be noted from the expressions for  $\hat{u}_{L,z}$  and  $\chi$  that decreasing  $d$  increases the spatial decay rate of velocity and temperature perturbations.

## 5.4 Results

### 5.4.1 Heat transfer rate

Table 5.2 compares the present results for the sphere Nusselt number, averaged over time and particles, with those predicted by several correlations originally developed for isolated spheres in steady laminar flow. Heat transfer is expected to be favored by turbulence and, indeed, our results lie above those of the single-sphere laminar correlations. As noted by Bagchi and Kottam, 2008 for the case of a single sphere, the laminar-turbulent difference is not large in spite of the strong intensity of the turbulence. The small magnitude of the effect is particularly striking in view of the large differences between the laminar and turbulent thermal wakes shown in figure 5.5. Most of the heat transfer takes place in the neighborhood of the instantaneous front stagnation point, which, in a turbulent flow continuously shifts. It is interesting to observe that the increase of the local Nusselt number with respect to the laminar case is approximately the same over the entire surface. A factor contributing to the increased heat transfer is the presence of the other spheres. Gunn, 1978 gives a correlation for the mean single-particle Nusselt number for particles in a particle bed

$$Nu = (7 - 10\alpha + 5\alpha^2)(1 + 0.7Re_s^{0.2}Pr^{1/3}) + (1.33 - 2.4\alpha + 1.2\alpha^2)Re_s^{0.7}Pr^{1/3}, \quad (5.21)$$

in which  $\alpha$  the fluid volume fraction and  $Re_s = \alpha Re_p$  is the Reynolds number based on the superficial velocity. A straightforward application of this expression to our situation is hampered by the fact that in our case particles are not

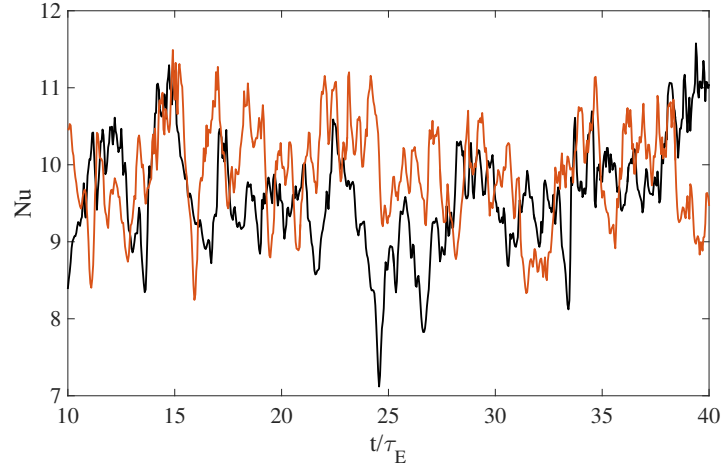


**Figure 5.1:** Examples of the instantaneous Nusselt number vs. time for two different spheres;  $\tau_E$  is the eddy turn-over time.

uniformly distributed in the computational domain. An effective particle volume fraction may be expected to lie between the ratio of the particle volume to the volume of a cubic box with a side equal to the inter-particle spacing, which gives  $\alpha \simeq 0.97$ , and the ratio of the cross sectional area occupied by the particles to the cross sectional area of the domain, which gives  $\alpha \simeq 0.87$ . As shown in Table 5.2, the predictions of Gunn’s correlation for these two estimates of  $\alpha$  bracket our numerical result. Due to the intensity of the turbulence, about 45%, the calculated instantaneous Nusselt number fluctuates considerably as shown in the examples of figure 5.1.

The local Nusselt number over the particle surface, defined by

$$Nu_{loc} = \frac{2a}{T_i - T_p} \mathbf{n}_p \cdot \nabla T, \quad (5.22)$$

with  $\mathbf{n}_p$  the outward unit normal, averaged over time and particles, is shown in figure 5.2 (solid line), where the dashed line is the result for a sphere in

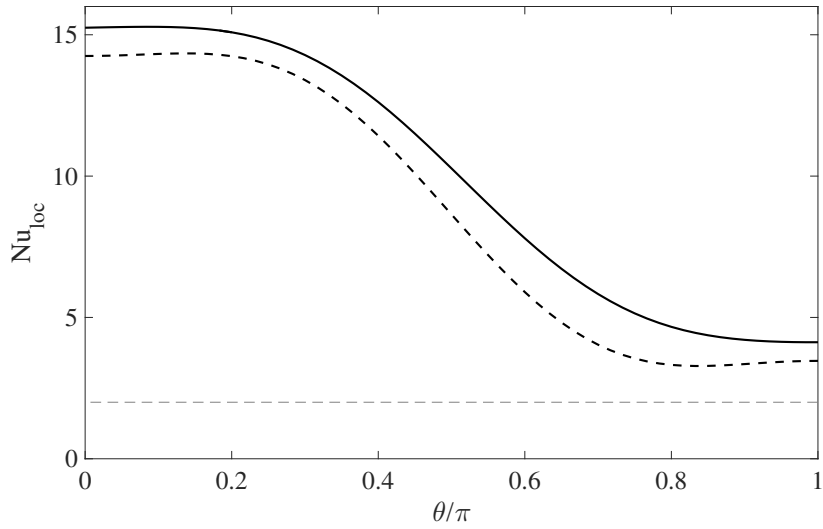


**Figure 5.2:** Average local Nusselt number over the spheres' surface;  $\theta = 0$  and  $\pi$  are the front and rear stagnation points, respectively. The thick dashed line is for laminar flow; the lightly dashed line is the pure conduction limit  $Nu = 2$ .

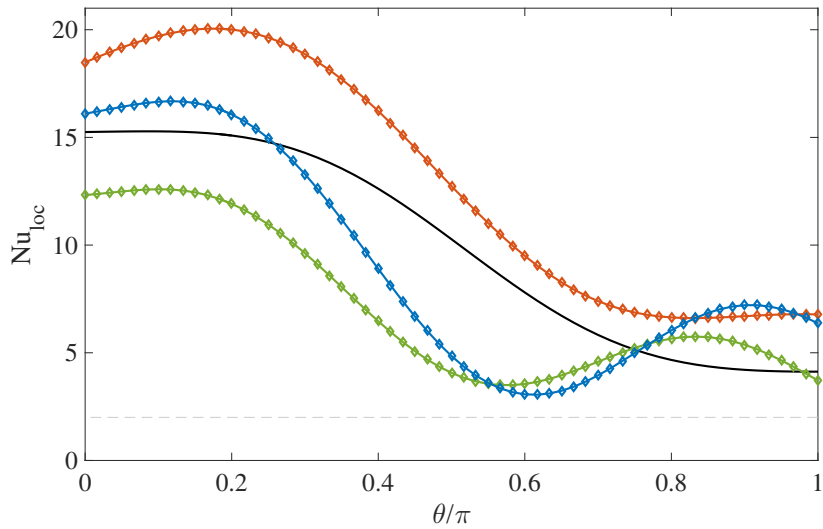


**Figure 5.3:** Three examples of the instantaneous local Nusselt number. The solid line is the mean value shown in figure 5.2 and the lightly dashed line the pure conduction limit  $Nu = 2$ .

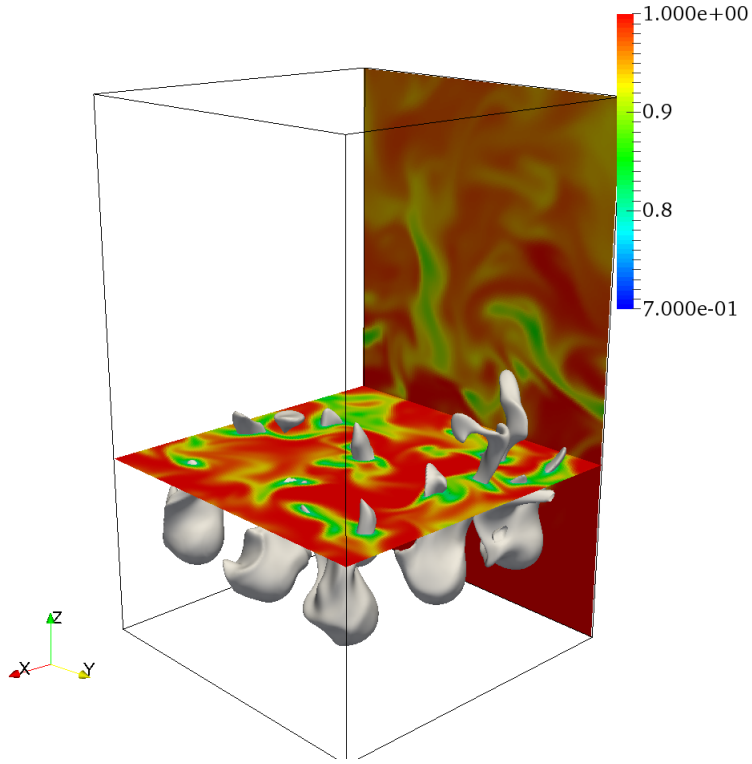


**Figure 5.4:** Snapshot of the normalized temperature  $T_* = (T - T_p)/(T_i - T_p)$  in the flow studied in this paper; the isosurfaces correspond to  $T_* = 0.8$ .

laminar flow at the same  $Re_p$ . Turbulence is seen to increase  $Nu_{loc}$  at every position over the sphere surface. Just as the overall Nusselt number, this quantity also fluctuates considerably, as can be seen from the examples shown in figure 5.3. There are also minor variations (not shown) depending on the specific meridian along which  $Nu_{loc}$  is calculated for each sphere.

### 5.4.2 Mean field

Figure 5.4 gives an impression of the instantaneous normalized temperature

$$T_* = \frac{T - T_p}{T_i - T_p}, \quad (5.23)$$

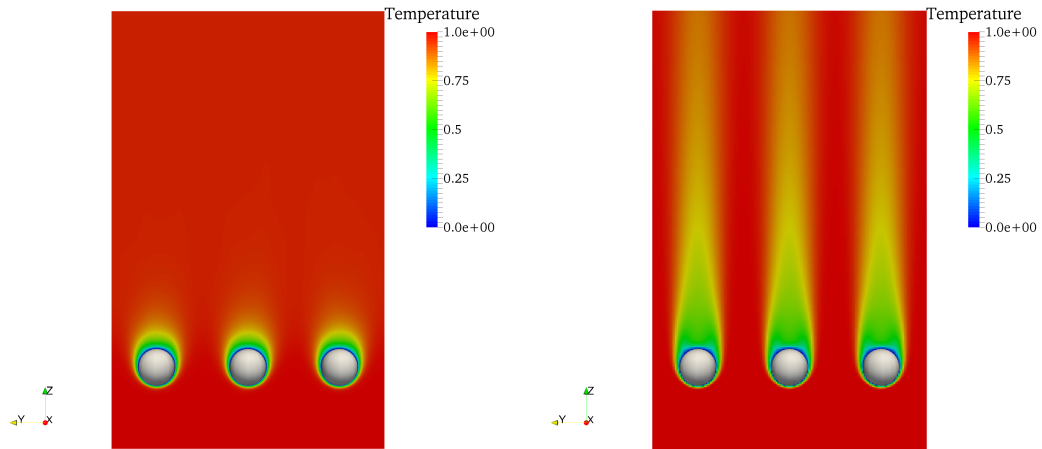


**Figure 5.5:** Comparison between the time-mean normalized temperature distribution on a plane parallel to the mean velocity through the centers of three contiguous particles for turbulent flow (left) and for laminar flow.

as found in the present simulations; the isosurfaces correspond to  $T_* = 0.8$ . The large regions of  $T_*$  close to 1 show that the effect of the cooling due to the particles remains mostly localized in their wakes except for the turbulent fluctuations.

The time-mean normalized temperature distribution on a plane through the centers of three contiguous particles is shown by the left diagram of figure 5.5. The right diagram permits a comparison with the temperature distribution in the analogous steady laminar flow at the same  $Re_p$ . The great effectiveness of turbulent transport in mixing the fluid in the thermal wakes of the particle is evident here.

A contour plot of the temperature field near the spheres averaged over time and over particles on planes parallel to the mean flow through the particles center is shown in figure 5.6. One notices a weak cooling of the fluid upstream



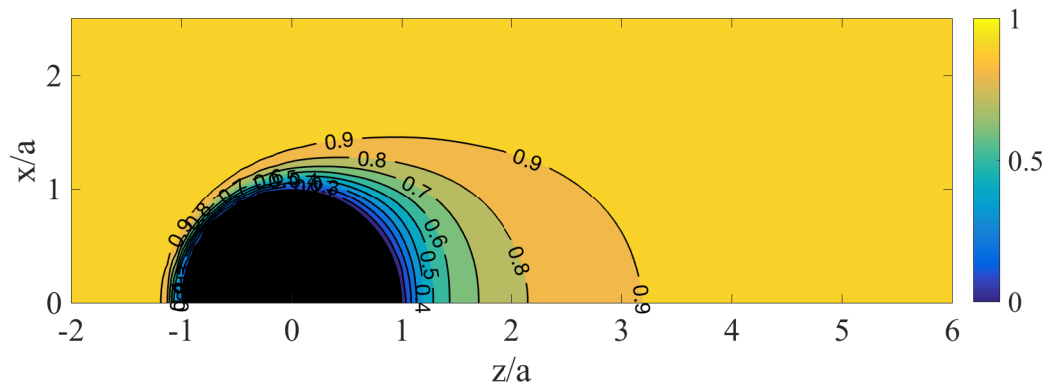


**Figure 5.6:** Contour plot of the normalized average temperature field  $(T - T_p)/(T_i - T_p)$  on a plane parallel to the flow direction through the particle center.

of the particles and a rather short mean thermal wake. Although in their simulations of turbulent flow past an isolated sphere Bagchi and Kottam, 2008 do not show simulations for our Reynolds number, their results for  $Re_p = 65$  and 250 suggest that the thermal wake in our case is indeed shorter than for an isolated sphere. The simple analytical model of the previous section, which implies that decreasing the separation between the particles shortens the thermal wake, offers a plausible explanation. The root of this behavior lies in the effect of cross-stream conduction: the presence of the other particles limits the widening of the wake so that conduction is more effective in bringing the temperature in the wake closer to that of the incident flow.

A similar contour plot for the average streamwise velocity component is shown in figure 5.7. The appearance of this figure is quite different from that for the temperature contour plot in the previous figure, which is somewhat unexpected from the simple Oseen model. Indeed, as noted before, this model suggests that the influence of the pressure field should decay faster than that of viscous diffusion so that the velocity distribution should be dominated by

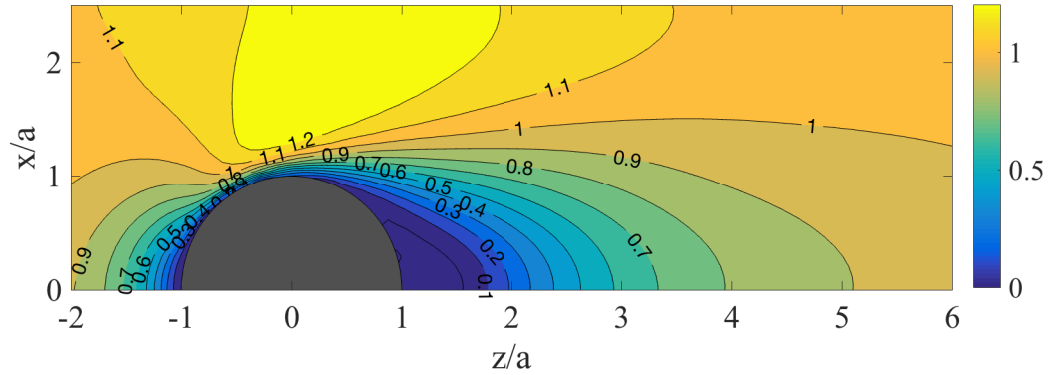


**Figure 5.7:** Contour plot of the normalized average streamwise velocity field  $u_z/U$  on a plane parallel to the flow direction through the particle center.

the latter. For our case of  $Pr = 1$  one would then expect similar results for velocity and temperature. The reason for the large difference between these two quantities is the blockage of the flow due to the finite size of the particles, an effect not accounted for in the Oseen model. The flow velocity increases considerably in the gap between adjacent spheres, with the consequence that the momentum wake extends considerably farther downstream than the thermal wake.

The upper diagram in figure 5.8 shows the decay of the temperature deficit  $(T_i - T)/(T_i - T_p)$ , averaged over time and over particles, along lines parallel to the flow direction through the particles center; the dashed line is for the case in the absence of turbulence. This result is very similar to that shown in figure 14 of Bagchi and Kottam, 2008. The effectiveness of the turbulent fluctuations in restoring the expected mean value of the temperature estimated earlier in equation (5.10) is confirmed once again. This asymptotic value is found to be 0.0413, gratifyingly close to the estimate 0.0407 given earlier in equation (5.10). The solid line in the lower diagram compares the analogous quantity

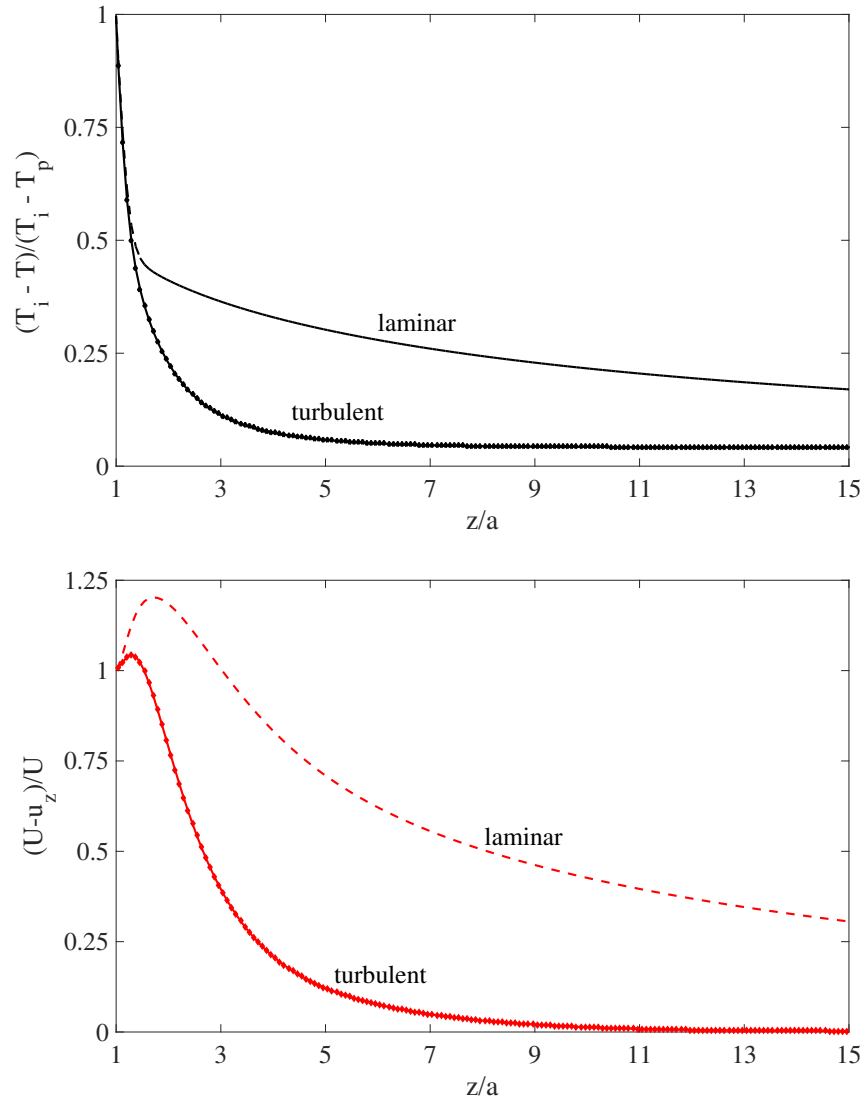


**Figure 5.8:** Average normalized temperature deficit  $(T_i - T)/(T_i - T_p)$  (upper diagram) and velocity deficit  $(U - u_z)/U$ , vs. distance along a line through the particle center parallel to the mean flow;  $z/a = 1$  is the rear stagnation point of the particle.

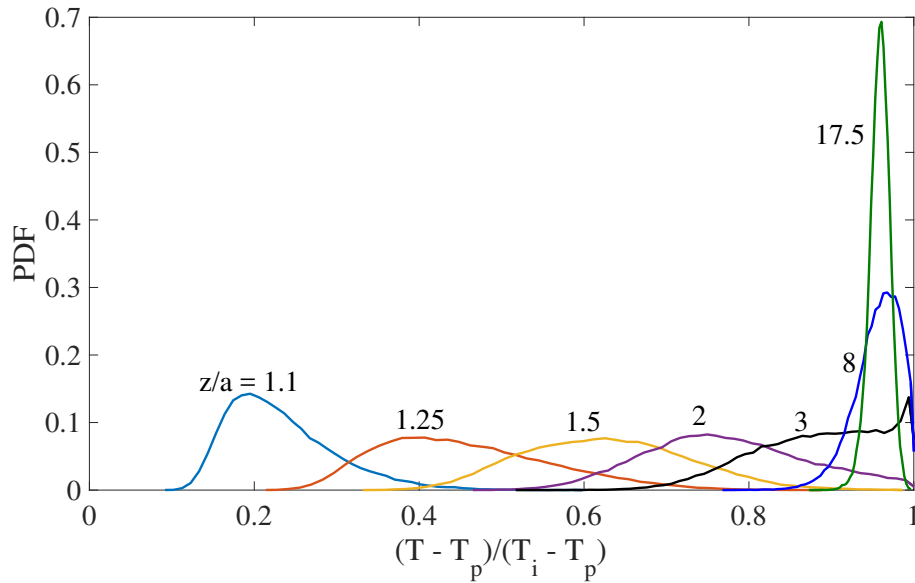


**Figure 5.9:** Probability density function of the temperature along a line through the sphere center parallel to mean flow; the sphere center is at  $z = 0$ . From left to right the curves are for  $z/a = 1.1, 1.25, 1.5, 2, 3, 8, 17.5$ .

for the streamwise velocity,  $(U - u_z)/U$ , with the laminar result shown by the dashed line. The effectiveness of the turbulent mixing process is again apparent. The small local maximum near the particle surface is due to the recirculation in the near-wake. This line crosses the level  $(U - u_z)/U = 1$  around  $z/a \simeq 1.5$ , which gives an estimate of the extent of the recirculation region behind the sphere.

The probability density function (PDF) of the temperature along a line through the spheres centers parallel to mean flow is shown in figure 5.9 at different distances downstream of the spheres. Since in the present simulation the spheres are cold, the temperature at the peak of the PDF's increases with downstream distance. At intermediate distances the PDF broadens

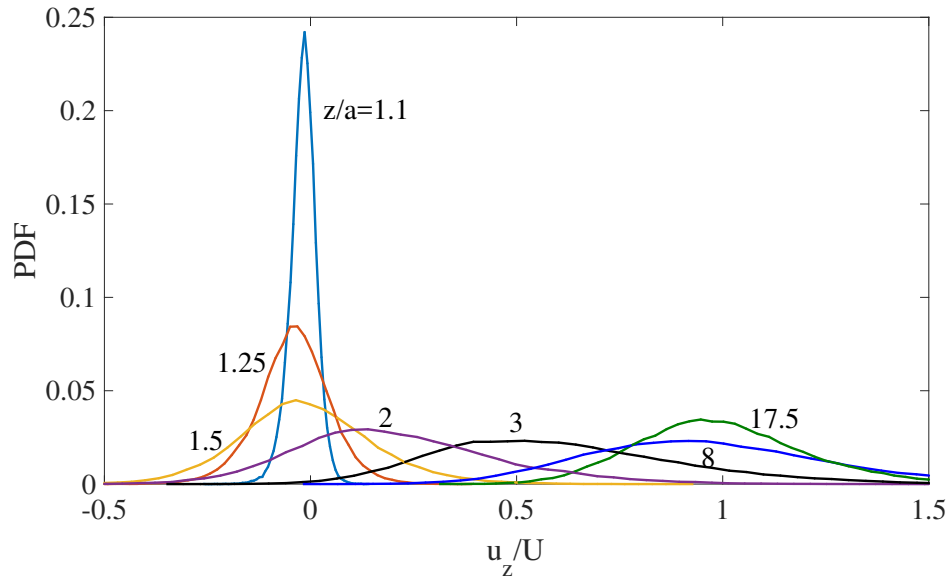


**Figure 5.10:** Probability density function of the streamwise velocity along a line through the sphere center parallel to mean flow; the sphere center is at  $z = 0$ . From left to right the curves are for  $z/a = 1.1, 1.25, 1.5, 2, 3, 8, 17.5$ .

reflecting the larger velocity fluctuations unimpeded by the effect of the no-slip condition, but after a few diameters the PDF becomes very narrow and centered about the mean fluid temperature estimated earlier in equation (5.10). The recirculating flow behind the particle, which ends at about  $z/a = 1.5$ , does not seem to have much of an effect on these PDFs.

The analogous PDF for the normalized streamwise velocity  $u_z/U$ , figure 5.10, shows an opposite trend. Very near the sphere the velocity is slightly negative and narrowly distributed close to zero, and gradually recovers a mean value close to that of the incident flow downstream. Since, for the velocity, there is no effect analogous to the permanent cooling of the fluid caused by the spheres, the mean velocity far downstream must equal the mean of the incident velocity. There is a significant difference between the PDFs for  $z/a$

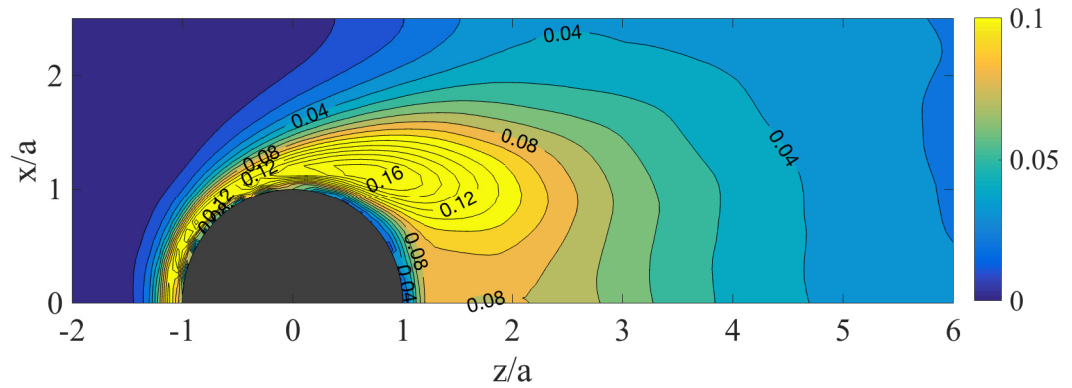


**Figure 5.11:** Contour plots of the root-mean-square normalized temperature fluctuations defined in equation (5.24).

less than 1.5, which are in the recirculating region of the wake, and those for  $z/a > 1.5$ , which are much broader.

### 5.4.3 Fluctuating field

Contour plots of the root-mean-square (RMS) temperature fluctuations are shown in figure 5.11. The quantity plotted here is normalized and defined by

$$RMS(T_*) = \sqrt{\overline{(T_* - \bar{T}_*)^2}}. \quad (5.24)$$

Very near the sphere, velocity and velocity fluctuations are small and therefore so are the temperature fluctuations. Far downstream the cooling effect of the sphere is small and therefore, again, so are the temperature fluctuations. The fluctuations are most intense in the high-velocity region close to the sphere downstream of the separation point. A small region of relatively high fluctuations is also visible just upstream of the sphere where the region around the stagnation point is subject to the impingement of incoming eddies.

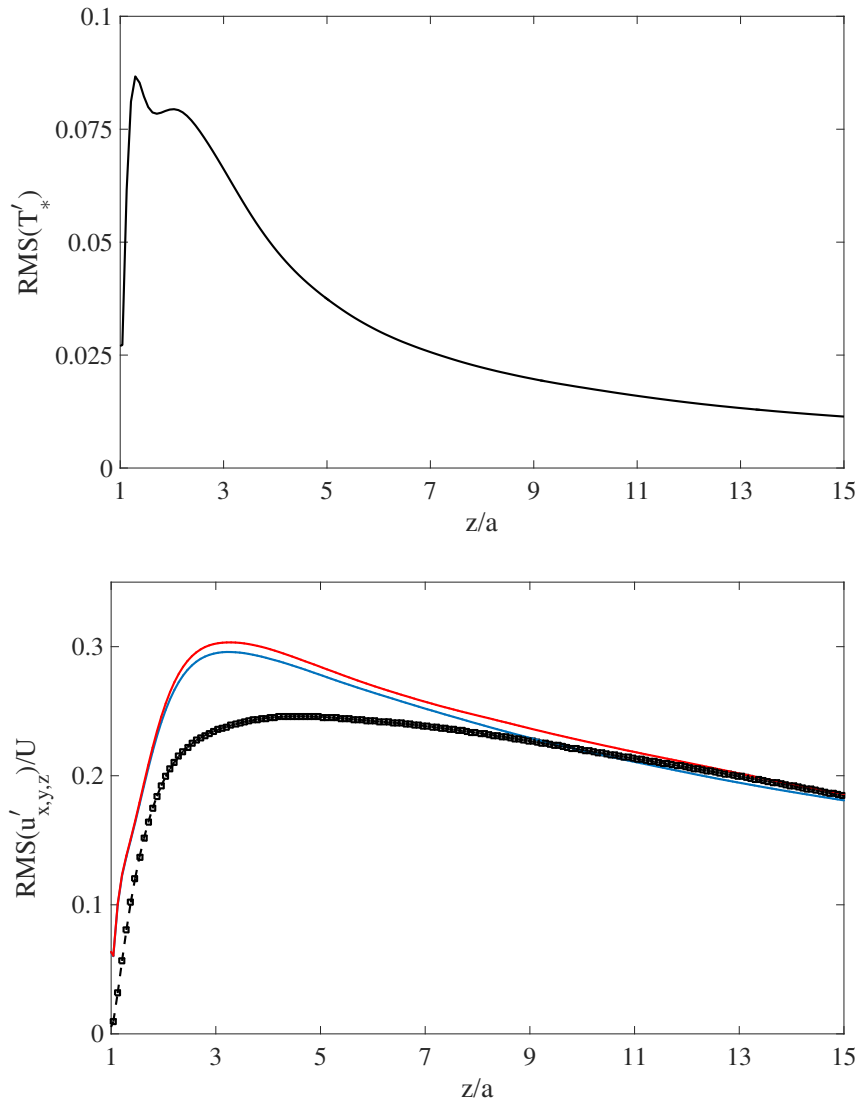


**Figure 5.12:** Dependence of the root-mean-square temperature (upper diagram) and velocity fluctuations vs. distance along a line through the particle center parallel to the mean flow;  $z/a = 1$  is the rear stagnation point of the particle. In the lower diagram the upper two lines show the fluctuations of the two cross-stream velocity components; the thick line is for the streamwise velocity.

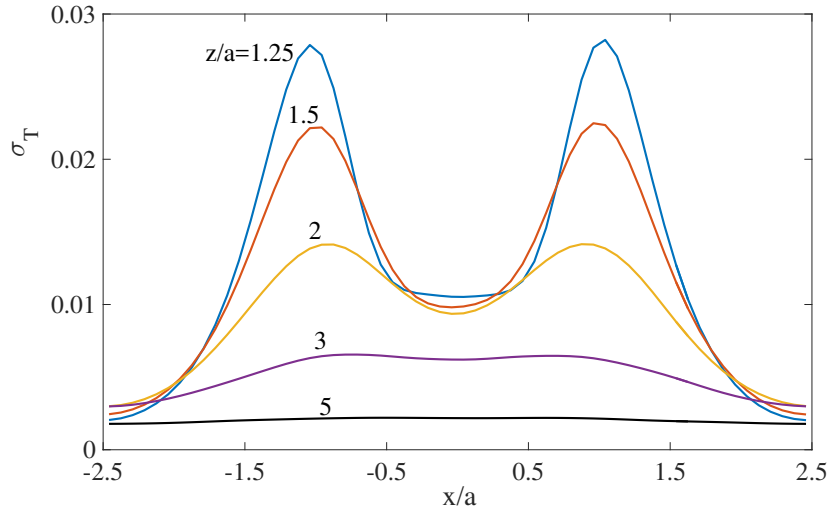


**Figure 5.13:** Normalized temperature variance  $\sigma_T = \overline{T'^2}/(T_i - T_p)^2$  in the cross-stream direction at different downstream distances from the sphere. In descending order of the maxima, the lines are for  $z/a = 1.25, 1.5, 2, 3$  and  $5$ ; the particle center is on the plane  $x = 0$ .

More detailed information on the decay of the RMS temperature fluctuations, defined as in (5.24), and normalized velocity components,  $RMS(u'_{x,y,z})/U$ , in the particle's wake is shown in figure 5.12. The recirculating flow in the near wake contributes a small region of enhanced temperature fluctuations near the particle. The two thin lines in the lower diagram show the RMS fluctuations of the velocity components in the cross-stream directions,  $u'_x/U$  and  $u'_y/U$ . Their near identity gives an idea of the degree of convergence of the averaging used to present our results. The thick line shows the RMS of the streamwise component  $u'_z/U$ . The three results converge a few diameters downstream of the sphere, but significant differences are visible further upstream in the recirculating region of the wake strongly buffeted by the incident turbulence.

A quantity related to fluctuations is the temperature variance  $\sigma_T = \overline{T'^2}/(T_i -$



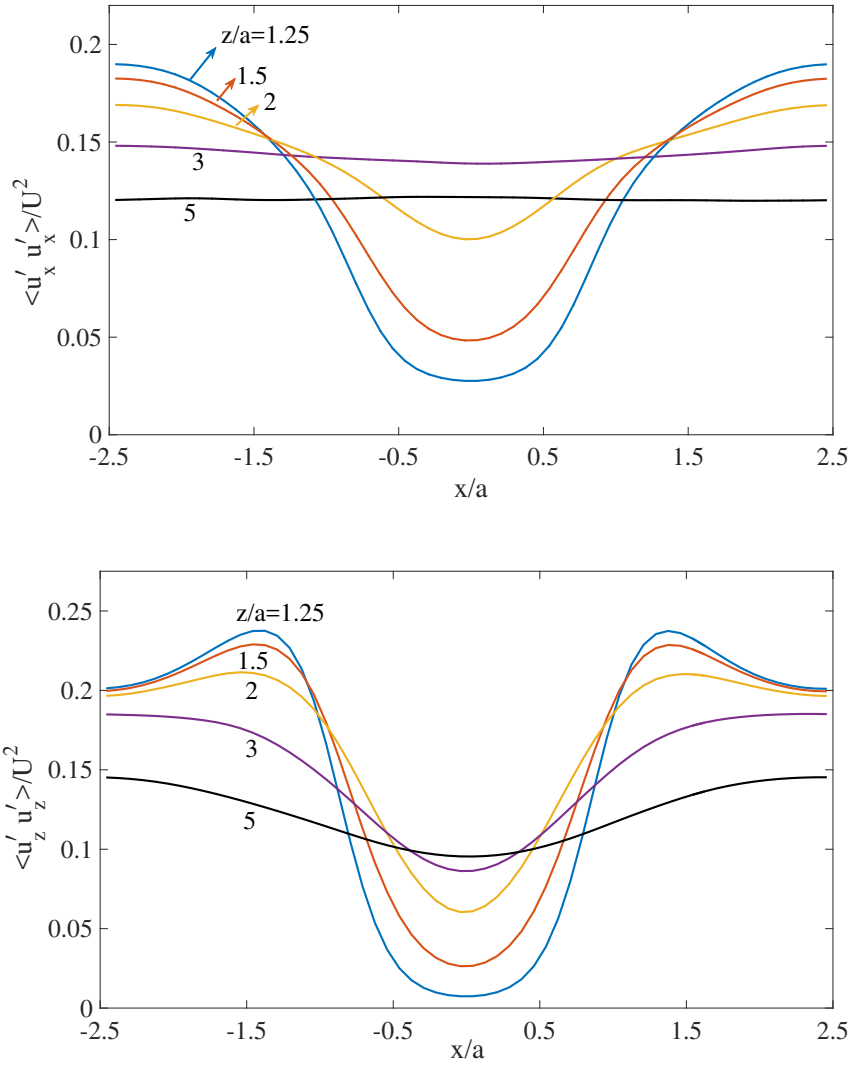


**Figure 5.14:** Normalized diagonal turbulent Reynolds stress  $u'_x u'_x / U^2$  (upper diagram) and  $u'_z u'_z / U^2$  in the cross-stream planes at downstream distances from the sphere  $z/a = 1.25, 1.5, 2, 3$  and  $5$ ; the particle center is on the plane  $x = 0$ .

$T_p)^2$ . The distribution of this quantity in the cross-stream direction downstream of the particles is shown in figure 5.13. The maxima are located in the intensely fluctuating region already shown in figure 5.9. The decay of these features with distance is however very rapid as could be expected, for example, already on the basis of the left diagram of figure 5.5.

The analogous quantities for the velocity are the normalized diagonal components  $u'_x u'_x / U^2$  and  $u'_z u'_z / U^2$  of the Reynolds stresses. These quantities, averaged over time and particles, are shown in figure 5.14 at different distances downstream of the spheres. Both components are symmetric about the line through the particle center. The cross stream component  $u'_x u'_x / U^2$  is monotonic on both sides of the symmetry line and shows the expected broadening and shallowing of the wake with distance. The component along the mean flow,  $u'_z u'_z / U^2$ , on the other hand, exhibits characteristic maxima near the edges of the wake as reported in earlier studies see e.g. Botto and Prosperetti, 2012. These structures are located outside the recirculating region of the wake, but in the same range of  $z/a$ . A possible explanation is that the unsteady nature of the flow near the separation line induces strong velocity components in the cross-stream plane which tilt and stretch the vorticity of the incident turbulent eddies thus reinforcing fluctuations in the streamwise velocity.

The normalized turbulent heat transport in the cross-stream directions,  $\overline{u'_{x,y} T'} / U(T_i - T_p)$ , is shown as a function of distance  $x$  from the sphere axis at different downstream distances in figure 5.15. The symmetry about the midplane  $x = 0$  again testifies to the good convergence of the averaging.

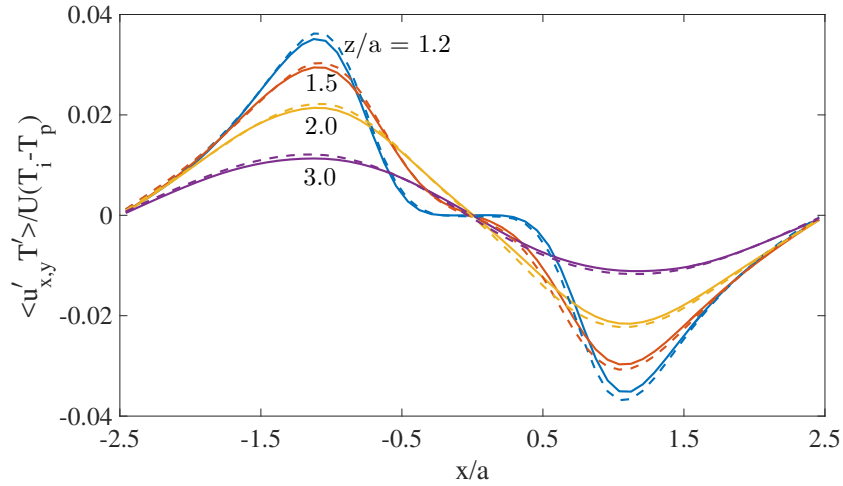


**Figure 5.15:** Dependence of the average  $x$  (solid lines) and  $y$  components of the turbulent heat flux on distance from the sphere axis at downstream locations  $z/a = 1.2, 1.5, 2$  and  $3$ ; the particle center is on the plane  $x = 0$ .

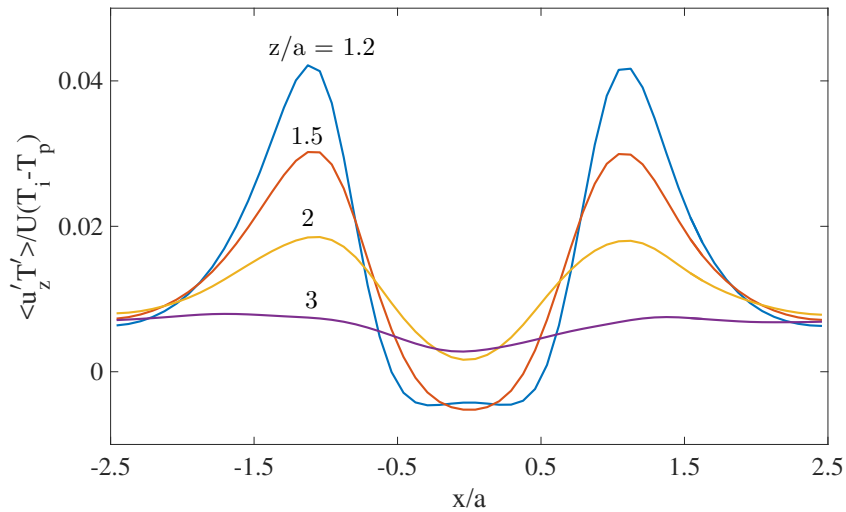


**Figure 5.16:** Dependence of the average  $z$ -components of the turbulent heat flux on distance from the sphere axis at downstream locations  $z/a = 1.2, 1.5, 2$  and  $3$ ; the particle center is on the plane  $x = 0$ .

Comparison with figures 5.9, 5.13 and 5.14 shows that the maxima/minima are mostly due to the temperature, rather than the velocity, fluctuations. In the case of the  $z$  component,  $\overline{u'_z T'}/U(T_i - T_p)$ , shown in figure 5.16, the  $u'_z$  velocity fluctuations combine with the temperature fluctuations to give somewhat stronger maxima.

The temperature variance  $\overline{T'^2}$  satisfies the equation (see e.g. Pope, 2000)

$$\frac{d\overline{\frac{1}{2}T'^2}}{dt} = -\nabla \cdot \Phi_T + \mathcal{P}_T - \epsilon_T, \quad (5.25)$$

in which the left-hand side is the convective derivative of the variance,

$$\Phi_T = \overline{\frac{1}{2}T'^2 \mathbf{u}'} - \frac{1}{2}D\nabla\overline{T'^2}, \quad (5.26)$$

is the turbulent transport,

$$\mathcal{P}_T = -\overline{T' \mathbf{u}'} \cdot \nabla \overline{T}, \quad (5.27)$$

is the production and

$$\epsilon_T = D\overline{\nabla T' \cdot \nabla T'}, \quad (5.28)$$

is the dissipation. Cross-stream graphs of these three terms are shown in the two panels of figure 5.17 at  $z/a = 1.2$  and  $1.5$ . The production (red line) has two relatively intense regions, one in the recirculating part of the wake and one just outside it, separated by a minimum located close to the streamline enclosing the mean recirculation. Across this line the turbulent transport (black line) changes sign.

A final point of interest concerns the time scales for mechanical and thermal

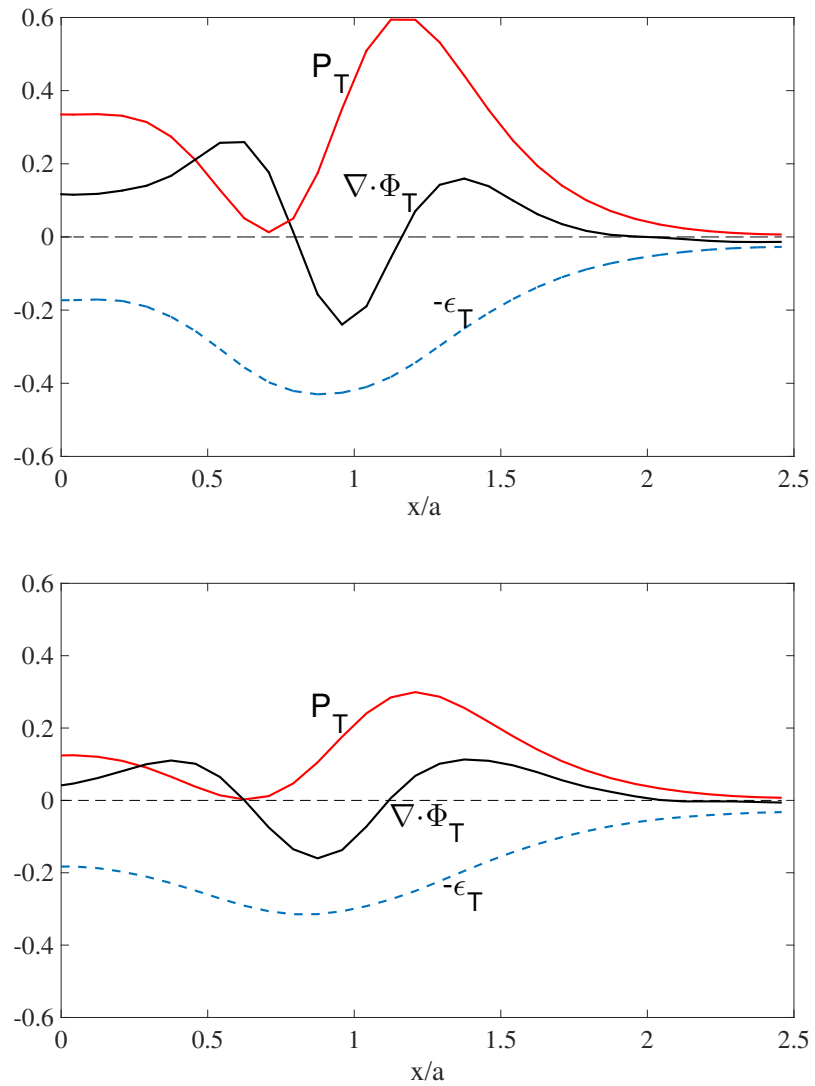


**Figure 5.17:** The three terms in the energy budget equation (5.25) as functions of the cross-stream coordinate at  $z/a = 1.2$  (upper diagram) and 1.5.

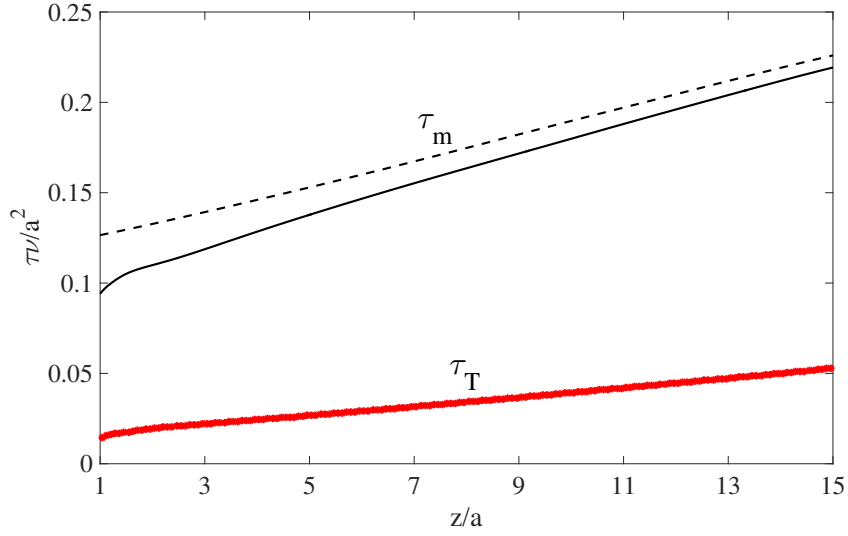


**Figure 5.18:** Mechanical (upper two lines) and thermal time scales, defined in (5.29), as functions of the downstream distance. The dashed line is for turbulent flow without the particles.  $z/a = 1$  is the rear stagnation point of the particle.

energy dissipation defined by

$$\tau_m = \frac{k}{\epsilon_u}, \quad \tau_T = \frac{\frac{1}{2}\overline{T'^2}}{D\overline{\nabla T' \cdot \nabla T'}}. \quad (5.29)$$

These two quantities, averaged over cross-stream planes, are shown as functions of the downstream distance in figure 5.18. The upper pair of lines shows  $\tau_m$  with (solid) and without particles. The particles increase the energy dissipation  $\epsilon_u$  and, therefore, somewhat decrease  $\tau_m$ . The lowest line is the thermal time scale, which is seen to be significantly shorter than the mechanical time scale. The reason is that temperature fluctuations are confined to the particle wakes, which occupy only a relatively small fraction of the cross-stream planes, as is graphically demonstrated by figure 5.4.

## 5.5 Summary

We have presented the results of the fully resolved simulations of turbulent flow and heat transfer past a regular array of 9 spheres arranged in a plane perpendicular to the mean flow. The simulations reveal a wealth of information about the character of the flow and the effectiveness of turbulence in disrupting the wakes of the spheres. This effect is graphically demonstrated in figure 5.5 which compares the thermal wakes of the spheres with and without turbulence. The mean and local particle Nusselt numbers are found to be only moderately increased with respect to the laminar case in spite of the very intense turbulence. The temperature fluctuations are strongest near the spheres downstream of the separation line.

We have found a striking difference between the behavior of the temperature and streamwise velocity in spite of the fact that the Prandtl number considered is unity. Most likely this behavior is caused by the blockage of the flow caused by the spheres which has a strong effect on the velocity field but does not have a counterpart for the temperature field. The fact that, in the simple analysis of section 5.3 in which the particles are treated as point in a uniform Oseen flow velocity and temperature are indeed similar lends some support to this conjecture. For this reason, many of the considerations developed for the behavior of passive scalars in turbulence may not applicable to flows of this type.

# Appendices

## 5.A Laminar flow and heat transfer past an infinite planar array of point particles<sup>2</sup>

The Oseen approximation to Navier-Stokes equations are written as:

$$\mathbf{U} \cdot \nabla \mathbf{u} = -\frac{1}{\rho} \nabla p + \nu \nabla^2 \mathbf{u}, \quad (5.30)$$

in which  $\mathbf{u}$  and  $p$  are the velocity and pressure disturbances due to the particle and  $\nu$  is the fluid kinematic viscosity. At upstream and downstream infinity the velocity is  $\mathbf{U}$ .

If interest lies in the energy exchange between the particle and the fluid, an approximation consistent with (5.30) would be

$$\mathbf{U} \cdot \nabla T = D \nabla^2 T, \quad (5.31)$$

in which  $D = k/\rho c_p$  is the thermal diffusivity.

In the following sections we give the mathematical model and solution to the velocity and temperature fields in the steady uniform flow past a regular planar array of point-like particles.

---

<sup>2</sup>This section is based on a paper by the same title authored by Y. Wang and A. Prosperetti, prepared to be submitted to *Int. J. Heat Mass Transfer*.



### 5.A.1 Mathematical model

We consider a regular planar array of point particles located at  $z = 0$ . The incident flow has temperature  $T_i$  and is steady and uniform with velocity  $\mathbf{U} = U\mathbf{k}$ , in which  $\mathbf{k}$  is a unit vector in the flow direction  $z$ . The particles are located at positions  $\mathbf{x}_{jk} = (x = jd_x, y = kd_y, z = 0)$ , with  $-\infty < j, k < \infty$ . The fluid is incompressible with constant properties. The mathematical model consists of the equation of continuity

$$\nabla \cdot \mathbf{u} = 0, \quad (5.32)$$

the momentum equation in the Oseen form (5.30) augmented by the force  $f$  exerted by the fluid on each particle,

$$U \frac{\partial \mathbf{u}}{\partial z} = -\frac{1}{\rho} \nabla p + \nu \nabla^2 \mathbf{u} - \mathbf{k} \sum_{j,k=-\infty}^{\infty} \frac{f}{\rho} \delta(\mathbf{x} - \mathbf{x}_{jk}), \quad (5.33)$$

and by the energy equation similarly augmented by the heat  $Q$  transferred by the fluid to each particle:

$$U \frac{\partial T}{\partial z} = D \nabla^2 T - \sum_{j,k=-\infty}^{\infty} \frac{Q}{\rho c_p} \delta(\mathbf{x} - \mathbf{x}_{jk}). \quad (5.34)$$

In these equations  $\mathbf{u}$  represents the velocity perturbation due to the particles and  $\rho$  and  $c_p$  are the fluid density and specific heat.

The flow is clearly periodic in the cross-stream planes with period  $d_x$  in the  $x$  direction and  $d_y$  in the  $z$  direction. Upon integration of the momentum equation over a volume of infinite length and cross section  $d_x \times d_y$ , with the

particle on its axis, we readily find

$$p_i - p_\infty = \frac{f}{A}, \quad (5.35)$$

with  $A = d_x d_y$  and  $p_\infty$  the limit value of the pressure far downstream of the particles. Since  $f$  is defined as the force exerted by the fluid on the particles, it is a positive number. This relation then quantifies the pressure drop across the particles plane. Proceeding similarly with the energy equation we find

$$T_i - T_\infty = \frac{Q}{U\rho c_p A}. \quad (5.36)$$

If the particles absorb heat from the fluid,  $Q > 0$  and the fluid is cooler downstream of the particles, and vice versa if the particles cede heat to the incoming fluid.

## 5.A.2 Decomposition of the flow field

Upon taking the divergence of the momentum equation we find, by (5.32),

$$\nabla^2 p = -\frac{\partial}{\partial z} \sum_{j,k=-\infty}^{\infty} f \delta(\mathbf{x} - \mathbf{x}_{jk}), \quad (5.37)$$

which can be satisfied by writing

$$p = p_i + \rho \partial \phi / \partial z, \quad (5.38)$$

with

$$\nabla^2 \phi = -\frac{f}{\rho} \sum_{j,k=-\infty}^{\infty} \delta(\mathbf{x} - \mathbf{x}_{jk}). \quad (5.39)$$

We define the longitudinal velocity component  $\mathbf{u}_L$  by

$$\mathbf{u}_L = -\frac{1}{U}\nabla\phi, \quad (5.40)$$

and note that its  $z$  component satisfies the linearized Bernoulli equation:

$$\frac{p}{\rho} + Uu_z = \frac{p_i}{\rho}. \quad (5.41)$$

We now introduce the transverse velocity  $\mathbf{u}_T = \mathbf{u} - \mathbf{u}_L$  and substitute into the momentum equation (5.33) to find, by (5.39),

$$U\frac{\partial\mathbf{u}_T}{\partial z} = \nu\nabla^2\mathbf{u}_T - \frac{f}{\rho}\left(\mathbf{k} - \frac{\nu}{U}\nabla\right)\sum_{j,k=-\infty}^{\infty}\delta(\mathbf{x} - \mathbf{x}_{jk}), \quad (5.42)$$

If we set  $\mathbf{u}_T = \mathbf{k}\chi - (\nu/U)\nabla\chi$  we find

$$\left(\mathbf{k} - \frac{\nu}{U}\nabla\right)\left(U\frac{\partial\chi}{\partial z} - \nu\nabla^2\chi + \frac{f}{\rho}\sum_{j,k=-\infty}^{\infty}\delta(\mathbf{x} - \mathbf{x}_{jk})\right) = 0, \quad (5.43)$$

which is satisfied by choosing the auxiliary function  $\chi$  so that

$$U\frac{\partial\chi}{\partial z} = \nu\nabla^2\chi - \frac{f}{\rho}\sum_{j,k=-\infty}^{\infty}\delta(\mathbf{x} - \mathbf{x}_{jk}). \quad (5.44)$$

It may be noted that, by (5.39) and (5.44),

$$\nabla \cdot (\mathbf{u}_L + \mathbf{u}_T) = \frac{1}{U}\left(-\nabla^2\phi + U\frac{\partial\chi}{\partial z} - \nu\nabla^2\chi\right) = 0, \quad (5.45)$$

so that the equation of continuity is satisfied by the sum  $\mathbf{u}_L + \mathbf{u}_T$  but not by each component individually.

### 5.A.3 Solution

Since the problem is periodic in the cross-stream directions, we focus our attention to the domain  $\left(-\frac{1}{2}d_x \leq x \leq \frac{1}{2}d_x, -\frac{1}{2}d_y \leq y \leq \frac{1}{2}d_y, -\infty < z < \infty\right)$ , with a single particle located at the origin. Thus we need to solve

$$\nabla^2 \phi = -\frac{f}{\rho} \delta(\mathbf{x}), \quad (5.46)$$

and

$$U \frac{\partial \chi}{\partial z} = \nu \nabla^2 \chi - \frac{f}{\rho} \delta(\mathbf{x}). \quad (5.47)$$

On the cross-stream boundaries periodicity requires that

$$\frac{\partial}{\partial(x, y)}(u_x, u_y, p) = 0, \quad u_z = 0. \quad (5.48)$$

In view of (5.38) we require that  $\phi$  tend to an arbitrary constant for  $z \rightarrow -\infty$ , which is conveniently chosen as 0 without loss of generality. This choice ensures that  $\mathbf{u}_L \rightarrow 0$  at  $-\infty$ . For  $\mathbf{u}_T$  to satisfy the same condition we impose that  $\chi \rightarrow 0$  at  $-\infty$ . At  $+\infty$ , by (5.35) and (5.38), we must have

$$\frac{\partial \phi}{\partial z} \rightarrow -\frac{f}{\rho A}. \quad (5.49)$$

For  $\mathbf{u}$  to vanish as  $z \rightarrow \infty$  it is therefore necessary that

$$\chi \rightarrow -\frac{f}{\rho AU}. \quad (5.50)$$

Equations (5.46) and (5.47) are readily solved by means of a double Fourier series in the cross-stream coordinates. We set

$$\phi = \frac{f}{\rho} \sum_{k=-\infty}^{\infty} \sum_{n=-\infty}^{\infty} \phi_{kn}(z) \exp 2\pi i(kx/d_x + ny/d_y), \quad (5.51)$$

substitute into (5.46) and take scalar products with the Fourier basis functions to find

$$\frac{d^2\phi_{kn}}{dz^2} - \lambda_{kn}^2\phi_{kn} = -\frac{\delta(z)}{A} \quad \text{with} \quad \lambda_{kn} = 2\pi\sqrt{\frac{k^2}{d_x^2} + \frac{n^2}{d_y^2}}. \quad (5.52)$$

Here, as before,  $A = d_x d_y$  is the area of the cross section of the fundamental period in the cross-stream planes. The relevant solutions of (5.52) for  $z < 0$  and  $z > 0$  and  $k, n$  not both 0 are

$$\phi_{kn}(z) = \frac{1}{2A\lambda_{kn}} \exp(\pm\lambda_{kn}z), \quad (5.53)$$

with the integration constant determined so as to satisfy the jump condition implicit in (5.52). For  $k = n = 0$  we need to impose the conditions at  $\pm\infty$  to find

$$\phi_{00} = -\frac{1}{A}H(z)z, \quad (5.54)$$

with  $H(z)$  the Heaviside step function.

For  $\chi$  we similarly start from

$$\chi = \frac{f}{\rho} \sum_{k=-\infty}^{\infty} \sum_{n=-\infty}^{\infty} \chi_{kn}(z) \exp 2\pi i(kx/d_k + ny/d_y), \quad (5.55)$$

and substitute into (5.47) to find

$$v \frac{d^2\chi_{kn}}{dz^2} - U \frac{d\chi_{kn}}{dz} - v\lambda_{kn}^2\chi_{kn} = \frac{\delta(z)}{A}. \quad (5.56)$$

The solutions valid for  $z < 0$  and  $z > 0$ , and  $k$  and  $n$  not both zero, are

$$\chi_{kn}(z) = -\frac{1}{AU\sqrt{1 + \frac{4v^2\lambda_{kn}^2}{U^2}}} \exp \left[ \frac{U}{2v} \left( 1 \pm \sqrt{1 + \frac{4v^2\lambda_{kn}^2}{U^2}} \right) z \right], \quad (5.57)$$

with the integration constant determined as before. When  $k = n = 0$  the solution is

$$\chi_{00} = -\frac{1}{AU} \left[ H(-z) \exp\left(\frac{Uz}{v}\right) + H(z) \right]. \quad (5.58)$$

In view of its similarity with (5.44), the solution for the energy equation may be written down directly by a simple adaptation of (5.55):

$$T = \frac{Q}{\rho c_p} \sum_{k=-\infty}^{\infty} \sum_{n=-\infty}^{\infty} T_{kn}(z) \exp 2\pi i(kx/d_x + ny/d_y), \quad (5.59)$$

with

$$T_{kn}(z) = -\frac{1}{AU\sqrt{1 + \frac{4D^2\lambda_{kn}^2}{U^2}}} \exp \left[ \frac{U}{2D} \left( 1 \pm \sqrt{1 + \frac{4D^2\lambda_{kn}^2}{U^2}} \right) z \right], \quad (5.60)$$

$$T_{00} = -\frac{1}{AU} \left[ H(-z) \exp\left(\frac{Uz}{D}\right) + H(z) \right]. \quad (5.61)$$

## References

- Arcen, B., A. Tanière, and M. Khalij (2012). "Heat transfer in a turbulent particle-laden channel flow". In: *Int. J. Heat mass Transfer* 55, pp. 6519–6529.
- Ardekani, M. N., O. Abouali, F. Picano, and L. Brandt (2018). "Heat transfer in laminar Couette flow laden with rigid spherical particles". In: *J. Fluid Mech.* 834, pp. 308–334.
- Bagchi, P. and K. Kottam (2008). "Effect of freestream isotropic turbulence on heat transfer from a sphere". In: *Phys. Fluids* 20, p. 073305.
- Balachandar, S. and J. K. Eaton (2010). "Turbulent Dispersed Multiphase Flow". In: *Annu. Rev. Fluid Mech.* 42, pp. 111–133.
- Botto, L. and A. Prosperetti (2012). "A fully resolved numerical simulation of turbulent flow past one or several spherical particles". In: *Phys. Fluids* 24, p. 013303.
- Breugem, W.-P. (2012). "A second-order accurate immersed boundary method for fully resolved simulations of particle-laden flows". In: *J. Comput. Phys.* 231, pp. 4469–4498.
- Carroll, P. L. and G. Blanquart (2013). "A proposed modification to Lundgren's physical space velocity forcing method for isotropic turbulence". In: *Phys. Fluids* 25, p. 105114.
- Dandy, D. S. and H. A. Dwyer (1990). "A sphere in shear flow at finite Reynolds number: effect of shear on particle lift, drag, and heat transfer". In: *J. Fluid Mech.* 216, pp. 381–410.
- Deen, N. G., S. H. L. Kriebitzsch, M. A. van der Hoef, and J. A. M. Kuipers (2012). "Direct numerical simulation of flow and heat transfer in dense fluid-particle systems". In: *Chem. Eng. Sci.* 81, pp. 329–344.
- Deen, N. G., E. A. J. F. Peters, J. T. Padding, and J. A. M. Kuipers (2014). "Review of direct numerical simulation of fluid-particle mass, momentum and heat transfer in dense gas-solid flows". In: *Chem. Eng. Sci.* 116, pp. 710–724.

- Dennis, S. C. R., J. D. A. Walker, and J. D. Hudson (1973). "Heat transfer from a sphere at low Reynolds numbers". In: *J. Fluid Mech.* 60, pp. 273–283.
- Dhole, S. D., R. P. Chhabra, and V. Eswaran (2006). "A numerical study on the forced convection heat transfer from an isothermal and isoflux sphere in the steady symmetric flow regime". In: *Int. J. Heat Mass Transfer* 49, pp. 984–994.
- Feng, Z. G. and E. E. Michaelides (2000). "A numerical study on the transient heat transfer from a sphere at high Reynolds at Péclet numbers". In: *Int. J. Heat Mass Transfer* 43, pp. 219–229.
- Feng, Z. G. and E. E. Michaelides (2008). "Inclusion of heat transfer computations for particle laden flows". In: *Phys. Fluids* 20, p. 040604.
- Feng, Z. G. and E. E. Michaelides (2009). "Heat transfer in particulate flows with Direct Numerical Simulation (DNS)". In: *Int. J. Heat Mass Transfer* 52, pp. 777–786.
- Feng, Z. G. and S. G. Musong (2014). "Direct numerical simulation of heat and mass transfer of spheres in a fluidized bed". In: *Powder Technol.* 262, pp. 62–70.
- Glowinski, R., T.-W. Pan, T. I. Hesla, D. D. Joseph, and J. Periaux (2001). "A fictitious domain approach to the direct numerical simulation of incompressible viscous flow past moving rigid bodies: Application to particulate flow." In: *J. Comput. Phys.* 169, pp. 363–426.
- Gudmundsson, K. and A. Prosperetti (2013). "Improved procedure for the computation of Lamb's coefficients in the Physalis method for particle simulation". In: *J. Comput. Phys.* 234, pp. 44–59.
- Gunn, D. J. (1978). "Transfer of heat or mass to particles in fixed and fluidised beds". In: *Int. J. Heat Mass Transf.* 21, pp. 467–476.
- Hoef, M. A. van der, M. V. Annaland, N. G. Deen, and J. A. M. Kuipers (2008). "Numerical simulation of dense gas-solid fluidized beds: A multiscale modeling strategy". In: *Annu. Rev. Fluid Mech.* 40, pp. 47–70.
- Kim, J. and H. Choi (2004). "An immersed-boundary finite-volume method for simulation of heat transfer in complex geometries". In: *KSME Int. J.* 18, pp. 1026–1035.
- Kurose, R., M. Anami, A. Fujita, and S. Komori (2012). "Numerical simulation of flow past a heated/cooled sphere". In: *J. Fluid Mech.* 692, pp. 332–346.
- Lagerstrom, P. A. (1964). "Laminar Flow Theory". In: *Theory of Laminar Flows*. Ed. by F. K. Moore. Princeton: Princeton University Press, pp. 88–102.
- Lundgren, S. (2003). "Linearly forced isotropic turbulence". In: *Annual Research Briefs*. Stanford University, pp. 461–473.



- Picano, F., W.-P. Breugem, and L. Brandt (2015). "Turbulent channel flow of dense suspensions of neutrally buoyant spheres". In: *J. Fluid Mech.* 764, pp. 463–487.
- Pope, S. B. (2000). *Turbulent Flows*. Cambridge: Cambridge U.P.
- Prosperetti, A. (1976). "Laminar Flow at Large Distances From an Infinite Two-Dimensional Grid". In: *J. Mécanique* 15, pp. 209–235.
- Ranz, W. E. and W. R. Marshall (1952). "Evaporation from drops, Part II". In: *Chem. Eng. Prog* 48, pp. 173–180.
- Rosales, C. and C. Meneveau (2005). "Linear forcing in numerical simulations of isotropic turbulence: Physical space implementations and convergence properties". In: *Phys. Fluids* 17, p. 095106.
- Sierakowski, A. J. and A. Prosperetti (2016). "Resolved-particle simulation by the Physalis method: Enhancements and new capabilities". In: *J. Comput. Phys.* 309, pp. 164–184.
- Stadler, M. B. de, N. R. Rapaka, and S. Sarkar (2014). "Large eddy simulation of the near to intermediate wake of a heated sphere at  $Re = 10,000$ ". In: *Int. J. Heat Fluid Flow* 49, pp. 2–10.
- Sun, B., S. Tenneti, S. Subramaniam, and D. L. Koch (2016). "Pseudo-turbulent heat flux and average gas-phase conduction during gas-solid heat transfer: flow past random fixed particle assemblies". In: *J. Fluid Mech.* 798, pp. 299–349.
- Tavassoli, H., S. H. L. Kriebitzsch, M. A. van der Hoef, E. A. J. F. Peters, and J. A. M. Kuipers (2013). "Direct numerical simulation of particulate flow with heat transfer". In: *Int. J. Multiphase Flow* 57, pp. 29–37.
- Tenneti, S. and S. Subramaniam (2014). "Particle-Resolved Direct Numerical Simulation for Gas-Solid Flow Model Development". In: *Annu. Rev. Fluid Mech.* 46, pp. 199–230.
- Tenneti, S., B. Sun, R. Garg, and S. Subramaniam (2013). "Role of fluid heating in dense gas-solid flow as revealed by particle-resolved direct numerical simulation". In: *Int. J. Heat Mass Transfer* 58, pp. 471–479.
- Uhlmann, M. (2005). "An immersed boundary method with direct forcing for the simulation of particulate flows". In: *J. Comput. Phys.* 209, pp. 448–476.
- Uhlmann, M. and A. Chouippe (2017). "Clustering and preferential concentration of finite-size particles in forced homogeneous-isotropic turbulence". In: *J. Fluid Mech.* 812, pp. 991–1023.
- Wang, Y., A. J. Sierakowski, and A. Prosperetti (2017). "Fully-resolved simulation of particulate flows with particles-fluid heat transfer". In: *J. Comput. Phys.* 350, pp. 638–656.

- Wang, Z., J. Fan, K. Luo, and K. Cen (2009). "Immersed boundary method for the simulation of flows with heat transfer". In: *Int. J. Heat Mass Transfer* 52.19, pp. 4510–4518.
- Whitaker, S. (1972). "Forced convection heat transfer correlations for flow in pipes, past flat plates, single cylinders, single spheres, and for flow in packed beds and tube bundles". In: *AIChE J.* 18, pp. 361–371.
- Yu, Z., X. Xiao, and A. Wachs (2006). "A fictitious domain method for particulate flows with heat transfer". In: *J. Comput. Phys.* 217, pp. 424–452.
- Zhu, H. P., Z. Y. Zhou, R. Y. Yang, and A. B. Yu (2008). "Discrete particle simulation of particulate systems: A review of major applications and findings". In: *Chem. Eng. Sci.* 63, pp. 5728–5778.
- Zonta, F., C. Marchioli, and A. Soldati (2011). "Time behavior of heat fluxes in thermally coupled turbulent dispersed particle flows". In: *Acta Mech.* 218, pp. 367–373.

# Chapter 6

## Conclusion

Disperse two-phase flows offer an extreme challenge to computational fluid mechanics. The particle-turbulence interaction, complex and time-dependent fluid boundary, simultaneous presence of many spatial and temporal scales, particle-particle interaction and others are major obstacles preventing extensive in-depth studies of these systems. This complexity has severely limited our ability to study important problems such as the formation of bubbles in fluidized beds, the detailed mechanism of sediment transport, the formation of rain and other important phenomena. Until relatively recently the only tool available to simulate these flows was the so-called point-particle model, in which the finite extent of the particles is neglected and the hydrodynamic forces are parameterized with a degree of accuracy that it is very difficult to assess.

It is only in the last few years that the situation has improved thanks to the advent of more powerful computational hardware and improved numerical methods able to take advantage of its features. One of these computational methods, which has been used and extended in the present work, is

PHYSALIS, which has been efficiently implemented on GPU-based computers. The method is accurate and efficient and, together with more established ones such as the immersed boundary method and the fictitious domain method, is a very promising tool for the investigation of these complex systems.

In the present work we have used the isothermal version of PHYSALIS to study the rotational dynamics of a particle in a turbulent flow. The current situation in which very limited results exist for non-isothermal particulate systems has motivated us to extend the method to deal with heat-transfer problems. By studying several examples of steady and unsteady heat transfer problems, with stationary or moving particles, we have demonstrated the effectiveness of our extension. In particular, we have presented detailed results for the turbulent flow past a planar array of particles colder than the incoming fluid.

In extending PHYSALIS to the energy equation we have adopted a lumped-capacitance model for the particle energy. The consequent uniformity of the particle temperature results in a boundary condition of the Dirichlet type for the fluid temperature. One can envisage a straightforward extension to Neumann or Robin conditions, provided the lumped capacitance model remains applicable. The more general case with a spatially, as well as temporally, variable particle temperature would be more difficult to include due to the dependence of diffusion problems on past history.

The possibility of direct simulations of disperse flows based on first principles opens the way to a better understanding of the physics of these systems. Once this physics has become clearer, it will be possible to incorporate it in

reduced-order models incorporating a coarse-grained description of large particulate systems. Several such models have been proposed, but they appear to be affected by several limitations. It is our hope that the work described in this thesis brings a modest contribution to progress in this direction.

# Curriculum Vitae

Yayun Wang was born in Hubei, China on August 1990. She graduated from Shanghai Jiao Tong University in 2011 with a Bachelor of Science degree in Mechanical Engineering. She obtained a Master's degree from the same department in 2013 advised by Professor Hua Liu. She started her Ph.D. program in Johns Hopkins University in September 2013 under the supervision of Professor Andrea Prosperetti. Her research focuses on the simulation of heat transfer in particulate flows. She defended her dissertation for the Doctor's degree of Philosophy in January 2018.